A Study on Plasma Process-Induced Damage during Fabrication of Si Devices and Methodology for Optical Measurement

---

Asahiko MATSUDA

2013

Preface

From 2008 to 2013, the author of this dissertation studied a problem in the field of plasma electronics / semiconductor process engineering, called plasma process-induced damage — in particular, "physical damage" in the silicon substrate caused by the bombardment of ions during fabrication of devices. With rapid miniaturization of semiconductor devices, formation of physical damage during the plasma etching process has become a problem with a negative impact on the performance and reliability of devices. To address this problem, methodology to characterize physical damage on silicon wafers was studied with a focus on two optical techniques: spectroscopic ellipsometry and photoreflectance spectroscopy. Optical techniques have an advantage of being contactless and nondestructive, which makes them suitable as a damage characterization technique to be used not only in laboratories but also in mass production lines.

In chapter 1, brief history and background behind microfabrication technology, plasma etching, and plasma process-induced damage are overviewed. Chapter 2 explains the techniques and apparatuses that were used in our experiments. In chapter 3, the structure of the damaged layer was examined, and an optical model to address the damaged structure using spectroscopic ellipsometry is proposed and evaluated. In chapter 4, the depth profiles of the defects in the damaged layer are analyzed; using the optical model established in the previous chapter, damage quantification by photoreflectance spectroscopy, and wet etching technique. In chapter 5, temperature-controlled photoreflectance spectroscopy is explored. An im-

provement in the signal intensity accomplished with this technique is shown, with theoretical explanations that brought the improvement. The conclusion is given in chapter 6, with a brief outline on the remaining problems and issues for the near future.

Table of Contents

Nomenclature

Symbols and units

International System of Units (SI) base/derived units are shown first. Other units used in this dissertation follow in parentheses.

A^*	modified Richardson constant		
a, b, c	(arbitrary) constants		
C	amplitude factor		
d	thickness / depth	m	
d	derivative		
E	energy	J	(eV)
e	elementary charge	C	
e	Napier's constant		
$\hat{\mathbf{e}}$	unit polarization vector		
$\boldsymbol{\mathcal{E}}$	electric field	V m^{-1}	
E_g	critical point energy	J	(eV)
E_i	incident ion energy	J	(eV)
f	frequency	Hz	
f	volume fraction	%	
h	Planck constant	J s	
$\hbar$	reduced Planck constant	J s	
$\mathcal{H}$	Hamiltonian		
I	current	A	
i	imaginary unit		
i, j, k, l	indices		
I_p	modulation beam intensity	W	
J	joint density of state		
k	extinction coefficient		
$\mathbf{k}$	wave vector		
k_B	Boltzmann constant	J K^{-1}	
M	number of measurement points		

m	mass of particle	kg	
N	complex refractive index		
n	refractive index		
n	dimensionality of interband critical point		
N_{dam}	areal defect density	m^{-2}	
n_{dam}	volume defect density	m^{-3}	
n_{e}	electron density	m^{-3}	
P	power	W	
P	number of unknown parameters		
p	pressure	Pa	(Torr)
$\mathbf{p}, p$	momentum		
P_1, P_2	parameters to express I_p dependence of C		
Q	flow rate	$\mathrm{m}^3\ \mathrm{s}^{-1}$	(sccm)
R	reflectivity / reflectance		
$\mathbf{r}$	coordinate vector		
r_p, r_s	amplitude reflection coefficients		
T	temperature (in kelvins)	K	
T	temperature (in joules)	J	(eV)
t	time	s	(min)
V	voltage	V	
V	potential energy	J	(eV)
v	interatomic potential		
V_{dc}	DC self-bias voltage	V	
V_{pp}	peak-to-peak voltage	V	
V_{s}	surface potential	J	(eV)
α	absorption coefficient	m^{-1}	
α, β	Seraphin coefficients		
α, β	(arbitrary) constants		
Γ	broadening parameter	J	(eV)
γ	quantum efficiency		
Δ	phase shift	rad	
Δ	change of the following quantity		
ε	(relative) dielectric function		

ε_0	vacuum permittivity	F m^{-1}	
η	ideality factor		
θ	phase factor	rad	
μ	effective mass		
ν	frequency of light	Hz	
ρ	complex refractive ratio		
σ	unbiased estimator		
Φ	total interatomic potential		
ϕ	angle of incidence	rad	(°)
Ψ	amplitude ratio		

∂	partial derivative
$\bar{a}$	mean
a'	perturbed

Abbreviations and sub-/superscripts

Title words are abbreviated in accordance with the ISO 4 standard. Other abbreviations, acronyms, or symbols are listed below. These may be used in combination with the symbols listed in the preceding table as subscripts or superscripts.

0	before etching / reference
0	unperturbed
1	real
2	imaginary
2	two-body
3	three-body
arb	arbitrary
at	atomic
AUX	auxiliary
B / BE	Bose–Einstein
BV	backvalve
c	centroid

c	chopper
CCP	capacitively coupled plasma
coeff	coefficient
ctrl	control
C-V	capacitance-voltage
D / d	drain
dam	damaged
DC / dc	direct current
DHF	diluted hydrofluoric acid
DP	dry pump
e	electron
EMA	effective medium approximation
exp	experiment
ext	extension
f	floating
FET	field-effect transistor
FV	forevalve
G / g	gate
g	band gap
gi	indirect band gap
GV	gate valve
HRTEM	high-resolution transmission electron microscopy/micrograph
i	ion
IC	integrated circuit
ICP	inductively coupled plasma
IL	interface layer
int	integration
ITRS	International Technology Roadmap of Semiconductors
LN_2	liquid nitrogen
MD	molecular dynamics
MFC	mass flow controller
mod	model
MOSFET	metal–oxide–semiconductor field-effect transistor
p	plasma

p	parallel compoment
PECVD	plasma-enhanced chemical vapor deposition
PID	plasma-induced damage
PMT	photomultiplier tube
PPID	plasma process-induced damage
PR	photoreflectance
PRS	photoreflectance spectroscopy
R	recess
RBS	Rutherford backscattering spectrometry
REF / ref	reference
RF / rf	radio frequency
RP	rotary pump
S	source
S / s	semiconductor
s	Senkrecht (perpendicular) component
SE	spectroscopic ellipsometry
SL	surface layer
SMA	Sub Miniature A (optical fiber connector type)
S/N	signal-to-noise
sub	substrate
TDFF	third-derivative functional form
TEM	transmission electron microscopy/micrograph
th	threshold
TMP	turbomolecular pump
w	wet etching
wt	weight
XTEM	cross-sectional transmission electron microscopy/micrograph

1. Introduction

1.1. Brief history

The latter half of the 20th century saw the invention of integrated circuits (ICs) by Kilby [1] and Noyce [2], and their subsequent development into large-scale integration (LSI) and very-large-scale integration (VLSI). ICs/LSIs are the core elements in today's information technology and telecommunications. The electronics industry has become one of the world's largest industries, accounting for about 10% of the gross world product [3]. The exponential growth of semiconductor devices, commonly known as Moore's law [4], [5], has been realized by fabricating the devices continuously smaller than the preceding generation (Fig. 1.1), thereby cramming more components into a single chip.

One of the driving forces for such a rapid growth was the scaling law, formulated in 1974 by Dennard and colleagues [6]. Scaling law states that when the dimension of a metal–oxide–semiconductor field effect transistor (MOSFET) is decreased by a factor of $1/\kappa$ while preserving its electric field pattern, the propagation delay* decreases by $1/\kappa$ and the power dissipation by $1/\kappa^2$. This characteristic motivated the industry to continuously improve the necessary set of technologies to allow for further miniaturization [7]. This set of technologies

* The length of time required for the output of a logic gate to be stable and valid. Reduction of delay results in devices of higher performance.

is called microfabrication, microtechnology, or miniaturization engineering,[†] and includes photolithography, ion implantation, thin film deposition, polishing, and plasma etching.

In the size domain required for semiconductor device fabrication, the "tools" that we must use to are the atoms, molecules, ions, electrons, and photons from chemically reactive plasma discharges.

> Materials and surface structures can be fabricated that are not attainable by any other commercial method ... [Plasma processes] are the equivalent, on a micrometer-size scale, of centimeter-size manufacture using metal and components, bolts and solder, and drill press and lathe.
>
> — *Lieberman and Lichtenberg* [10]

The unique characteristics of plasma etching includes sub-micrometer to nanometer precision, anisotropy, and uniformity. However, as is the case with any "tools" or manufacturing processes, plasma etching is not free from imperfections or problems. The problems include profile anomalies, insufficient selectivity, loss of microscopic uniformity, and aspect-ratio dependence [11].

This paper covers one of such problems — *plasma process-induced damage* (PPID). As the scale of device components have reached 20–30 nm[‡] (as of 2012 [7], [12]), the effects of *physical damage* (one of the PPID mechanisms) on device performance has become increasingly significant. It could be considered as one of the effects that make further miniaturization (a strategy known as "More Moore") difficult. Detailed understanding of PPID and methodology to

---

[†] Terminology varies among authors [8], [9]. This paper adopts "microfabrication" as the blanket term.

[‡] Scaling is product-specific. According to the 2012 Update of the ITRS Overall Roadmap Technology Characteristics, the half pitches for different products in 2012 are as follows [12].

Flash: 20 nm, DRAM: 32 nm, MPU/ASIC Metal 1: 32 nm.

In this context, "half pitch" refers to half of the expected average distance between identical features in an array of components fabricated with this process. DRAM: dynamic random access memory, MPU: microprocessor unit, ASIC: application-specific integrated circuit.

characterize them is extremely important, which is the topic of this work. Further details will be explained in the following sections.

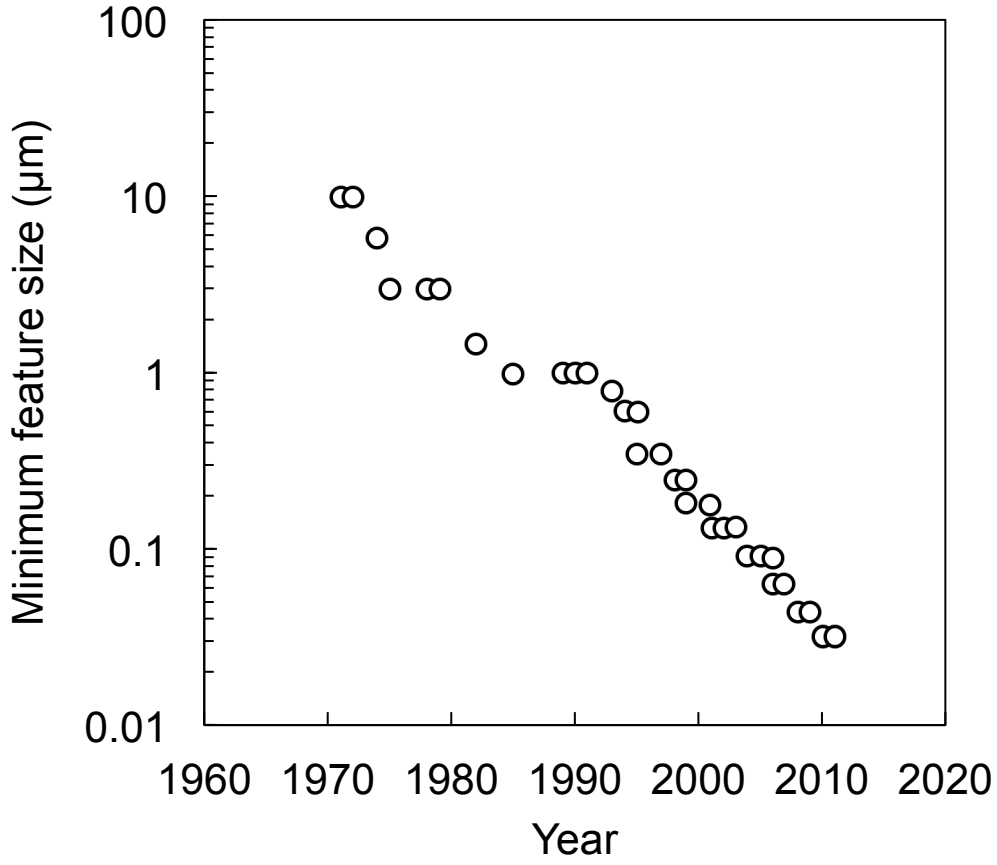

Fig. 1.1 The evolution of transistor gate length (minimum feature size) over the past 4 decades, after Ref. [7].

1.2. MOSFETs

A transistor is a semiconductor device used to amplify and switch electronic signals. It is the fundamental component of modern semiconductor devices, fabricated on a semiconductor substrate along with other components (resistors, capacitors, etc.) and wired together to process various signals [13]. The field-effect transistor (FET) is the most common type of transistors today, which uses electric field to control the device.

Typical structure of a FET is illustrated in Fig. 1.2. A FET has three electrodes: the gate (G), the source (S), and the drain (D). The electrodes are wired by metal (typically Cu) interconnects. Various dielectrics (ILD, PMD, and STI) provide insulation between the components. For the gate, its electrode was historically metal, its insulator (the black layer beneath the gate electrode) was SiO_2, and the substrate was Si; hence, this structure was named "MOS" (metal–oxide–semiconductor). Today's MOS structures instead use poly-Si for the gate. High-κ dielectric materials[§] may be used as the insulator to reduce leakage currents and improve device reliability [14]. These transistors may still be called MOSFETs, while some consider it to be a misnomer and use the term MISFET (metal–insulator–semiconductor FET) or IGFET (insulated-gate FET) [15].

There are two types of MOSFETs depending on the type of the carrier: n-MOSFET and p-MOSFET, which have corresponding characteristics but uses carriers of opposite charge. In an n-MOSFET (p-MOSFET), the transistor is fabricated on p-type (n-type) Si. When gate voltage (V_g) is applied to the gate electrode (G), the electric field penetrates through the thin insulating dielectric, repelling the holes (electrons) and creating a depletion region. Further increase

[§] Materials with dielectric constants higher than SiO_2.

in the gate voltage causes electrons (holes) to appear at the interface, creating inversion layer between the source (S) and the drain (D) (a "channel"), allowing the drain current (I_d) to flow through the channel and thereby turning the transistor on. Threshold voltage (V_{th}) is defined as the voltage at which there are sufficient carriers in the channel to make a low-resistance conductive path between the source and the drain.

In sub-micrometer MOSFETs, it becomes necessary to prevent *hot electron* problems: the high electric fields accelerating the carriers to an extent that can break Si–Si bonds or be injected into gate dielectrics and cause device reliability problems [13]. Also, *short channel effects*, caused by the drain electric field penetrating through the channel region, affect the potential barrier between the source and channel regions [13]. These problems are solved by creating shallow *extension regions* at the tip of the source and drain junctions. To construct this, structures known as *sidewall spacers* are prepared through clever use of isotropic deposition process and anisotropic etching process. Modern MOSFETs may also have *offset spacers* to guide the dopant distribution, in order to optimize the source–drain separation.

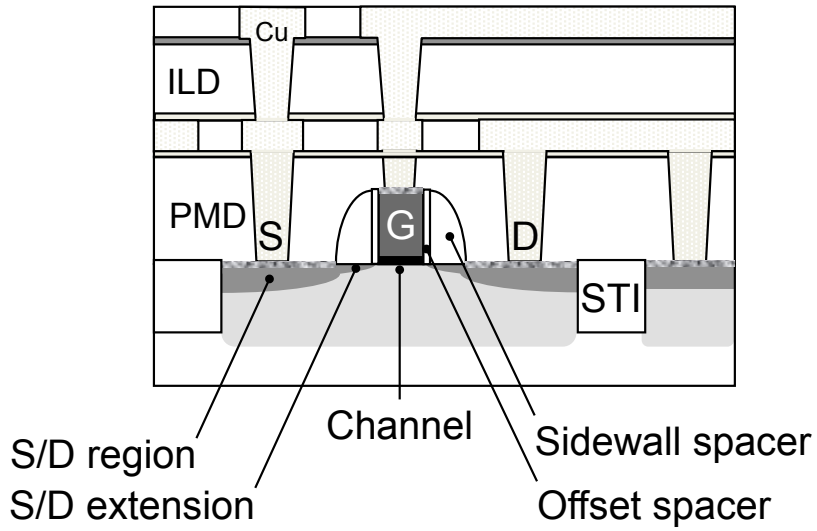

Fig. 1.2 A schematic diagram of a MOSFET cross section. G: gate, S: source, D: drain, ILD: inter-layer dielectric, PMD: pre-metal dielectric, STI: shallow trench isolation.

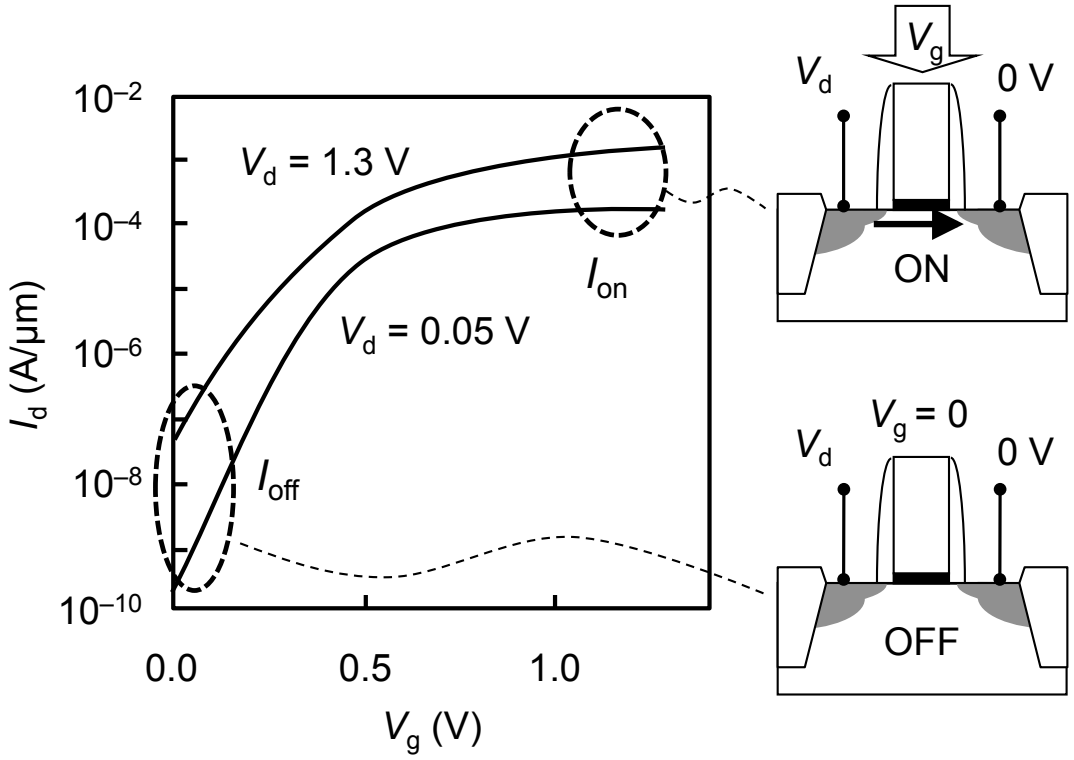

Fig. 1.3 Operation of a MOSFET and its I_d-V_g characteristics.

1.3. Plasma etching and damage

Plasma etching is one of the core elements in microfabrication, used in tandem with photolithography. The names of the processes come from etching and lithography in the field of fine arts and printing, dating back to the 16th century and the 19th century, respectively [16]. Traditional etching, such as copper etching, employed wet chemical etchants such as HNO_3 or $FeCl_3$. On the other hand, nanoscale etching uses gases, plasmas, or beams of reactive elements (*e.g.* halogen) as the etchant. For this reason, this method is called *dry etching*. Dry etching is also called *plasma etching* when the etchant takes the state of plasma.

Fig. 1.4 shows the schematics of one set of processes. This set of processes leaves a thin film of the desired material (shown in black) in a certain pattern on the surface of the starting material. The set is to be repeated for the number of materials and layers required to create intricate multi-layered structures. The mask is transparent, but is partly opaque in the form of the pattern to be fabricated.** The photoresist in the unmasked areas are chemically altered by UV incidence to be soluble in the developer liquid (in the case of positive photoresist). After exposure, the film material is removed from the surface by chemically reactive plasma discharges [10].

A typical discharge can contain many species that interact with solid surfaces to etch or deposit material. The species can be grouped into ions and electrons of various kinetic energies, neutral particles (including gas molecules,

** For sake of simplicity, the figure illustrates the size of the mask as the same size with the features developed on the photoresist. This is sometimes called 1:1 lithography or 1× lithography [9]. Alternatively, optical apertures may be inserted between the mask and the photoresist surface. This method is called projection lithography. The chief advantage of this method is that the beam that goes through the mask may be arbitrarily reduced in scale by lenses. The masks can be much larger than the final patterns, typically by scale of around five [9].

radicals, and atoms in their ground states or in various excited states), and photons [10], [17]. Etching processes are driven by a combination of reactions by these species, wherein the reactive species adhere to the material surface, reacts with atoms of the material to form products, and desorbs as molecules to be ultimately pumped away from the chamber. This sequence of events is assisted by the energy supplied as kinetic energies of impinging energetic ions [18], accelerated in the direction normal to the surface by the electric field in the plasma sheath [10]. The process is schematically illustrated in Fig. 1.5. The advantage of this ion-assisted reaction was clearly illustrated by a key study by Coburn and Winters [18], who showed that the etch rate attained by this ion-assisted chemical reaction is much faster than the sum of chemical etching alone and physical sputtering alone. Not only that, it also makes etching *anisotropic*, as required to transfer the pattern of the photoresist onto the underlying film as faithfully as possible with minimum lateral etching.

However, it has been pointed out that there are several undesirable phenomena that arise as a side effect of this process, collectively known as plasma-induced damage (PID) or plasma process-induced damage (PPID). As illustrated in Fig. 1.6, PPID can be classified into charging damage, radiation damage, and physical damage [19], [20].

Charging damage refers to defects (typically Si–O bond breakage) in the gate oxide and the SiO_2/Si interface, caused by an electrical stress that originates from the imbalance between electron current and ion current from the plasma and the potential difference between the gate electrode and the Si substrate [21]. Charging damage results in breakdown of the gate oxide [22] and enhancement of negative bias temperature instability (NBTI)[††] [23]. To prevent

[††] Degradation of MOSFET performance (drain current / threshold voltage) under negative bias stress and high temperature.

the effect of charging damage, design rules such as limitations on maximum antenna ratio have been proposed and used by circuit designers [24].

Radiation damage (UV radiation damage) is caused by ultraviolet radiation from the plasma, which may result in charging and/or electron–hole pair generation [25]. High-energy photons from the plasma are responsible for this type of damage. Note that the term "radiation damage" is sometimes used as a shorthand for "ion-radiation damage" to refer to the damage caused by ion bombardment [26], but this dissertation will not adopt this terminology.

This dissertation focuses on physical damage, also known as ion-bombardment damage. Collisions of ions with atoms in the substrate generate defect sites (*e.g.*, Si vacancies, displaced Si, interstitials, and dangling bonds [13]) near the surface (Fig. 1.7). An ion entering the substrate travels through the substrate in a random path, colliding with Si atoms and generating defects along the way, until it loses all its kinetic energy at a certain point [27]. (This point as measured along the axis of incidence is called the projected range of the ion.) In this dissertation, let us call the layer of Si with these defects the "damaged layer." Within the damaged layer, the density of the defects is therefore typically high near the surface and decreases with depth [Fig. 1.8(a)].

During the etching of gate electrodes and offset spacers, the damage induces oxidation of the underlying silicon substrate, which maybe removed during wet-etch treatment using hydrofluoric acid following plasma etching, resulting in a structure called the Si recess or the Si loss [28]–[30]. This mechanism is schematically illustrated in Fig. 1.8(b). The thickness of the recess is closely related to the thickness of the damaged layer. It has been found recently that Si recess causes a degradation in MOSFET performance by invoking a shift in its threshold voltage V_{th} [31]. On the other hand, defect distributed deeper into the substrate may remain as residual defects. Electrical capacitance-voltage

measurements have revealed that these defect sites act as negative-charge-trapping sites, which may cause drain current (I_d) degradation [32], [33].

The physics involved in the formation mechanism of physical damage was well studied around 1980s by authors including Yabumoto *et al.* [34] and Oehrlein *et al.* [35]–[37]. Studies focused on ion implantation processes (which typically employ ions at 10–500 keV) also contributed to understanding of this mechanism [38]–[41]. Device scales were larger than a micrometer at that time, and physical damage, which forms in the region 5–15 nm from the surface, did not have significant impact on device characteristics.

However, with rapid miniaturization of the devices, the effects of physical damage recently surfaced and could no longer be ignored. The depth of the damaged layer is determined by the energy distribution and projected range of incident ions, and thus is determined by plasma parameters, which is independent of device scale. Therefore, the thickness of the damaged layer has become significant in recent years [31]. The effect of residual charge-trapping sites is also more significant in scaled MOSFETs [33]. Therefore, it has become extremely important to accurately understand, characterize, and measure physical damage.

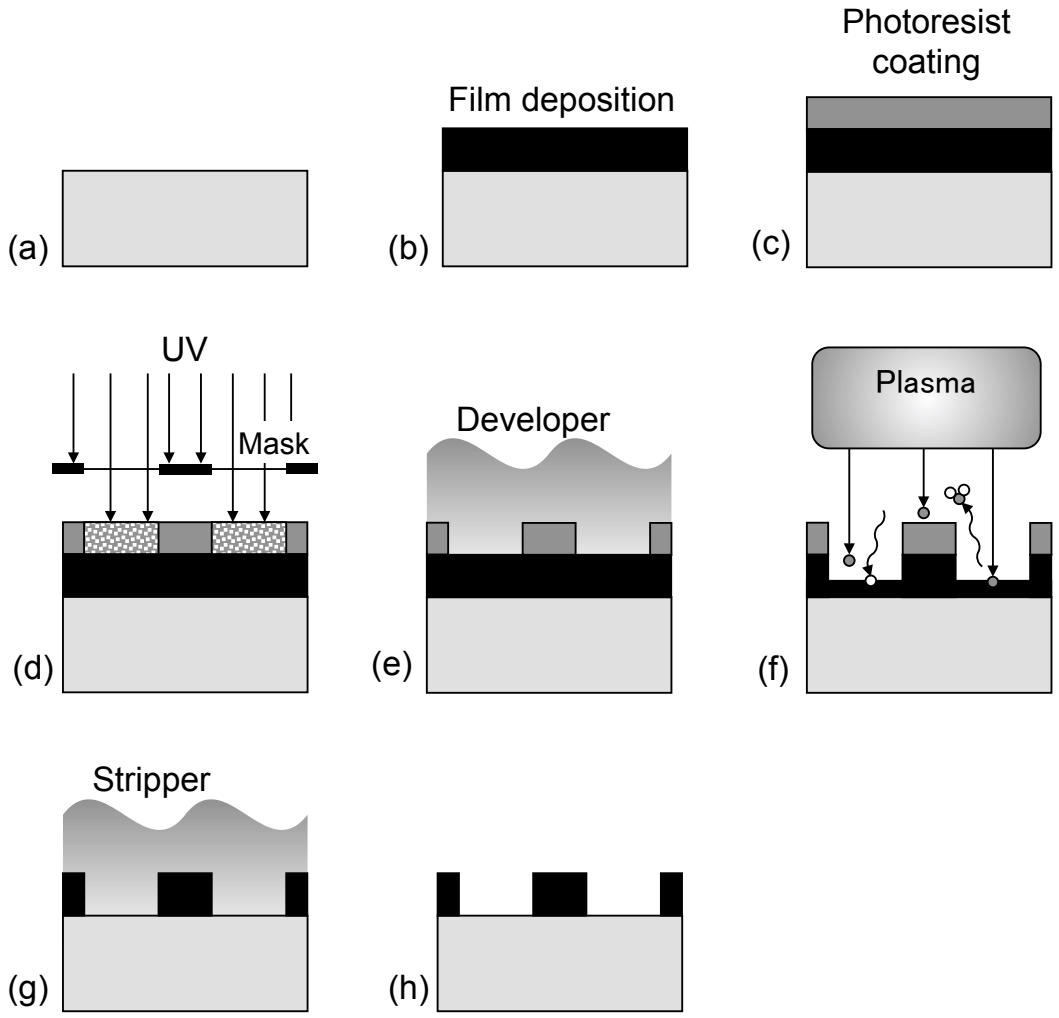

Fig. 1.4 Basic set of photolithography and etching processes.
(a) Starting material. (b) Film deposition. (c) Photoresist coating. (d) Exposure.
(e) Development. (f) Etching.
(g) Stripping (photoresist removal). (h) Resulting structure.

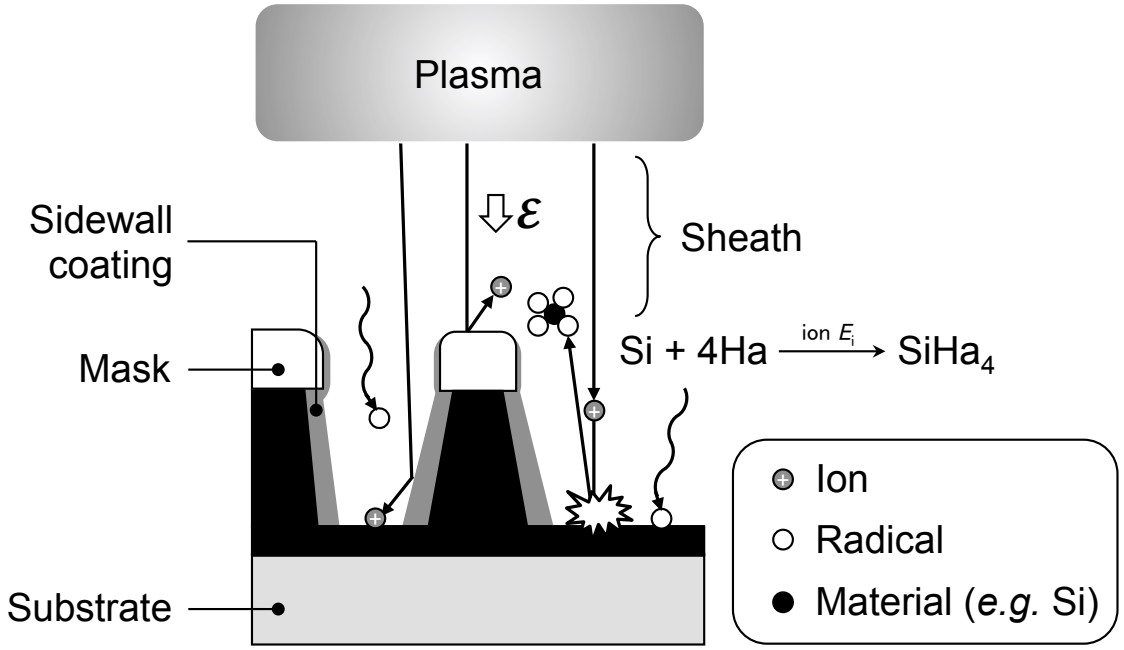

Fig. 1.5 An example of ion-enhanced etching; in this case, etching of Si by halogen (Ha = F, Cl, or Br). The reactive neutrals (Ha, Ha_2, $SiHa_2$, etc.) and the energetic ions accelerated by the electric field $\mathcal{E}$ in the sheath (Ha^+, Ha_2^+) are the major species in this reaction. Ion bombardment often increases the etching rate by directly enhancing the kinetics of the reaction and by removing surface contaminants that may block the process [10].

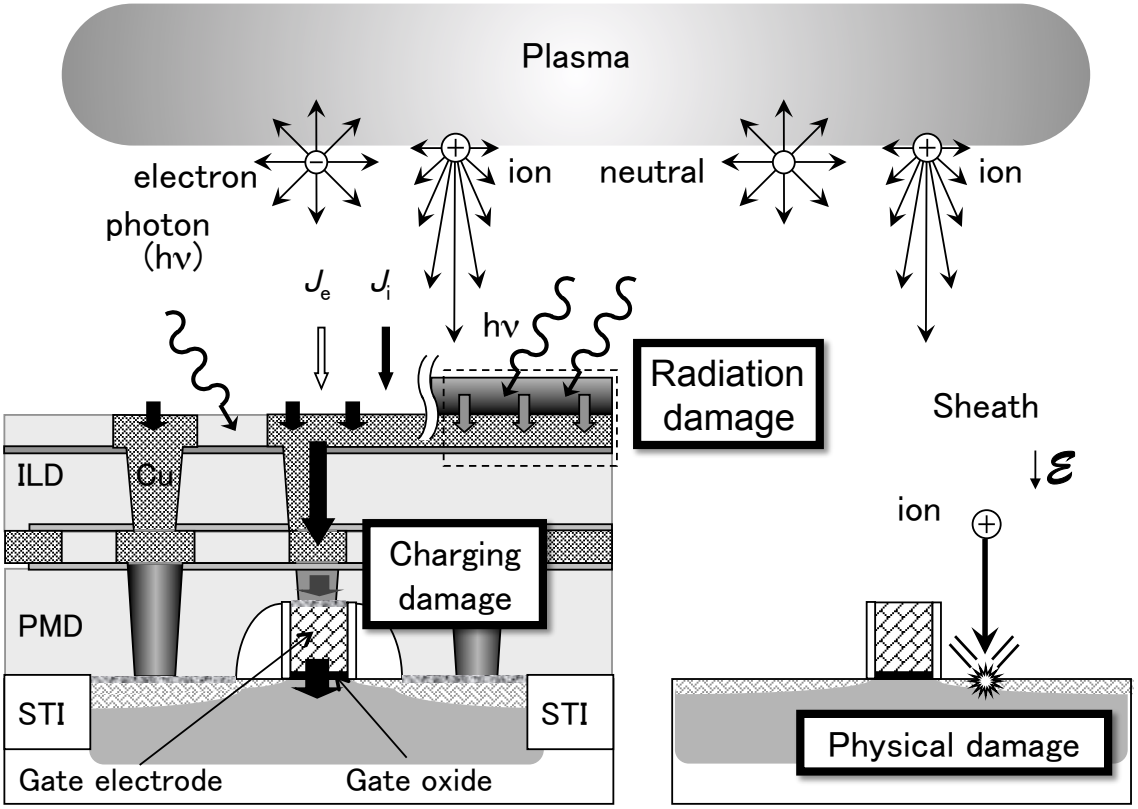

Fig. 1.6 Mechanisms of plasma process-induced damage.

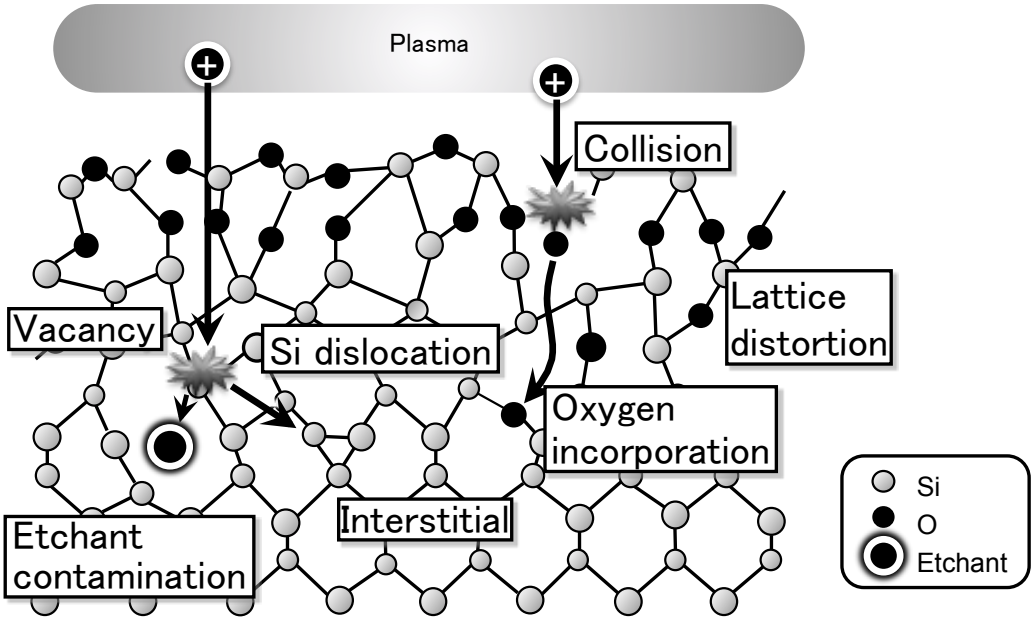

Fig. 1.7 Physical damage (ion-bombardment damage).

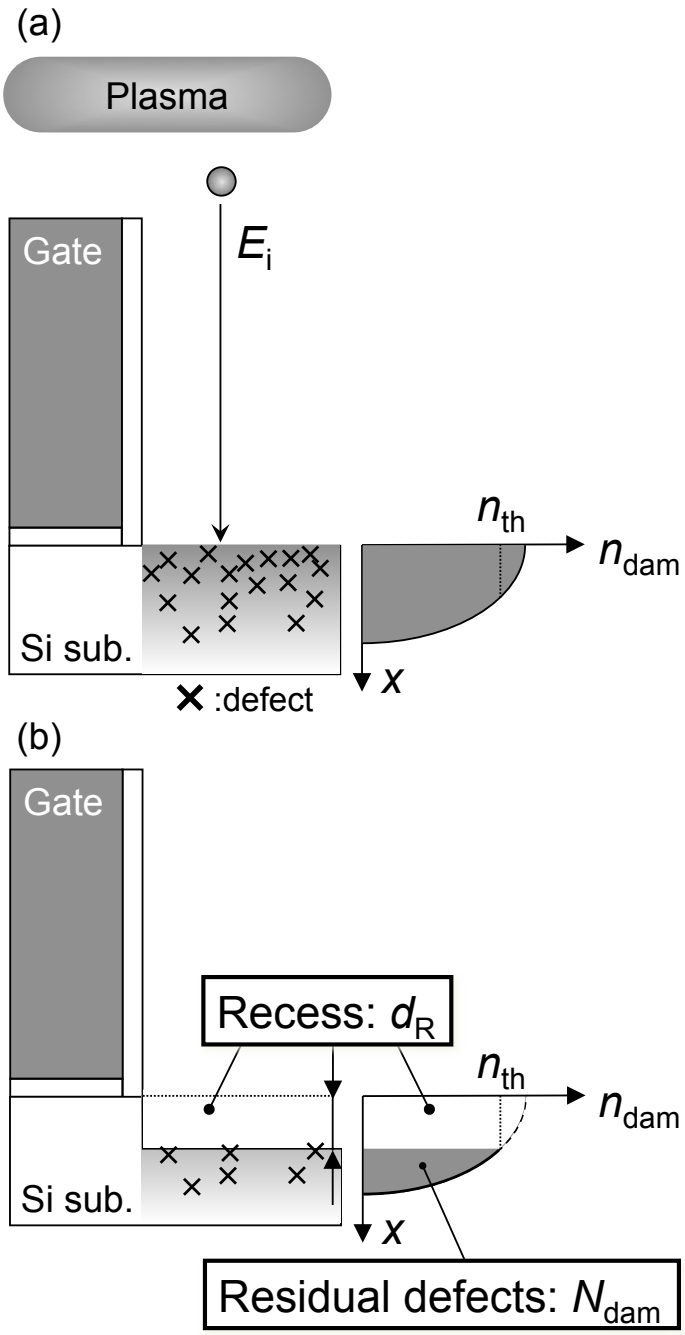

Fig. 1.8 Effects of physical damage on a MOSFET [42].
(a) Formation of the damaged layer and the defect density profile.
(b) Si recess and residual defects after post-etch wet treatment.

1.4. Characterization of physical damage

Due to the importance of characterizing and identifying defects in semiconductors, a wide variety of techniques have evolved through the latter half of the 20th century [43]. In order to study the damage, one must consider the causal relationship between:

i. the real-space structure of the defects (dislocations, interstitials, vacancies, etc.),
ii. the characteristics of the defects (such as its electrical/magnetic properties, trapping of carriers, absorption of photons, photoconductivity, luminescence, etc. [43]), and
iii. the effect on the device characteristics.

Perhaps the most straightforward technique is to observe the real-space crystallographic structure by taking a cross-sectional transmission electron micrograph (XTEM) using high-resolution transmission electron microscopy (HRTEM). This technique is capable of obtaining images that correspond to the crystalline structure of atoms, and therefore is able to determine the crystallinity of the specimen or lack thereof [44]. Under careful inspection, HRTEM can identify the structures of stacking faults, dislocation loops, and defect clusters [45], [46]. However, since the technique observes electrons transmitted through the specimen structure, the specimen must be sliced into a thin foil, making the technique tedious and inherently destructive. For a characterization technique to be widely used, it is desirable that it be a contactless and nondestructive method.

One of the strategies one could use to achieve contactless measurement is to use an optical characterization technique [47]. Common optical

techniques include ellipsometry, transmission/reflection spectroscopy, modulation spectroscopy, photoluminescence, and Raman spectroscopy [48]. This work focuses on two reflective optical techniques: spectroscopic ellipsometry (SE) and photoreflectance spectroscopy (PRS).

SE measures the change in amplitude (Ψ) and phase (Δ) between the p and s components of polarized light reflected from the sample [49], [50]. The optical properties of films on the sample surface can be obtained, such as refractive indices and dielectric functions of materials (n, k, ϵ). Also, the thickness of films (d) can be measured in high precision (≤ 1 nm scale [48]). It is frequently employed to monitor the material surface in mass production lines [48].

PRS, a form of modulation spectroscopy [48], [51], [52], monitors the reflectivity (R) of the specimen and its change (ΔR) induced by irradiation of a modulation beam (I_p). Energies and broadening parameters of interband transitions can be obtained with high precision (a few meV at room temperature [51]). Close examination of the lineshapes can also reveal the effects of electric/magnetic fields, temperature, hydrostatic pressure, and uniaxial stress [51]. Recent studies have applied PRS as a damage characterization technique [19], [53]–[56].

As mentioned, SE measures the ratio of amplitudes and shift in phase between the p and s components of light, and PRS measures a normalized quantity: $\Delta R/R$. Therefore, the methods do not require that every photon be collected, making them relatively robust in the sense that obstructions in the viewport, uneven surface morphology, or any other faults that result in partial loss of light do not affect the spectrum [51]. This is an advantage over other methods such as transmission/reflection spectroscopy.

In light of these characteristics, it is anticipated that a damage characterization based on SE and PRS would be useful, which brings us to the objectives of this study:

1. To understand how we could observe plasma-damaged samples using spectroscopic ellipsometry (a commonly used technique) and propose possible improvement on its usage for damage characterization methodology.
2. To gain detailed understanding of the structure of the damaged layer and characteristics of the defects.
3. To establish an advanced optical damage characterization methodology based on SE and PRS.

These should greatly contribute to minimizing the effects of PPID, in order to realize devices with even higher performance, higher reliability, and lower variability.

In chapter 2, the techniques and instrumentation used in this study are briefly explained. In chapter 3, an optimal optical model for damage characterization is comparatively studied, using simulations and composition analysis along with SE. In chapter 4, the distribution profiles of defects are analyzed using the methodology established in chapter 3, with a focus on ion mass/radius difference and their effect on damage depth. In chapter 5, an advanced PRS method is explored, where the wafer temperature was varied. The temperature dependence of the photoreflectance spectrum is discussed, which gives us insight into the optical transition involved and improvement in the signal intensity. The structure of the dissertation is roughly outlined in Fig. 1.9.

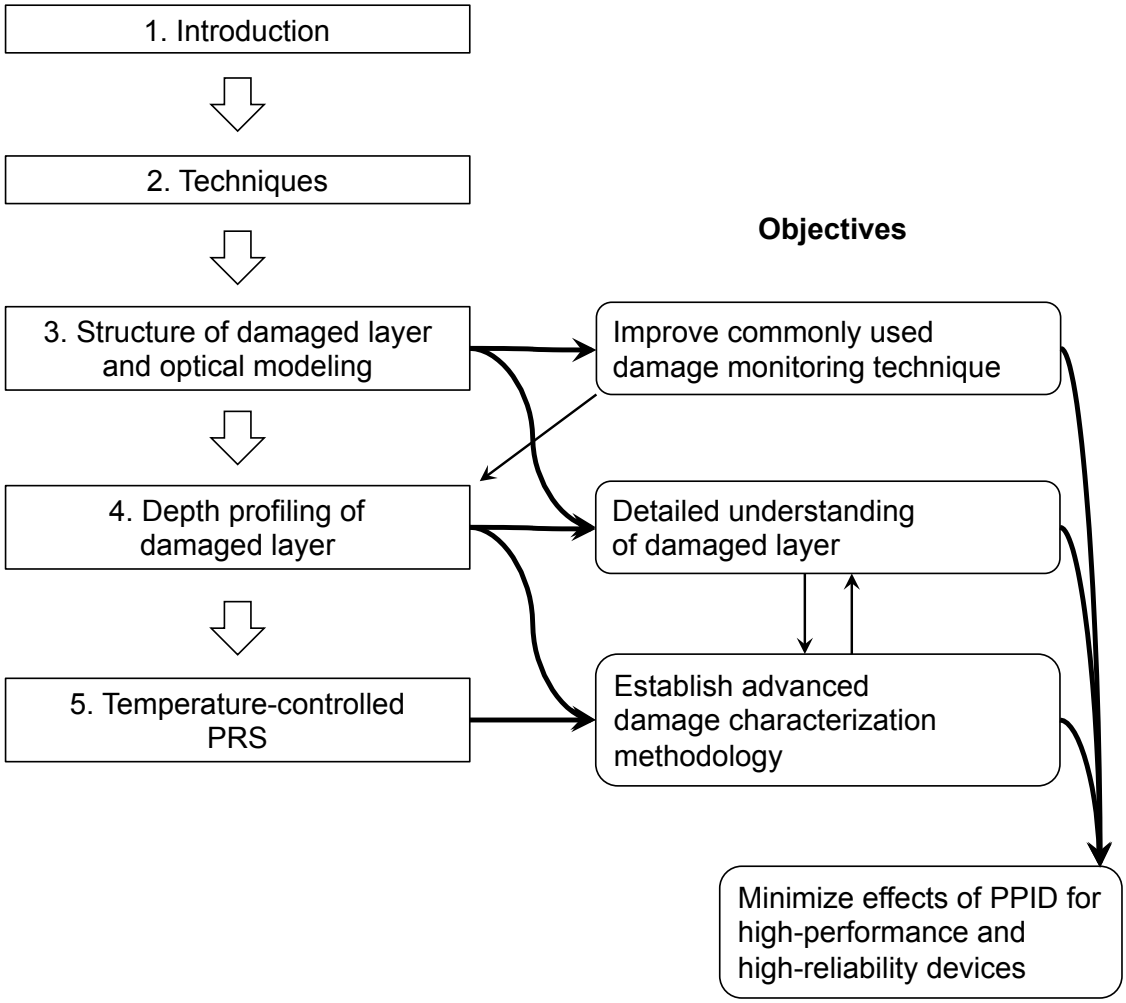

Fig. 1.9 Structure and objectives of the dissertation.

1.5. References

[1] J. S. Kilby, "Miniaturized electronic circuits," U.S. Patent 3138743, Jun. 23, 1964.

[2] R. N. Noyce, "Semiconductor device-and-lead structure," U.S. Patent 2981877, Apr. 25, 1961.

[3] S. M. Sze, *Semiconductor Devices: Physics and Technology*, 2nd ed. John Wiley & Sons, 2002.

[4] G. E. Moore, "Cramming more components onto integrated circuits," *Electronics*, vol. 38, no. 8, pp. 114–117, Apr. 1965.

[5] G. E. Moore, "Progress in digital integrated electronics," *IEDM Tech. Dig.*, vol. 21, pp. 11–13, 1975.

[6] R. H. Dennard, F. H. Gaensslen, V. L. Rideout, E. Bassous, and A. R. LeBlanc, "Design of ion-implanted MOSFET's with very small physical dimensions," *IEEE J. Solid-State Circuits*, vol. SC-9, no. 5, pp. 256–268, Oct. 1974.

[7] I. Ferain, C. A. Colinge, and J.-P. Colinge, "Multigate transistors as the future of classical metal–oxide–semiconductor field-effect transistors," *Nature*, vol. 479, pp. 310–316, Nov. 2011.

[8] M. J. Madou, *Fundamentals of Microfabrication: the Science of Miniaturization*, 2nd ed. Boca Raton: CRC Press, 2002.

[9] S. Franssila, *Introduction to Microfabrication*. West Sussex: John Wiley & Sons, 2004.

[10] M. A. Lieberman and A. J. Lichtenberg, *Principles of Plasma Discharges and Materials Processing*, 2nd ed. Hoboken, NJ: Wiley, 2005.

[11] C. Y. Chang and S. M. Sze, *ULSI Technology*. New York: McGraw-Hill, 1996.

[12] "International Technology Roadmap for Semiconductors: 2012 Update," 2012. [Online]. Available: http://www.itrs.net/.

[13] J. D. Plummer, M. Deal, and P. B. Griffin, *Silicon VLSI Technology*. Upper Saddle River, NJ: Prentice Hall, 2000.

[14] G. D. Wilk, R. M. Wallace, and J. M. Anthony, "High-κ gate dielectrics: Current status and materials properties considerations," *J. Appl. Phys.*, vol. 89, no. 10, pp. 5243–5275, May 2001.

[15] S. M. Sze, *Physics of Semiconductor Devices*, 2nd ed. New York: Wiley-Interscience, 1981.

[16] M. W. Marien, *Photography: a cultural history*, 2nd ed. Upper Saddle River, NJ: Pearson, 2006.

[17] T. P. Ma, "Plasma Process Induced Radiation Effects in CMOS Technology," presented at the 2002 7th International Symposium on Plasma-Process Induced Damage, Maui, HI, 2002, pp. 18–22.

[18] J. W. Coburn and H. F. Winters, "Ion- and electron-assisted gas-surface chemistry—An important effect in plasma etching," *J. Appl. Phys.*, vol. 50, no. 5, pp. 3189–3196, May 1979.

[19] K. Eriguchi and K. Ono, "Quantitative and comparative characterizations of plasma process-induced damage in advanced metal-oxide-semiconductor devices," *J. Phys. D*, vol. 41, no. 2, 024002, Jan. 2008.

[20] K. Eriguchi, K. Takahashi, and K. Ono, "Plasma-induced damage and its impacts on the reliability of advanced semiconductor devices," in *Proc. 6th Int. Conf. Reactive Plasmas & 23rd Symp. Plasma Processing*, Matsushima/Sendai, 2006, pp. 5–6.

[21] K. P. Cheung, *Plasma Charging Damage*. London: Springer, 2001.

[22] K. Eriguchi and Y. Kosaka, "Correlation between two time-dependent dielectric breakdown measurements for the gate oxides damaged by plasma processing," *IEEE Trans. Electron Devices*, vol. 45, no. 1, pp. 160–164, Jan. 1998.

[23] A. T. Krishnan, V. Reddy, and S. Krishnan, "Impact of charging damage on negative bias temperature instability," in *IEDM Tech. Dig.*, 2001, pp. 865–868.

[24] V. Shukla, V. Gupta, C. Guruprasad, and G. Kadamati, "Automated antenna detection and correction methodology in VLSI designs," in *Proc. Int. Symp. Plasma Process-Induced Damage*, 2003, pp. 158–161.

[25] T. Yunogami, T. Mizutani, K. Suzuki, and S. Nishimatsu, "Radiation Damage in SiO_2/Si Induced by VUV Photons," *Jpn. J. Appl. Phys.*, vol. 28, no. Part 1, No. 10, pp. 2172–2176, Aug. 1989.

[26] K. Hirobe and H. Azuma, "Reduction of Radiation Damage on Silicon Substrates in Magnetron Reactive Ion Etching," *J. Electrochem. Soc.*, vol. 132, no. 4, pp. 938–942, Apr. 1985.

[27] K. Eriguchi, Y. Nakakubo, A. Matsuda, Y. Takao, and K. Ono, "Model for Bias Frequency Effects on Plasma-Damaged Layer Formation in Si Substrates," *Jpn. J. Appl. Phys.*, vol. 49, 056203, May 2010.

[28] S. A. Vitale and B. A. Smith, "Reduction of silicon recess caused by plasma oxidation during high-density plasma polysilicon gate etching," *J. Vac. Sci. Technol. B*, vol. 21, no. 5, pp. 2205–2211, Sep. 2003.

[29] L. Desvoivres, L. Vallier, and O. Joubert, "Sub-0.1 μm gate etch processes: Towards some limitations of the plasma technology?," *J. Vac. Sci. Technol. B*, vol. 18, no. 1, pp. 156–165, Jan. 2000.

[30] M. Fukasawa, Y. Nakakubo, A. Matsuda, Y. Takao, K. Eriguchi, K. Ono, M. Minami, F. Uesawa, and T. Tatsumi, "Structural and electrical characterization of HBr/O_2 plasma damage to Si substrate," *J. Vac. Sci. Technol. A*, vol. 29, 041301, Jun. 2011.

[31] K. Eriguchi, A. Matsuda, Y. Nakakubo, M. Kamei, H. Ohta, and K. Ono, "Effects of Plasma-Induced Si Recess Structure on n-MOSFET Performance Degradation," *IEEE Electron Device Lett.*, vol. 30, no. 7, pp. 712–714, Jul. 2009.

[32] Y. Nakakubo, A. Matsuda, M. Kamei, H. Ohta, K. Eriguchi, and K. Ono, "Analysis of Si Substrate Damage Induced by Inductively Coupled Plasma Reactor with Various Superposed Bias Frequencies," in *Emerging Technologies and Circuits*, vol. 2021, A. Amara, T. Ea, and M. Belleville, Eds. Dordrecht: Springer, 2010, pp. 107–120.

[33] K. Eriguchi, Y. Nakakubo, A. Matsuda, Y. Takao, and K. Ono, "Plasma-Induced

Defect-Site Generation in Si Substrate and Its Impact on Performance Degradation in Scaled MOSFETs," *IEEE Electron Device Lett.*, vol. 30, no. 12, pp. 1275–1277, Dec. 2009.

[34] N. Yabumoto, M. Oshima, O. Michikami, and S. Yoshii, "Surface Damage on Si Substrates Caused by Reactive Sputter Etching," *Jpn. J. Appl. Phys.*, vol. 20, no. 5, pp. 893–900, May 1981.

[35] G. S. Oehrlein, R. M. Tromp, Y. H. Lee, and E. J. Petrillo, "Study of silicon contamination and near-surface damage caused by CF_4/H_2 reactive ion etching," *Appl. Phys. Lett.*, vol. 45, no. 4, pp. 420–422, Aug. 1984.

[36] G. S. Oehrlein, R. M. Tromp, J. C. Tsang, Y. H. Lee, and E. J. Petrillo, "Near-Surface Damage and Contamination after CF_4/H_2 Reactive Ion Etching of Si," *J. Electrochem. Soc.*, vol. 132, no. 6, pp. 1441–1447, Jun. 1985.

[37] G. S. Oehrlein, "Dry etching damage of silicon: A review," *Mater. Sci. Eng. B*, vol. 4, no. 1–4, pp. 441–450, Oct. 1989.

[38] A. Agarwal, T. E. Haynes, D. J. Eaglesham, H.-J. Gossmann, D. C. Jacobson, J. M. Poate, and Y. E. Erokhin, "Interstitial defects in silicon from 1–5 keV Si^+ ion implantation," *Appl. Phys. Lett.*, vol. 70, no. 25, pp. 3332–3334, Jun. 1997.

[39] M. T. Robinson and I. M. Torrens, "Computer simulation of atomic-displacement cascades in solids in the binary-collision approximation," *Phys. Rev. B*, vol. 9, no. 12, pp. 5008–5024, Jun. 1974.

[40] S. Tian, M. F. Morris, S. J. Morris, B. Obradovic, Geng Wang, A. F. Tasch, and C. M. Snell, "A detailed physical model for ion implant induced damage in silicon," *IEEE Trans. Electron Devices*, vol. 45, no. 6, pp. 1226–1238, Jun. 1998.

[41] J. P. Biersack and L. G. Haggmark, "A Monte Carlo computer program for the transport of energetic ions in amorphous targets," *Nucl. Intsrum. Methods*, vol. 174, no. 1–2, pp. 257–269, Aug. 1980.

[42] K. Eriguchi, Y. Nakakubo, A. Matsuda, M. Kamei, Y. Takao, and K. Ono, "Trade-Off Relationship between Si Recess and Defect Density Formed by Plas-

ma-Induced Damage in Planar Metal–Oxide–Semiconductor Field-Effect Transistors and the Optimization Methodology," *Jpn. J. Appl. Phys.*, vol. 50, 08KD04, Aug. 2011.

[43] H. G. Grimmeiss, M. Kleverman, J. Olajos, and P. Omling, "Electronic defect characterization in silicon," *J. Electron. Mater.*, vol. 19, no. 8, pp. 837–849, Aug. 1990.

[44] K. S. Jones, S. Prussin, and E. R. Weber, "A systematic analysis of defects in ion-implanted silicon," *Appl. Phys. A*, vol. 45, no. 1, pp. 1–34, Jan. 1988.

[45] S. Takeda, "An Atomic Model of Electron-Irradiation-Induced Defects on {113} in Si," *Jpn. J. Appl. Phys.*, vol. 30, part 2, no. 4A, pp. L639–L642, Apr. 1991.

[46] H. Nishizawa, F. Hori, and R. Oshima, "In-situ HRTEM observation of the melting-crystallization process of silicon," *J. Cryst. Growth*, vol. 236, pp. 51–58, Mar. 2002.

[47] S. Perkowitz, D. G. Seiler, and W. M. Duncan, "Optical Characterization in Microelectronics Manufacturing," *J. Res. Natl. Inst. Stand. Technol.*, vol. 99, no. 5, pp. 605–639, Sep.–Oct. 1994.

[48] D. K. Schroder, *Semiconductor Material and Device Characterization*, 3rd ed. John Wiley & Sons, 2006.

[49] 藤原裕之, 分光エリプソメトリー, 第2版, 東京: 丸善, 2011.

[50] D. E. Aspnes, "Spectroscopic Ellipsometry of Solids," in *Optical Properties of Solids – New Developments*, B. O. Seraphin, Ed., Amsterdam: North-Holland, 1976.

[51] F. H. Pollak and H. Shen, "Modulation spectroscopy of semiconductors: bulk/thin film, microstructures, surfaces/interfaces and devices," *Mater. Sci. Eng. R*, vol. 10, no. 7–8, pp. 275–374, Oct. 1993.

[52] M. Cardona, *Modulation Spectroscopy* (Solid State Physics, Suppl. 11). New York: Academic Press, 1969.

[53] K. Eriguchi, A. Ohno, D. Hamada, M. Kamei, H. Fukumoto, and K. Ono, "Quantitative characterization of plasma-induced defect generation process in exposed

thin Si surface layers," *Jpn. J. Appl. Phys.*, vol. 47, no. 4, pp. 2446–2451, Apr. 2008.

[54] K. Eriguchi, A. Ohno, D. Hamada, M. Kamei, and K. Ono, "Estimation of defect generation probability in thin Si surface damaged layer during plasma processing," *Thin Solid Films*, vol. 516, no. 19, pp. 6604–6608, Aug. 2008.

[55] H. Wada, M. Agata, K. Eriguchi, and A. Fujimoto, "Photoreflectance characterization of the plasma-induced damage in Si substrate," *J. Appl. Phys.*, vol. 88, no. 5, pp. 2336–2341, Sep. 2000.

[56] M. Murtagh, S. M. Lynch, P. V. Kelly, S. Hildebrandt, P. A. F. Herbert, C. Jeynes, and G. M. Crean, "Photoreflectance characterisation of Ar^+ ion etched and $SiCl_4$ reactive ion etched silicon (100)," *Mater. Sci. Tech.*, vol. 13, no. 11, pp. 961–964, Nov. 1997.

2. Techniques

2.1. Plasma reactors

To generate artificial low-pressure plasmas in laboratory scale, the electrons must be heated to sustain their ionized states (Fig. 2.1). Typical methods to heat the electrons involve the use of electric and/or magnetic fields. The field preferentially accelerates the electrons, which are lighter and more mobile. Electrons exchange energy efficiently with other electrons, while the heavy ions exchange energy with other ions or background gas. This results in a non-equilibrium state, $T_e \gg T_i$, where T_e (typically ≈ 1–10 eV) is the electron temperature and T_i is the ion temperature [1]. (This is in contrast to interstellar plasma in the universe, which is in thermal equilibrium: $T_e = T_i$.)

Plasma sources are classified by how the electrodes or antennas are configured and by how the energy is transferred to the electrons. Common types include capacitively coupled plasma (CCP), inductively coupled plasma (ICP), and wave-heated plasmas (*e.g.* electron cyclotron resonance, helicon discharges). In this study, we employed CCP and ICP. Simplified diagrams of typical CCP and ICP reactors are shown in Fig. 2.2 and Fig. 2.3 respectively. Both types of plasma are driven by a radio frequency (RF) power source. A typical CCP reactor may have one of the electrodes as the driving electrode. A capacitively coupled discharge is sustained by a combination of ohmic heating, stochastic heating, and secondary electrons from the electrode surface [1]. On

the other hand, a typical ICP reactor has a coil (either cylindrical or planar) that is coupled to the plasma through a dielectric window. The coil generates an oscillating magnetic field, which induces an oscillating electric field within the chamber, heating the electrons in the chamber [1], [2].

Due to the difference in mobility between the positive ion and the electron, the bulk plasma is always charged positive with respect to the chamber walls [1]. This is called the plasma potential (V_p). Along the chamber walls and other solid that comes into contact with the plasma, a space-charged region is formed, called the "sheath." When an electrode is driven by a RF power, a "self-bias" potential (V_dc) appears on the electrode. As illustrated in Fig. 2.4, the mean incident energy ($\bar{E}_\mathrm{i}$) of the ions entering the self-biased electrode can be expressed as

$$\bar{E}_\mathrm{i} = e(V_\mathrm{p} - V_\mathrm{dc}) \ , \tag{2.1}$$

where e is the elementary charge. In the experiments, a Langmuir probe can be used to determine V_p, as well as the electron density (n_e), the electron temperature ($\mathrm{T_e}$), and the floating potential (V_f). V_dc was monitored by an oscilloscope connected to the driven electrode.

In actual plasma etching processes, a wide variety of chemically reactive gases are used, such as halogen-based gases for Si, C_xF_y or $C_xH_yF_z$ for SiO_2, Cl_2 for Al, *etc.* [1]. Other gases might be added to adjust the densities of the reactive species, create passivation layers, or to stabilize the discharge. Gas chemistry is a profound art in itself, but the experiments in this study employed noble gases (namely Ar and He) to eliminate chemical reactions, because the focus of this study is on physical effects.

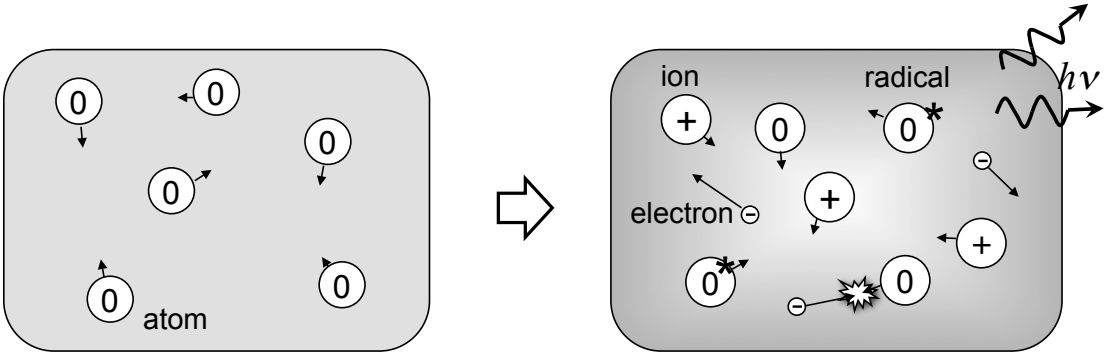

Fig. 2.1 Generating plasma from gas.

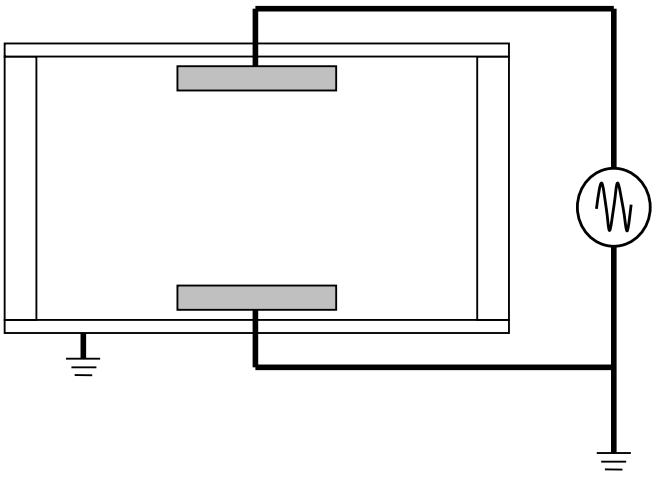

Fig. 2.2 A simplified diagram of a typical CCP reactor.

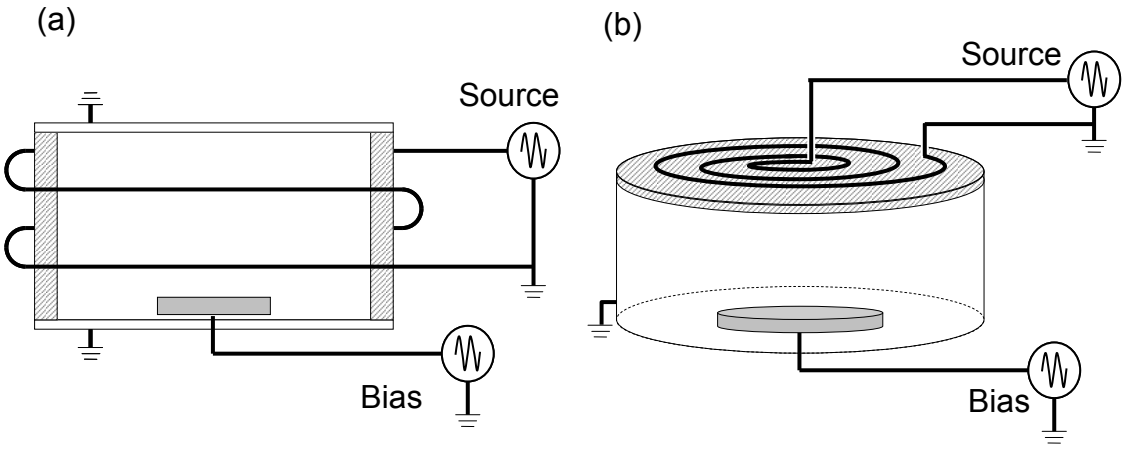

Fig. 2.3 Simplified diagrams of typical ICP reactors in (a) cylindrical and (b) planar geometries. Striped areas indicate dielectric windows.

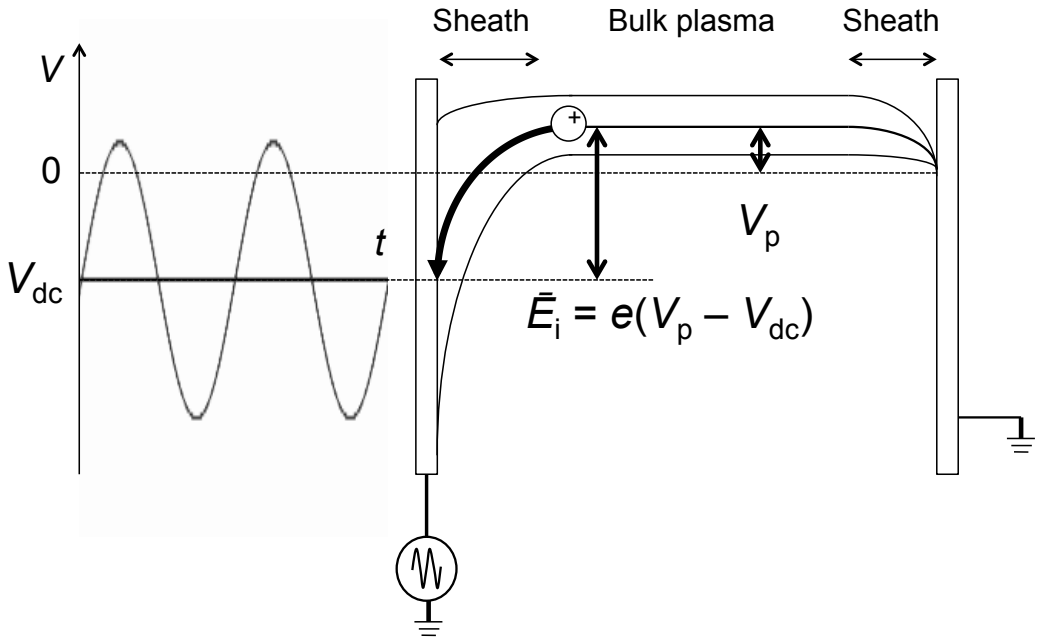

Fig. 2.4 A one-dimensional schematic illustration of a plasma and its sheath. Two electrodes oppose each other: one grounded and another driven with RF power. Actual configurations typically include a blocking capacitor and a matching network (not illustrated). The mean incident energy of the ions entering the driven electrode is the sum of the plasma potential V_p and the DC self-bias voltage V_{dc}.

2.2. Molecular dynamics

As described in chapter 1, our primary interest in this work concerns the nanoscale structures of plasma-exposed solid surfaces. Unfortunately, it is extremely difficult to perform nanoscale measurements of the surface reactions *in situ* (to observe in its place as it is occurring) [3]. Atomic-scale simulations compensate for this difficulty and give us insight into the surface structure and reaction mechanisms on solid surfaces.

Classical molecular dynamics simulation is one of the techniques to address this. Molecular dynamics (MD) simulations postulate an interatomic potential (Φ) as a function of positions of the atoms: $\Phi(\mathbf{r}_1, \mathbf{r}_2, \ldots, \mathbf{r}_N)$, where N is the total number of atoms in the simulation. The force acting on each atom (atom i) at a given time, t, is calculated from the potential, and the atoms interact with each other under the Newton's equation of motion,

$$\frac{\mathrm{d}^2\mathbf{r}_i}{\mathrm{d}t^2} = -\frac{1}{m_i}\frac{\partial \Phi}{\partial \mathbf{r}_i}, \tag{2.2}$$

to calculate the positions of the atoms in the next time step $t + \Delta t$ (Fig. 2.5); where $\mathbf{r}_i$ and m_i are the position and mass of the atom i, respectively. It is for this reason that the technique is labeled as "classical." *

Clearly, the outcome of the simulation depends on Φ, as it directly determines the movements of the atoms. For this reason, various potential models have been proposed. Most primarily, the potential only determines the

* However, this does not imply total negligence of quantum-mechanical effects. The potential may be constructed using results from *ab-initio* (first-principle) calculations, where the quantum-mechanical effects indirectly affect the outcome of the simulation. This is the case for the simulation in this work. See also the appendix.

force between two atoms, which is typically a function of the interatomic distance. Commonly used two-body potential models ($v_2(i,j)$) include the Lennard-Jones potential [4], the Morse potential [5], and the Molière potential [6] (refer to a literature by Torrens [7] for a comprehensive discussion). For forces between three or more atoms,

$$\Phi = \sum_{i,j}^{N} v_2(i,j) + \sum_{i,j,k}^{N} v_3(i,j,k)\,, \tag{2.3}$$

where the three-body potential $v_3(i,j,k)$ may be a function of the angle between the atoms (Stillinger–Weber potential [8]) or the bond order (*e.g.* the Tersoff potential [9]).

In this work, we applied the potential set and codebase by Watanabe *et al.* [10] and Ohta *et al.* [3], [11], [12]. The potential set is based on the Stillinger–Weber potential and the Molière potential, and is intended for simulations on Si–O–Ha (where Ha is halogen: F, Cl, or Br) and Si–O–Ar systems. The Stillinger–Weber potential is constructed to minimize the lattice energy of the tetrahedrally bonded structures *(sp^3)* in crystalline silicon. The Molière potential describes the Coulomb potential and its screening between atoms, and therefore is suited to model interactions involving noble gas atoms. See the appendix for details on the potential set.

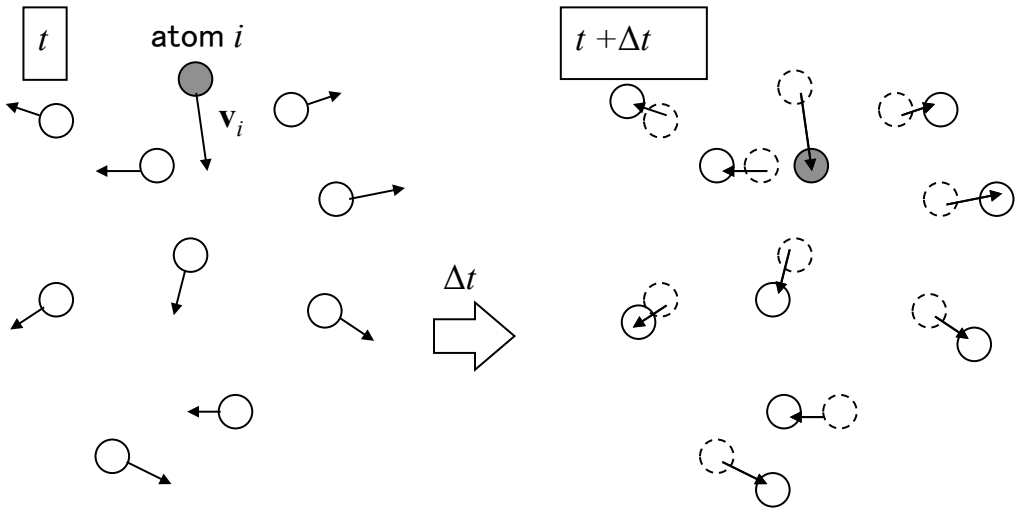

Fig. 2.5 Classical molecular dynamics simulation.

2.3. Spectroscopic ellipsometry

Ellipsometry [13]–[15] is an optical surface analysis technique where a beam of light is irradiated on the sample surface at an angle, and the polarization of the reflected light is monitored to obtain information about the surface [16]. The name "ellipsometry" stems from the fact that generally, the observed reflected light is elliptically polarized.

Early attempts at what can now be labeled as "ellipsometry" date back to the first half of the 19th century [17]. Drude laid down most of the theoretical foundation around 1890 [18], [19]. However, these earlier methodologies were cumbersome and gave relatively small amount of information. It was not until 1975 that a measurement over a wide range of photon energy—spectroscopic ellipsometry (SE)—was made possible, by using an automated procedure developed by Aspnes and Studna [20]. Since then, SE has been applied to various materials: metals, semiconductors, insulators, and organic/biological materials [13]. SE offers very high depth resolution, where monolayer (~ 0.1 nm) precision is achievable with a well-aligned ellipsometer [15]. The intensity of the light is weak, so the surface is not altered by the measurement. Modern apparatus allow for real-time, *in situ* measurements of the sample surface as it is being processed. Owing in part to these merits, SE is widely used as in-line monitors in production lines in the microelectronics industry [15], [21].

In an ellipsometric measurement, the sample surface is assumed to be a stack of uniform layers: ambient, layer 1, layer 2, ... , layer j, ... , layer m, and the substrate. Each layer j is uniform in the lateral direction, and its thickness in the vertical direction is d_j. The refractive index and the extinction coefficient spectra of layer j — $n_j(E)$ and $k_j(E)$, respectively — must be different from

the adjacent layers $j \pm 1$. Linearly polarized light is irradiated on the surface at an angle (ϕ). If we observe the reflected light, we can expect a change in the amplitude ratio and a shift in the phase between between the p and s components of polarized light. This relationship between the amplitude ratio spectrum $\Psi(E)$ and the phase shift spectrum $\Delta(E)$ is described by the fundamental equation of ellipsometry [13]:

$$\rho(E) = \frac{r_p}{r_s} = \tan(\Psi)\exp(i\Delta) \tag{2.4}$$

where r_p and r_s are the reflection coefficients of the p and s components. The spectrum $\rho(E)$ is called the complex refractive ratio and is a function of ϕ, d_j, $n_j(E)$, and $k_j(E)$ — tied to each other by Fresnel equations. $n_j(E)$ and $k_j(E)$ can be consolidated into a single complex quantity, the complex refractive index $N_j(E) \coloneqq n_j - ik_j$. The extinction coefficient $k(E)$ is tied to the absorption coefficient $\alpha(E)$ of the material.

$$\alpha(E) = \frac{4\pi k(E)}{\lambda}, \tag{2.5}$$

where λ is the wavelength of light in vacuum. For transparent materials, $k = 0$ ($\alpha = 0$). For opaque or semitransparent materials, term refractive index may refer to N rather than n.

For common and well-defined materials, values for $N_j(E)$ are available as tabulated database [22], reducing the unknown parameter for the layer j to only d_j. For a layer of material with a more complicated characteristic incorporating multiple materials, effective medium approximation (EMA) can combine the dielectric functions of the multiple constituents to give the "effective dielectric function" of the unknown layer. In this case, the volume fraction of a constituent f_j is added to the set of unknown

parameters. When $N_j(E)$ is completely unknown, it can be modeled in various formulations such as the Lorentz model (harmonic oscillator approximation), the Sellmeier/Cauchy models (for transparent materials), the Tauc–Lorentz model (for amorphous materials), and the Drude model (for metals and free-carrier absorptions in semiconductors) [13]. Several parameters are added to the set of unknown parameters in these models.

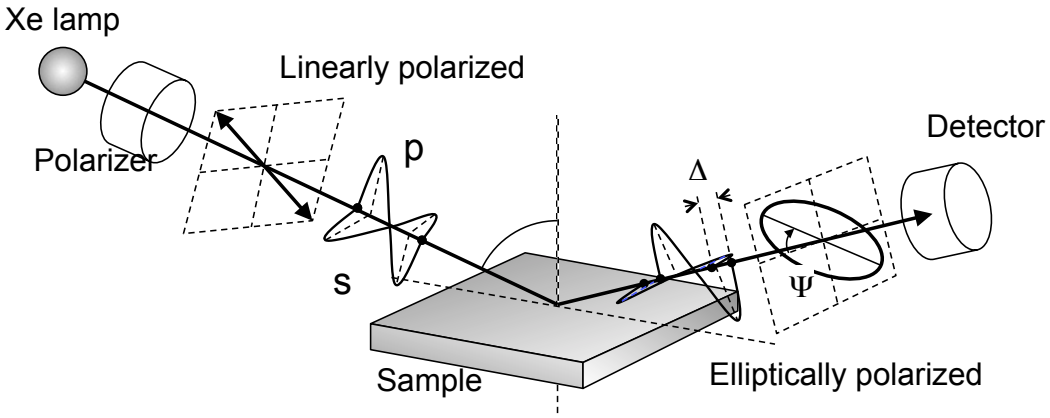

Fig. 2.6 Schematics of spectroscopic ellipsometry.

2.4. Photoreflectance spectroscopy

Photoreflectance spectroscopy (PRS) belongs to a class of measurements called modulation spectroscopy, which has been developed to obtain detailed information on band structures of semiconductors [23]–[26]. While a large portion of recent PRS-related publications deals with compounds semiconductors such as GaAs, GaN, and InAlAs [26]–[30], focusing on Si is not unprecedented [31], [32]; and in fact, modulation spectroscopy has played a considerable role in establishing today's understanding of the Si band structure. To the author's knowledge, PRS was first applied to address ion-bombardment damage on GaAs in 1993 [28], [33]; and on Si, 1997 [34], [35]. Since then, it has been used to address damage on Si [36]–[39], but as of the time of this writing, it is not as widely utilized as ellipsometry for the purpose of damage characterization.

A schematic diagram of the Si band structure is illustrated in Fig. 2.7(a). When Si is irradiated with photons of sufficient energy (E), an electron in the material experiences an interband transition as indicated by solid arrows at one of the several critical points (E_0', E_1, E_2) [40]. Si has an indirect band gap ($E_{\mathrm{gi}} = 1.12$ eV); indirect transition requires phonon interaction. The density of state that can be involved in the transitions is called the joint density of state $J(E)$. The absorption coefficient $\alpha(E)$ is proportional to $J(E)$ [24], and we can see corresponding structures in its spectrum as shown in Fig. 2.7(b): the E_1 edge [(E_0', E_1) complex] near $E \cong 3.4$ eV and the E_2 edge near $E \cong 4.2$ eV. The E dependence of the $\alpha(E)$ ($\propto J(E)$) is significantly different between energies below and above the critical point [24]. In other words, the slope changes significantly at the critical point, as we can observe from Fig. 2.7(b), and we can expect that the derivative form would have a sharp peak.

Modulation spectroscopy deals with this by perturbing the solid in some way. The perturbation adds a perturbation term $\mathcal{H}'$ to the Hamiltonian of the unperturbed crystal, $\mathcal{H}_0$:

$$\mathcal{H} = \mathcal{H}_0 + \mathcal{H}' = \frac{p^2}{2m} + V(\mathbf{r}) + \mathcal{H}', \tag{2.6}$$

where $\mathbf{p}$ is the electron momentum ($p = |\mathbf{p}|$), m is the electron mass, and $V(\mathbf{r})$ is a periodic potential for the lattice [41]. $\mathcal{H}'$ can be induced by various external perturbations, such as stress and temperature changes. When these perturbations are used for reflection modulation experiments, the techniques are called piezoreflectance and thermoreflectance, respectively [23]. When the perturbation is an electric field, $\boldsymbol{\mathcal{E}}$, the technique is called electroreflectance. In this case, $\mathcal{H}' = e\boldsymbol{\mathcal{E}} \cdot \mathbf{r}$ and translational invariance of the Hamiltonian is lost in the field direction [41]. When a low electric field is turned on, it accelerates the band electron, causing a discontinuity in the second-order term of the time-dependent average energy of the band electron. Transforming into the frequency domain, we see a third-order change in $\varepsilon(E)$ [25], [42]. A change in the dielectric function, $\Delta\varepsilon$, induces a change in the reflectivity, ΔR, as phenomenologically described by Seraphin and Bottka as [43]

$$\frac{\Delta R}{R} = \alpha(\varepsilon_1, \varepsilon_2)\Delta\varepsilon_1 + \beta(\varepsilon_1, \varepsilon_2)\Delta\varepsilon_2 , \tag{2.7}$$

where α and β are called Seraphin coefficients. Further consideration reveals that for quantitative analysis, the contributions of electron–hole Coulomb interactions (C_{ex}) and the effect of spatial inhomogeneity of the perturbing field (C_{in}) must be taken into account. $\Delta R/R$ has been generalized by Aspnes [41] to include these effects as

$$\frac{\Delta R}{R} = \Re\left[C_{\mathrm{s}} C_{\mathrm{ex}} C_{\mathrm{in}} \hat{e}^i \hat{e}^j \Delta\varepsilon^{ij}\right], \tag{2.8}$$

where $\hat{e}^i, \hat{e}^j$ represent Cartesian components of the unit polarization vector $\hat{\mathbf{e}}$. C_{s} can be rewritten as $C_{\mathrm{s}} = \alpha(\varepsilon_1, \varepsilon_2) - i\beta(\varepsilon_1, \varepsilon_2)$, which is directly expressed by the Seraphin coefficients. $\Delta\varepsilon^{ij}$ is $\Delta\varepsilon$ (second-rank tensor) in component form,

$$\Delta\varepsilon^{ij}(\mathcal{E}, \Gamma, E) \cong \frac{e^2\hbar^2\mathcal{E}^k\mathcal{E}^l}{24E^2}(\mu^{-1})^{kl}\frac{\partial^3}{\partial E^3}\left(E^2\varepsilon^{ij}(\Gamma, E)\right), \tag{2.9}$$

where Γ is the broadening parameter (related to the lifetime), e is the elementary charge, $\hbar$ is the reduced Planck constant, and μ is the effective mass (second-rank tensor). Summations over indices k and l are assumed. See literature [25], [42] for further details. Eq. (2.9) tells us that $\Delta\varepsilon$ can be expressed with a third-derivative function of the unperturbed dielectric function, and hence, low-field electroreflectance is known as *third-derivative modulation spectroscopy* [41]. Assuming parabolic model densities of states,

$$\Delta\varepsilon^{ij} \propto \mathcal{E}^2\left(E - E_{\mathrm{g}} + i\Gamma\right)^{-n}, \tag{2.10}$$

where n is a parameter that depends of the dimensionality of the critical point. (This matter is discussed in chapter 5.) From Eqs. (2.8) and (2.10), the lineshape of $\Delta R/R$ can be expressed in the generic form,

$$\frac{\Delta R}{R}(E) = \Re\left[C\mathrm{e}^{i\theta}\left(E - E_{\mathrm{g}} + i\Gamma\right)^{-n}\right], \tag{2.11}$$

where C is called the amplitude factor, θ the phase factor, and E_{g} is the direct transition energy at a critical point. A typical PRS spectrum for N-type Si(100) (resistivity 0.02 Ωcm) is shown in Fig. 2.8. The peak that corresponds to the E_1 edge [(E_0', E_1) complex] is visible at $E \cong 3.4$ eV. The energy of the peak

is determined by E_g. The spectral broadening is expressed by Γ. The amplitude of the peak is scaled linearly by C, and is also affected by Γ and n.

To realize electroreflectance, one might prepare a film of transparent electrode on the sample surface to generate the electric field as depicted in Fig. 2.9(a) [44]. Alternatively, modulation of the electric field could be caused by excited electron–hole pairs created by the pump source (laser or other light source) [26], as illustrated in Fig. 2.9(b). This extension of the electroreflectance technique is called photoreflectance (PR)—where the pump beam creates photo-injected electron–hole pairs, which modulate the built-in electric field of the semiconductor [26] (Fig. 2.10). In a PR measurement, the reflectivity (R) on the surface over a certain photon-energy (E) range is monitored by measuring the intensity of the "probe beam", while a secondary "modulation beam (pump beam)" is irradiated on the sample. The pumping induces a small change ($\Delta R \sim 10^{-5}$) in the intensity of the reflected probe beam [41]. To measure this small signal, the modulation beam could be chopped at a certain frequency, and the corresponding signal be retrieved by a lock-in amplifier. Many PR apparatuses utilize a mechanical chopper for this purpose, which allows for frequencies up to 5 kHz [26]. For higher frequencies up to about 1 MHz, an acousto-optic modulator may be used.

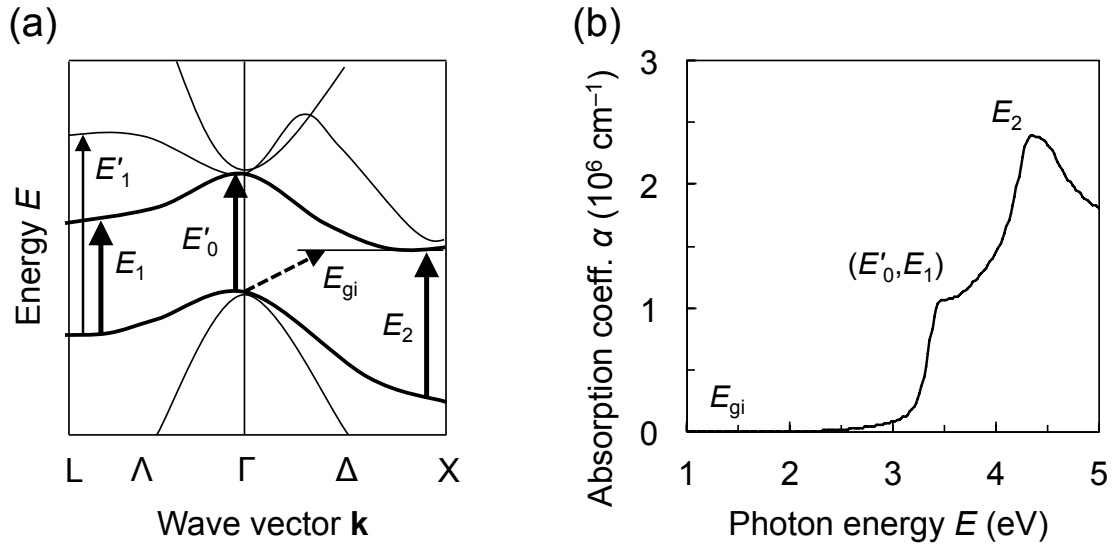

Fig. 2.7 (a) Schematic diagram of the Si band structure, after Adachi [40].
(b) Absorption coefficient of a clean crystalline Si, calculated by Eq. (2.5) using data compiled by Palik [22].

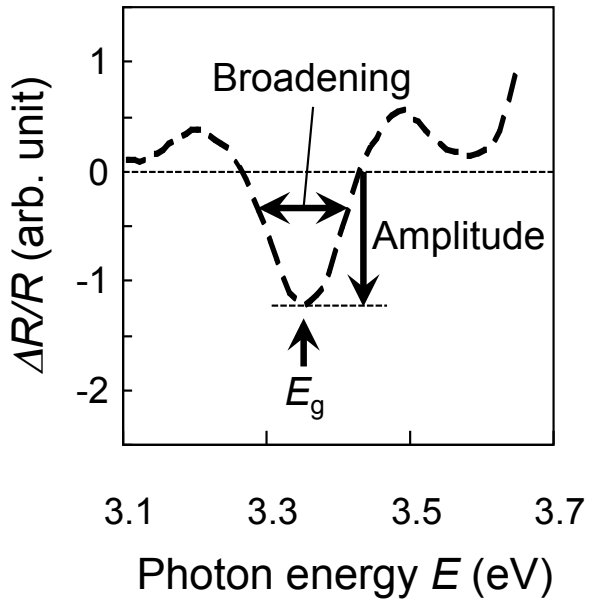

Fig. 2.8 A typical photoreflectance spectrum for N-type Si(100).

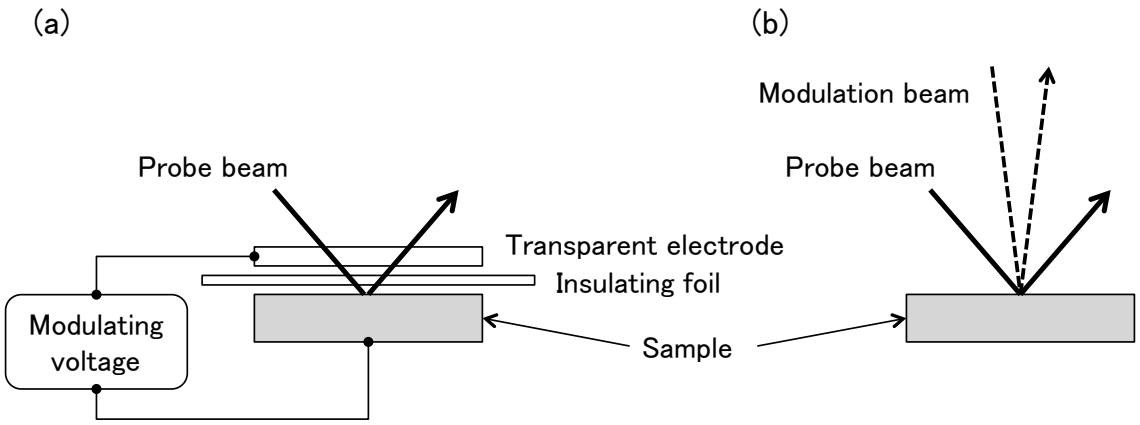

Fig. 2.9 (a) Schematic diagram of the sample arrangement for reflective electric field modulation experiments for semiconductors, after Cardona [23].
(b) Schematic diagram for photoreflectance experiments.

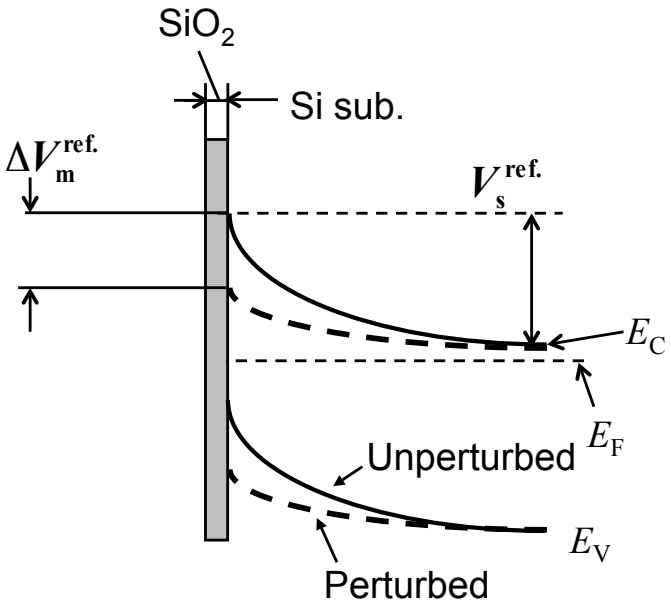

Fig. 2.10 Perturbation of the Si surface by irradiation of the modulation beam and the surface potential of Si. E_C: conduction band, E_F: Fermi level, and E_V: valence band.

2.5. References

[1] M. A. Lieberman and A. J. Lichtenberg, *Principles of Plasma Discharges and Materials Processing*, 2nd ed. Hoboken, NJ: Wiley, 2005.

[2] J. A. Meyer and A. E. Wendt, "Measurements of electromagnetic fields in a planar radio-frequency inductively coupled plasma source," *J. Appl. Phys.*, vol. 78, no. 1, pp. 90–96, Jul. 1995.

[3] H. Ohta and S. Hamaguchi, "Molecular dynamics simulation of silicon and silicon dioxide etching by energetic halogen beams," *J. Vac. Sci. Technol. A*, vol. 19, no. 5, pp. 2373–2381, Sep./Oct. 2001.

[4] J. E. Lennard-Jones, "On the Determination of Molecular Fields.—II. From the Equation of State of a Gas," *Proc. R. Soc. Lond. A*, vol. 106, no. 738, pp. 463–477, Oct. 1924.

[5] P. M. Morse, "Diatomic Molecules According to the Wave Mechanics. II. Vibrational Levels," *Phys. Rev.*, vol. 34, no. 1, pp. 57–64, Jul. 1929.

[6] G. Molière, "Therorie der Streuung schneller geladener Teilchen I. Einzelstreuung am abgeschirmten Coulomb-Feld," *Z. Naturforsch.*, vol. 2a, pp. 133–145, 1947.

[7] I. Torrens, *Interatomic Potentials*. New York: Academic Press, 1972.

[8] F. H. Stillinger and T. A. Weber, "Computer simulation of local order in condensed phases of silicon," *Phys. Rev. B*, vol. 31, no. 8, pp. 5262–5271, Apr. 1985.

[9] J. Tersoff, "Empirical interatomic potential for silicon with improved elastic properties," *Phys. Rev. B*, vol. 38, no. 14, pp. 9902–9905, Nov. 1988.

[10] T. Watanabe, H. Fujiwara, H. Noguchi, T. Hoshino, and I. Ohdomari, "Novel Interatomic Potential Energy Function for Si, O Mixed Systems," *Jpn. J. Appl. Phys.*, vol. 38, part 2, no. 4A, pp. L366–L369, Apr. 1999.

[11] H. Ohta and S. Hamaguchi, "Classical interatomic potentials for Si–O–F and Si–O–Cl systems," *J. Chem. Phys.*, vol. 115, no. 14, pp. 6679–6690, Oct. 2001.

[12] H. Ohta, A. Iwakawa, K. Eriguchi, and K. Ono, "An interatomic potential model for molecular dynamics simulation of silicon etching by Br^+-containing plasmas," *J. Appl. Phys.*, vol. 104, no. 7, 073302, Oct. 2008.

[13] 藤原裕之, 分光エリプソメトリー, 第 2 版, 東京: 丸善, 2011.

[14] D. E. Aspnes, "Spectroscopic Ellipsometry of Solids," in *Optical Properties of Solids – New Developments*, B. O. Seraphin, Ed. Amsterdam: North-Holland, 1976.

[15] E. A. Irene, "Applications of spectroscopic ellipsometry to microelectronics," *Thin Solid Films*, vol. 233, no. 1–2, pp. 96–111, Oct. 1993.

[16] E. Hecht, *Optics*, 4th ed. San Francisco: Addison-Wesley, 2002.

[17] U. Rossow, "The early history of ellipsometry," in *4th Int. Conf. Spectrosc. Ellipsom. Program & Abstr.*, Stockholm, Jun. 2007, p. 344.

[18] P. Drude, "Ueber die Gesetze der Reflexion und Brechung des Lichtes an der Grenze absorbirender Krystalle," *Ann. Phys. Chem.*, vol. 268, no. 12, pp. 584–625, 1887.

[19] K. Vedam, "Spectroscopic ellipsometry: a historical overview," *Thin Solid Films*, vol. 313–314, pp. 1–9, Feb. 1998.

[20] D. E. Aspnes and A. A. Studna, "High Precision Scanning Ellipsometer," *Appl. Opt.*, vol. 14, no. 1, pp. 220–228, Jan. 1975.

[21] D. K. Schroder, *Semiconductor Material and Device Characterization*, 3rd ed. Hoboken, NJ: John Wiley & Sons, 2006. (Trans.: ディーター・K・シュロウダー, 半導体材料・デバイスの評価 —パラメータ測定と解析評価の実際—, 第 3 版. 嶋田恭博訳. 東京: シーエムシー出版, 2012.)

[22] E. D. Palik, *Handbook of Optical Constants of Solids*, vol. 1. Academic Press, 1997.

[23] M. Cardona, *Modulation Spectroscopy* (Solid State Physics, Suppl. 11). New York: Academic Press, 1969.

[24] 大成誠之助, 固体スペクトロスコピー. 東京: 裳華房, 1994.

[25] Y. Hamakawa and T. Nishino, "Recent advances in modulation spectroscopy," in *Optical Properties of Solids – New Developments*, B. O. Seraphin, Ed. Amsterdam: North-Holland, 1976.

[26] F. H. Pollak and H. Shen, "Modulation spectroscopy of semiconductors: bulk/thin film, microstructures, surfaces/interfaces and devices," *Mater. Sci. Eng. R*, vol. 10, no. 7–8, pp. 275–374, Oct. 1993.

[27] T. Kanata, M. Matsunaga, H. Takakura, Y. Hamakawa, and T. Nishino, "Photoreflectance characterization of surface Fermi level in as-grown GaAs(100)," *J. Appl. Phys.*, vol. 68, no. 10, pp. 5309–5313, Nov. 1990.

[28] H. Nakanishi and K. Wada, "Plasma-Induced Damage Behavior in GaAs by Photoreflectance Spectroscopy," *Jpn. J. Appl. Phys.*, vol. 32, pp. 6206–6209, Dec. 1993.

[29] U. Behn, A. Thamm, O. Brandt, and H. T. Grahn, "Unpinned behavior of the surface Fermi level of GaN detected by photoreflectance spectroscopy," *J. Appl. Phys.*, vol. 87, no. 9, pp. 4315–4318, May 2000.

[30] J. S. Hwang, G. S. Chang, W. C. Hwang, and W. J. Chen, "Photoreflectance studies of surface state density of InAlAs," *J. Appl. Phys.*, vol. 89, no. 3, pp. 1771–1776, Feb. 2001.

[31] F. Cerdeira and M. Cardona, "Photoreflectance and electroreflectance in silicon," *Solid State Commun.*, vol. 7, no. 12, pp. 879–882, Jun. 1969.

[32] H. Moriya, A. Kaneta, and S. Adachi, "Photoreflectance study of crystalline silicon," *Mater. Sci. Eng. B*, vol. 76, no. 3, pp. 232–236, Jul. 2000.

[33] M. Murtagh, P. V. Kelly, P. A. F. Herbert, M. O'Connor, G. Duffy, and G. M. Crean, "Photoreflectance investigation of dry-etch-induced damage in semi-insulating GaAs substrates," *Appl. Surf. Sci.*, vol. 63, no. 1–4, pp. 158–162, Jan. 1993.

[34] M. Murtagh, S. M. Lynch, P. V. Kelly, S. Hildebrandt, P. A. F. Herbert, C. Jeynes, and G. M. Crean, "Photoreflectance characterisation of Ar^+ ion etched and $SiCl_4$ reactive ion etched silicon (100)," *Mater. Sci. Tech.*, vol. 13, no. 11, pp. 961–964, Nov. 1997.

[35] K. Eriguchi, T. Imai, A. Asai, and M. Okuyama, "A new evaluation technique of plasma-induced Si substrate damage by photoreflectance spectroscopy," in *1997 2nd Int. Symp. Plasma Process-Induced Damage*, Monterey, CA, 1997, pp. 215–218.

[36] M. Agata, H. Wada, O. Maida, K. Eriguchi, A. Fujimoto, T. Kanashima, and M. Okuyama, "Optical Characterization of Gate Oxide Charging Damage by Photoreflectance Spectroscopy," *Jpn. J. Appl. Phys.*, vol. 39, part 1, no. 4B, pp. 2040–2044, Apr. 2000.

[37] H. Wada, M. Agata, K. Eriguchi, and A. Fujimoto, "Photoreflectance characterization of the plasma-induced damage in Si substrate," *J. Appl. Phys.*, vol. 88, no. 5, pp. 2336–2341, Sep. 2000.

[38] K. Eriguchi, A. Ohno, D. Hamada, M. Kamei, H. Fukumoto, and K. Ono, "Quantitative characterization of plasma-induced defect generation process in exposed thin Si surface layers," *Jpn. J. Appl. Phys.*, vol. 47, pp. 2446–2451, Apr. 2008.

[39] K. Eriguchi, A. Ohno, D. Hamada, M. Kamei, and K. Ono, "Estimation of defect generation probability in thin Si surface damaged layer during plasma processing," *Thin Solid Films*, vol. 516, no. 19, pp. 6604–6608, Aug. 2008.

[40] S. Adachi, "Model dielectric constants of Si and Ge," *Phys. Rev. B*, vol. 38, no. 18, pp. 12966–12976, Dec. 1988.

[41] D. E. Aspnes, "Third-derivative modulation spectroscopy with low-field electroreflectance," *Surf. Sci.*, vol. 37, pp. 418–442, Jun. 1973.

[42] Y. Hamakawa, T. Nishino, and M. Okuyama, "Lineshape Morphology in Modulation Spectroscopy," *Prog. Theor. Phys. Suppl.*, no. 57, pp. 125–137, 1975.

[43] B. O. Seraphin and N. Bottka, "Franz-Keldysh Effect of the Refractive Index in Semiconductors," *Phys. Rev.*, vol. 139, no. 2A, pp. A560–A565, Jul. 1965.

[44] S. Perkowitz, D. G. Seiler, and W. M. Duncan, "Optical Characterization in Microelectronics Manufacturing," *J. Res. Natl. Inst. Stand. Technol.*, vol. 99, no. 5, pp. 605–639, Sep.–Oct. 1994.

3. Structure of Damaged Layers and Optical Modeling

3.1. Introduction

After plasma etching, the wafer undergoes a wet treatment using diluted hydrofluoric acid solution (DHF), to clean the contaminated surface [1]. The wet-etch rates of ion-bombarded surfaces are relatively high, and the layers are easily removed by this process [2]–[5]. In the context of gate- or offset-spacer etching, the process results in a recessed structure in the source/drain extension regions, known as the Si recess or the Si loss [6]–[8]. Since the depth of the recess (d_{R}) is closely tied to the wet-etched depth d_{w} as

$$d_{\mathrm{R}} \cong -\alpha d_{\mathrm{gr}} + d_{\mathrm{w}} + d_{\mathrm{sp}} \tag{3.1}$$

(where d_{gr} is the thickness of SiO_2 formed on the etched surface, d_{sp} is the sputtered depth during overetch step, and the constant α is assumed to be 0.4 [9]), accurate measurement of the damaged layer thickness is a crucial matter.

Spectroscopic ellipsometry (SE) is a widely used technique in both laboratories and as monitors in production lines. An ellipsometry-based method to evaluate the damaged layer thickness would be extremely useful. Earlier studies exist where the damaged layer was optically modeled as a single layer of SiO_2 [8], [10]. However, they were not able to obtain a valid result that

agrees with the results obtained from other techniques. In fact, considering the nature of the damaged layer, it is inaccurate to assume its optical properties to be of bulk SiO_2. An optical model that is both consistent with the characteristics of physical damage and practical for in-line use is required. In this chapter, the structure, composition, and formation mechanisms were comprehensively studied by using both simulation and experiments in combination. The optical model that corresponds to the characteristics of the damaged layer as clarified above will be discussed. Finally, the established optical model will be utilized to discuss the incident ion energy ($\bar{E}_i$) dependence of physical damage. A simple flowchart of this process is illustrated in Fig. 3.2.

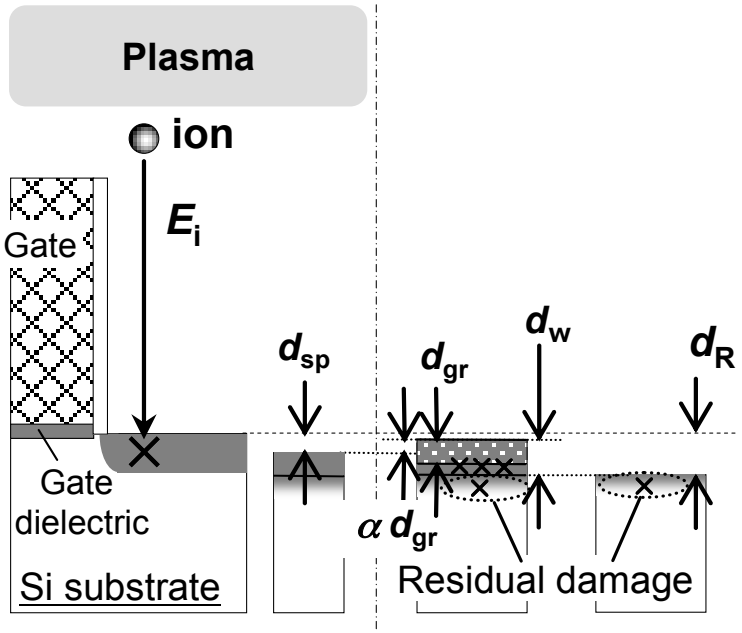

Fig. 3.1 Damaged layer thickness, wet-etched depth, and recess depth [9].

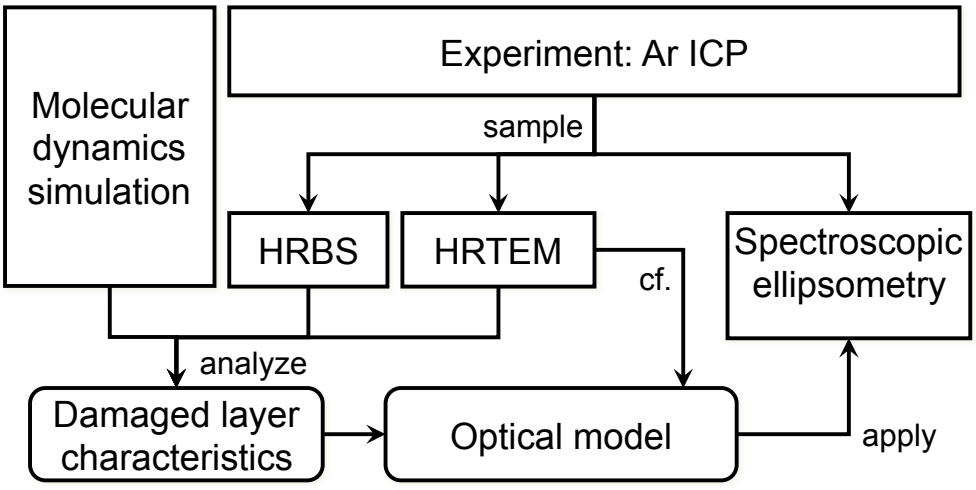

Fig. 3.2 Flowchart of the experiment in this chapter.

3.2. Simulation and experimental procedure

3.2.1. Molecular dynamics simulation

In order to investigate the formation mechanism and physical the structure of the damaged layer, we applied classical MD simulation [11], [12]. Stillinger–Weber type interatomic potentials for the Si–O–Ar systems were applied [13], [14]. The reader is referred to the appendix for details on this interatomic potential set. To reproduce the practical experimental condition, we constructed a scheme consisting of four simulation phases: (1) Si (100) structure with 1152 (= 8 × 8 × 18) atoms was prepared. (2) Low-energy O atoms were directed towards the surface until saturation, to emulate natural oxidation. (3) Ar^+ ions were impinged on the surface at certain incident energy E_i for 1000 times. Ar^+ ions that may remain beneath the surface are removed in this simulation. (4) Low-energy O atoms were directed to emulate post-process natural oxidation. Simulation domain was 2.17 nm in side length with periodic boundaries. E_i was varied, to simulate different bias voltages.

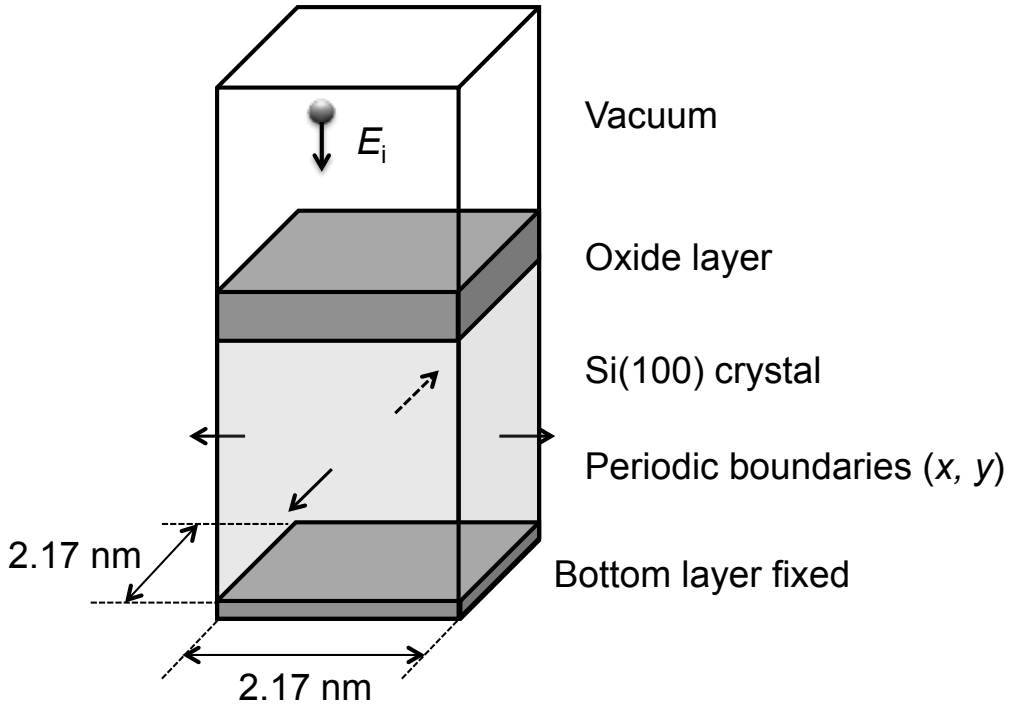

Fig. 3.3 Molecular dynamics simulation domain.

3.2.2. Plasma exposure

ICP reactor, illustrated in Fig. 3.4, was used. The chamber was made of stainless steel, and its dimensions were 25 cm in diameter and 30 cm in height. The chamber was vacuum-pumped by Seiko Seiki STP-H1000C turbo molecular pump (TMP). 13.56 MHz radio-frequency (RF) power supply was coupled to the plasma via a three-turn planar coil, positioned on a quartz window, located at the top of the chamber. Four-inch wafer stage was located at the bottom side of the chamber, where a ground shield surrounded the stage. The stage was coupled to a separate power supply system for biasing.

N-type Si (100) wafers (0.02 Ωcm) were placed on the stage and were exposed to argon plasma. Chamber pressure was 20 mTorr. Exposure time was 30 s. 13.56 MHz RF bias was applied to the wafer stage. Bias power (P_{bias}) was ranged from 0 W (no bias) to 400 W, to vary the mean energy of ions $\bar{E}_{\mathrm{i}}$ impinging onto wafer surface:

$$\bar{E}_{\mathrm{i}} = e(V_{\mathrm{p}} - V_{\mathrm{dc}}) , \tag{3.2}$$

where e is the elementary charge, V_{p} is the plasma potential determined using a Langmuir probe, and V_{dc} is the DC self-bias voltage of the sample stage, monitored using an oscilloscope.

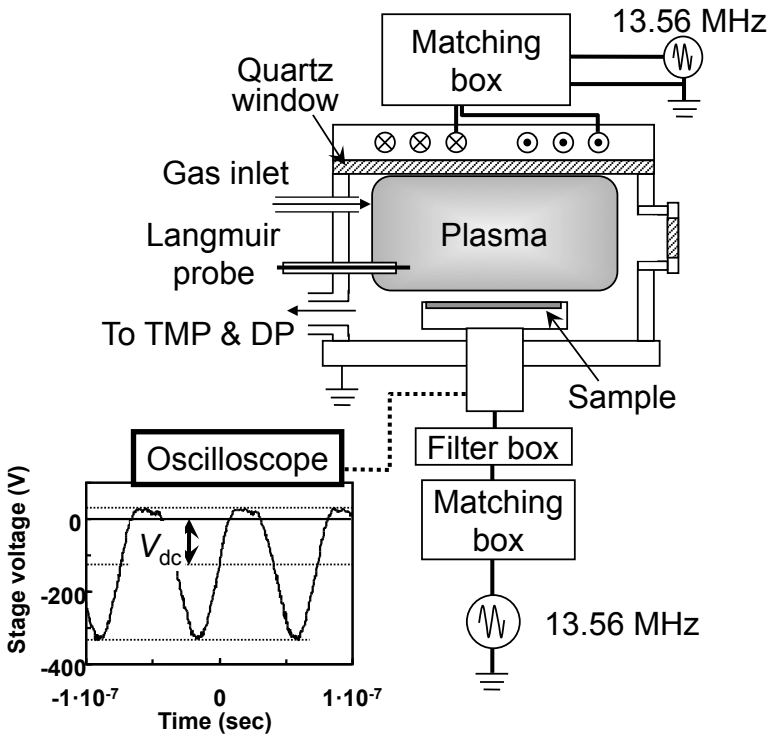

Fig. 3.4 The ICP chamber used in this experiment.

3.2.3. Composition analyses

To observe the surface structure and the layer thickness, some of the samples were examined by using cross-sectional high-resolution transmission electron microscopy (HRTEM). To determine the composition stoichiometry of the damaged layer, two of the samples (reference and $\bar{E}_i$ = 130 eV) were examined by using Rutherford backscattering spectrometry (RBS). 20 μC of He^+ beam was irradiated at 45° angle to obtain the aligned spectra and 50° to obtain the random spectra. For the reference sample, scattering angles of 50° and 55° were monitored; for the 130 eV sample, 55° and 77° were monitored. Ion energy was 300 keV for 50° and 55°; and 450 keV for 77°. Depth profile was obtained by simulation fitting.

3.2.4. Spectroscopic ellipsometry

The ellipsometric measurements were made using a rotating analyzer ellipsometer, SOPRA MOSS-MLM, with a xenon lamp as the light source. The beam diameter was 5×15 mm. Incident light angle was 75.2°, near the pseudo-Brewster angle of silicon. Measurements were carried out in the photon energy range of 1.60–5.50 eV at 0.05 eV intervals. To obtain the layer thickness and composition, the complex reflection ratio spectrum $\rho(E)$ must be fitted with an appropriate optical model that models the sample structure correctly (discussed later). The best fit was determined by regression analysis to minimize the unbiased estimator σ, defined as

$$\sigma = \frac{1}{\sqrt{M-P-1}} \left\{ \sum_{j=1}^{M} \left[\rho_{\exp}(E_j) - \rho_{\mathrm{mod}}(E_j) \right]^2 \right\}^{\frac{1}{2}}, \tag{3.3}$$

where M is the number of measurement points, P is the number of unknown parameters, and ρ_{exp} and ρ_{mod} are the experimental and modeled $\rho(E)$, respectively [15].

3.3. Results and discussion

3.3.1. Plasma conditions

Table 3.1 shows the plasma parameters obtained from Langmuir probe measurements [n_{e}: electron density, $\mathrm{T_e}$: electron temperature, V_{p}: plasma potential] and from oscilloscope [V_{dc} (< 0): DC self-bias voltage, V_{pp}: bias peak-to-peak voltage]. Also shown is the estimated mean energy of incident ions ($\bar{E}_{\mathrm{i}}$).

Table 3.1 Plasma parameters, bias voltages, and estimated incident ion energy.

P_{bias} (W)	n_{e} (10^{11} cm^{-3})	$\mathrm{T_e}$ (eV)	V_{p} (V)	V_{pp} (V)	V_{dc} (V)	$\bar{E}_{\mathrm{i}}$ (eV)
0	3.13	3.32	11.1	N/A	N/A	10
25	3.01	3.69	13.8	83	–33	50
50	2.99	3.73	14.0	180	–82	100
75	3.03	3.57	14.0	244	–115	130
100	3.04	3.52	14.2	276	–130	140
150	3.09	3.29	14.1	360	–161	180
200	3.14	3.13	14.4	438	–200	210
250	3.11	3.12	14.7	532	–246	260
300	3.08	3.15	15.2	604	–282	300
400	3.16	2.75	15.5	804	–400	420

3.3.2. Molecular dynamics simulation

The simulation was performed to correspond with the $\bar{E}_i$ obtained from the plasma experiment. Fig. 3.5 shows the results of the MD simulation. Si and O atoms on the topmost region were etched away at higher $\bar{E}_i$ conditions due to surface sputtering. Incident Ar^+ ions were observed to scatter the atoms and disarrange the crystalline structure. Also, events were observed wherein an ion collided with an O atom and caused the O atom to penetrate several nanometers into the substrate.

The resulting structure can be separated into four layers from the top: (1) surface SiO_2, (2) amorphous SiO_x ($x < 2$), (3) *c*-Si with occasional dislocated Si and interstitial atoms (both Si and O), and (4) *c*-Si, free of defects. Layer 1 was confirmed to be stoichiometric SiO_2 [graph in Fig. 3.5(c)]. Layers 2 and 3 were virtually nonexistent prior to plasma exposure, only a few monolayers thick for $\bar{E}_i$ = 50 eV, and increasingly thicker with higher $\bar{E}_i$. The transition from layer 2 to 3 was gradual, and had roughness of which its profile height was several monolayers. This structure is compared with the experiments in the following sections.

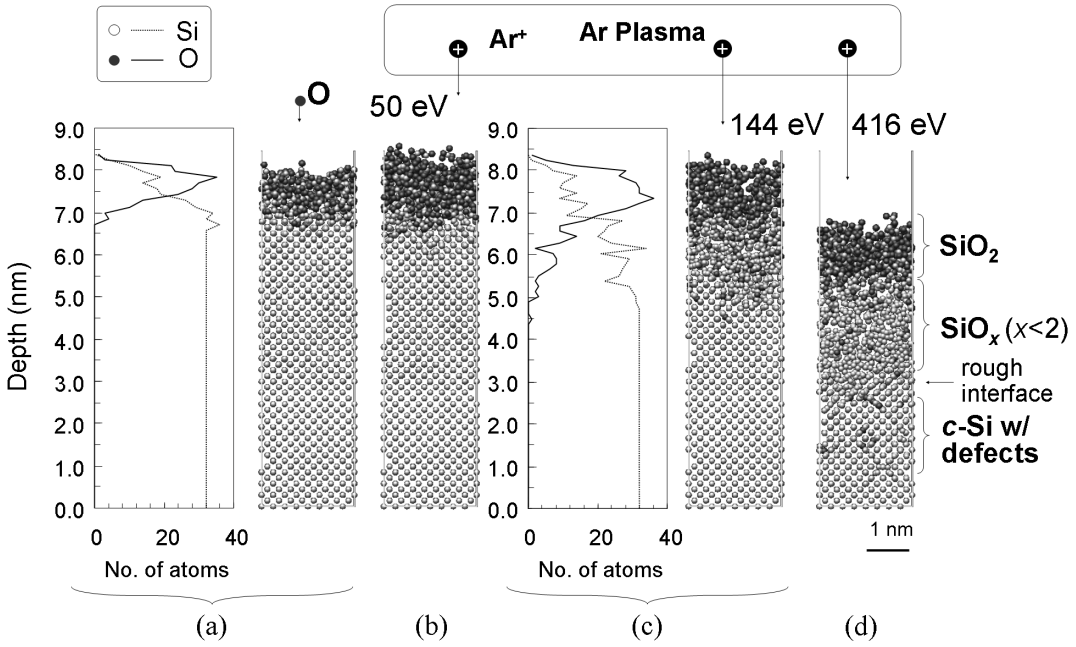

Fig. 3.5 Snapshots of the MD simulations.

(a) After natural oxidation (phase 2).

(b)–(d) After plasma exposure (phase 3; ion incident energy Ei is shown) and post-process oxidation (phase 4).

Atomic concentration are also shown for (a) and (c). Notice the change in the distribution of O atoms.

3.3.3. Composition and structure

Fig. 3.6 shows the cross-sectional HRTEM images for the wafers exposed to plasma with 100, 300, and 400 W bias power applied to the wafer stage. For all three samples, nanoscale crystallites protruding from the amorphous/crystalline interface towards the surface were observed. Fig. 3.7 shows the close-up view of the 300 W sample. In the crystalline region, features that may suggest the presence of defects can be observed. These were present only in 300 W and 400 W (Fig. 3.6). On a larger scale, notice localized shades in the crystalline region, near the interface. These may indicate the presence of uneven strain fields [16], [17] or segregated oxygen atoms [17], [18]. The thickness of the amorphized layer (including the rough interface) was 4.5 ± 0.1 nm for 100 W and 4.0 ± 0.1 nm for 300 W. Smaller thicknesses for 300 W may be attributed to surface sputtering. Disregarding the large wave-like features in the 400 W sample, the thickness was 2.5 ± 1.0 nm. The waves could be precursors of either nanocrystalline silicon dots [19] or ripples [20], [21] induced by ion bombardment in the higher energy range (commonly observed when $\bar{E}_i > 1$ keV).

The composition profile from the RBS analysis is shown in Fig. 3.8. Oxide layer of the exposed sample was thicker than that of the unexposed sample. Notice that the oxygen concentration for the exposed sample trails deeper towards the substrate (marked with arrows). This indicates that the exposed sample exhibits more gradual transition from the SiO_2 layer to the Si substrate.

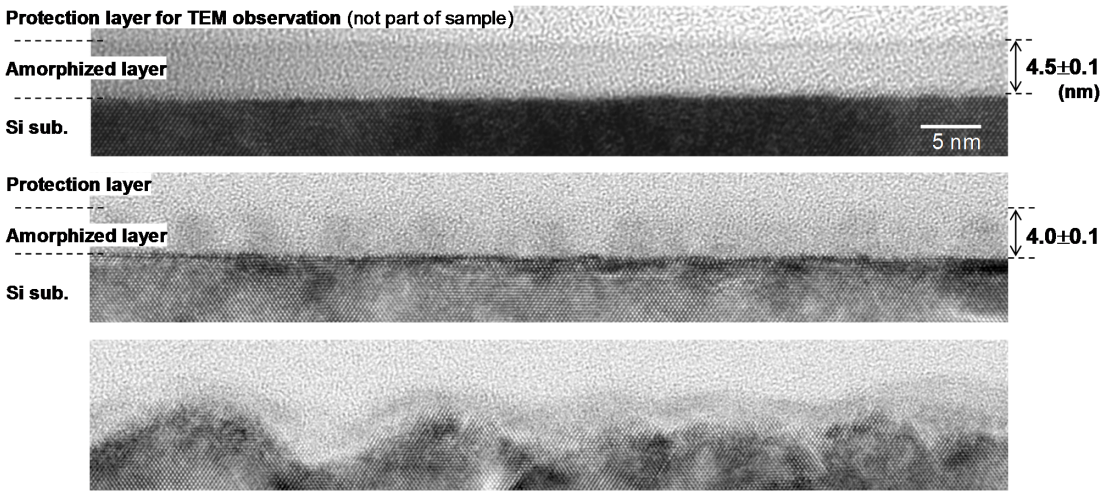

Fig. 3.6 Cross-sectional HRTEM images of the damaged wafers. From the top: 100 W, 300 W, and 400 W.

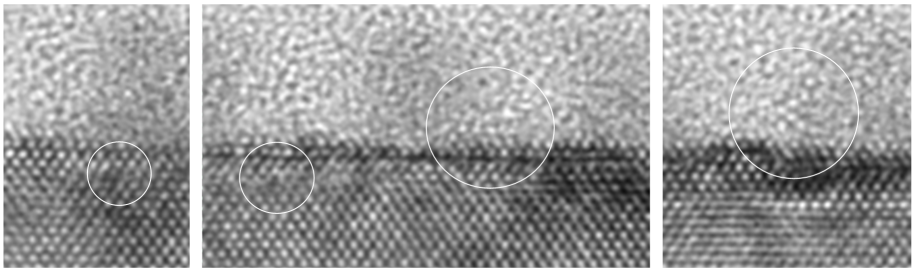

Fig. 3.7 Close-up view of the features near the boundary between crystalline and amorphized layers (300 W).

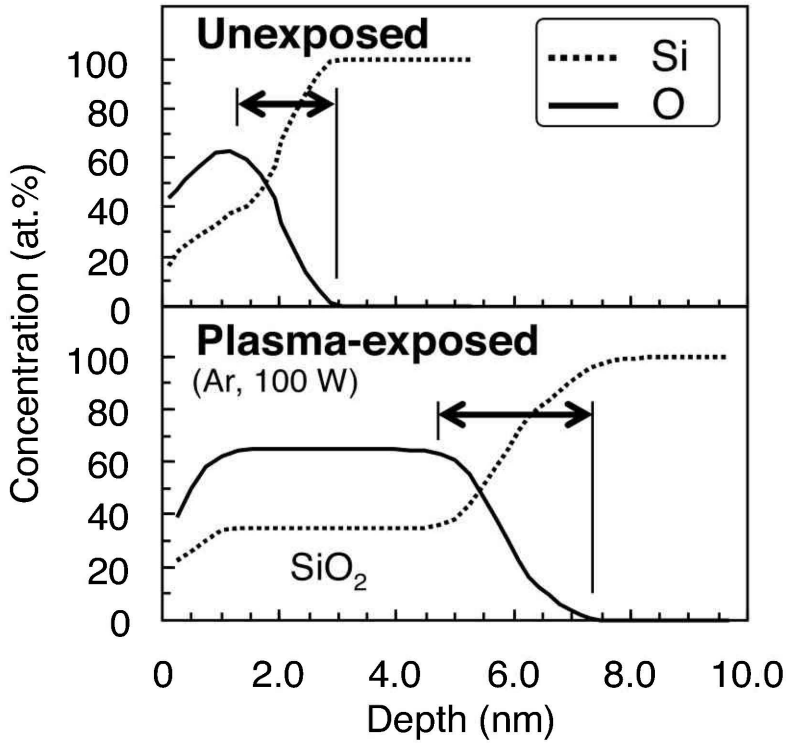

Fig. 3.8 Depth profile of the atomic concentration, obtained using RBS.

3.3.4. Optical model and layer thickness

From the above discussions, it has been found that the plasma-exposed samples possess partially oxidized layers (including roughness and segregated oxygen) and/or strain fields; and that a layer representing these must be included in the model. We choose not to include strains in the model, based on two reasons: (i) Based on reports on uniaxial stress [22], [23], the shift in optical constants induced from the strain fields (~ 10^{-2} eV) is expected to be negligible, compared to the effect of oxide incorporation. The shift from the stress is just comparable to the energy resolution of the measurements in this study (0.05 eV), while the oxide incorporation alters the dielectric function dramatically [23], as will be described in Eq. (3.4). (ii) The optical constants of strained silicon are not established and would be inappropriate for practical use.

The partially-oxidized layer was modeled as a mixture of Si and SiO_2 phases (whose dielectric functions are ε_{Si} and ε_{SiO_2}, respectively) by using Bruggeman's effective medium approximation (EMA) [15], [24]:

$$f_{Si}\frac{\varepsilon_{Si}-\varepsilon}{\varepsilon_{Si}+2\varepsilon}+(1-f_{Si})\frac{\varepsilon_{SiO_2}-\varepsilon}{\varepsilon_{SiO_2}+2\varepsilon}=0, \tag{3.4}$$

to derive the effective dielectric function (ε) of the layer, where f_{Si} is the volume fraction of Si. EMA is thought to be suitable for the layers discussed, as it models the layer as possessing inclusion of microstructures of the components, which the nanoscale crystalline protrusions/inclusions observed via HRTEM may correspond to. As such, assuming the Si phase to be crystalline (model B) was estimated to be the most suitable. Optical constants for each of the components were obtained from the compilation by Palik [25]. The model used in earlier literature [8], [10] (model A) and a model that assumes the Si phase to be

amorphous (model C) was also compared. Three additional models are considered for comparison (Fig. 3.9).

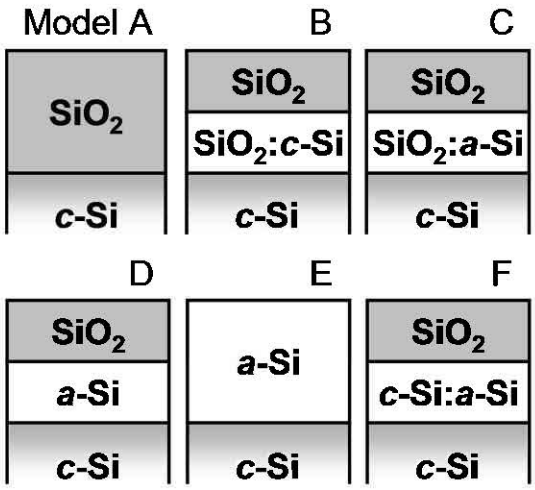

Fig. 3.9 Optical models compared in this study.

The unbiased estimator σ for each of the models are shown in Fig. 3.10. The increase of σ for model A indicates that the model is inappropriate especially with higher $\bar{E}_{\mathrm{i}}$. Models B and C exhibited lower σ, implying better fit. Table 3.2 shows the fitting results for the samples observed by using HRTEM. For 100 W, the total layer thickness ($d_{\mathrm{SL}} + d_{\mathrm{IL}}$) for models B and C equals the layer thickness as observed via HRTEM. For 300 W, the larger d_{IL} may be due to the oxygen incorporation in the crystalline region, causing the region to be included in the interface layer. The different trends for the $P_{\mathrm{bias}} = 400$ W ($\bar{E}_{\mathrm{i}} = 420$ eV) can be explained by its nanocrystalline dots/ripples. Thus, this sample is beyond the applicable scope of these models. The optimal model to describe this energy range would need a roughness layer (*e.g.*, EMA of ambient and SiO_2) [15].

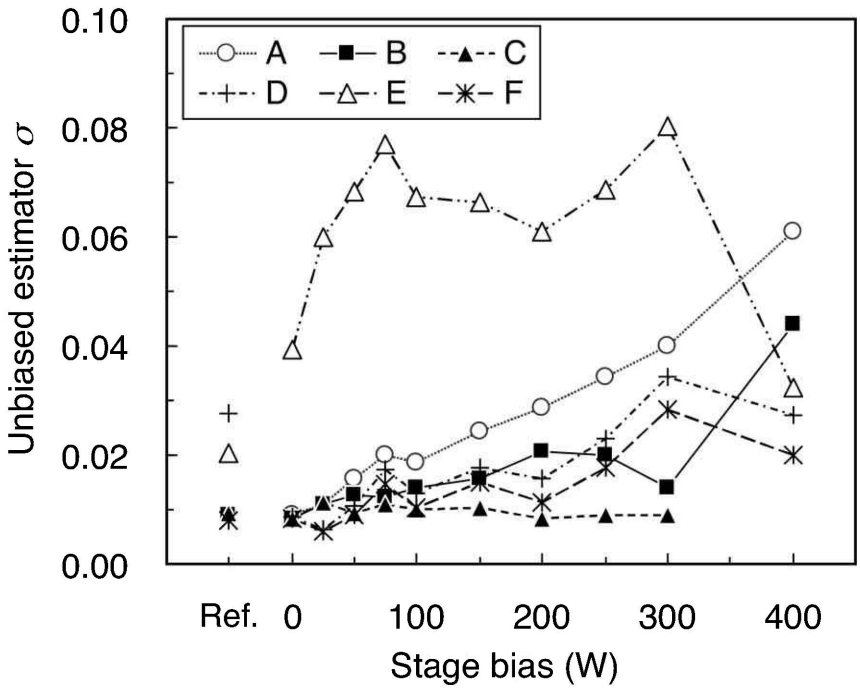

Fig. 3.10 Unbiased estimator σ for ellipsometry measurements. The spectra for 400 W sample could not be fitted with model D and was not plotted.

Table 3.2 Fitting results for two of the samples.

	$P_{\text{bias}} = 100$ W ($\bar{E}_{\text{i}} = 150$ eV)			$P_{\text{bias}} = 300$ W ($\bar{E}_{\text{i}} = 350$ eV)		
Model	d_{SL} (nm)	d_{IL} (nm)	f_{Si}	d_{SL} (nm)	d_{IL} (nm)	f_{Si}
A	5.1	-	-	6.3	-	-
B	3.4	1.2	29% *c*-Si	1.2	3.7	25% *c*-Si
C	3.2	1.5	69% *a*-Si	1.6	3.7	54% *a*-Si
D	4.3	0.9	-	5.1	1.6	-
E	5.2	-	-	7.8	-	-
F	4.3	5.6	20% *a*-Si	5.0	8.6	30% *a*-Si

It is of interest to note that earlier investigations on thermally-grown SiO_2/Si structure have addressed a transition layer containing nanometer-sized conical oxide "islands" or "hillocks" of *c*-Si [26], which can be modeled as a mixture of fused SiO_2 and *c*-Si [27], [28], which corresponds to model B in this work.

Based on these facts, model B was employed to investigate the $\bar{E}_i$-dependence of surface layer thickness (d_{SL}), interface layer thickness (d_{IL}), and their sum ($d_{SL} + d_{IL}$) (Fig. 3.11). There was no clear $\bar{E}_i$-dependence for f_{Si}. Its value was 23–32% except for the 400 W sample (39%). ($d_{SL} + d_{IL}$) saturated at approximately 5 nm. This is consistent with the widely observed Si recess thickness [8]. d_{SL} peaked at around 50 eV and showed a turnover. Smaller d_{SL} beyond this point may be attributed to surface sputtering; as the sputtering thresholds for Ar impacting Si and SiO_2 are known to be 45–50 eV [13]. At larger $\bar{E}_i$, the interface layer thickness (d_{IL}) increased to become dominant in the surface structure. This coincides with the increase in layers 2 and 3 in the simulation. This fact serves as an additional evidence of the importance of including an interface layer.

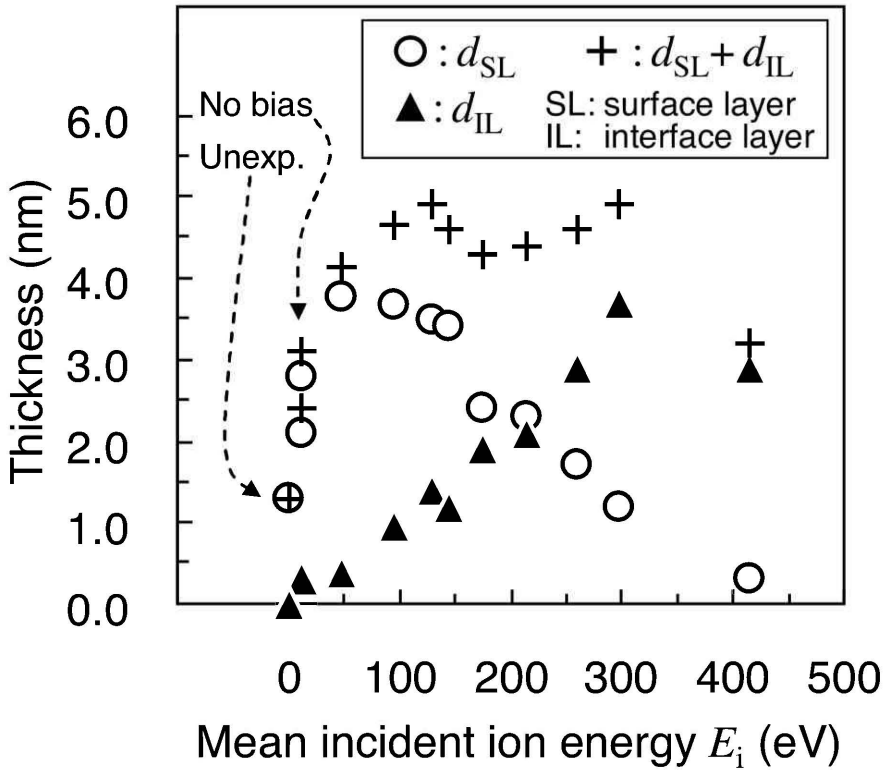

Fig. 3.11 Thickness fitting results using model B (SL: SiO_2, IL: SiO_2 & *c*-Si).

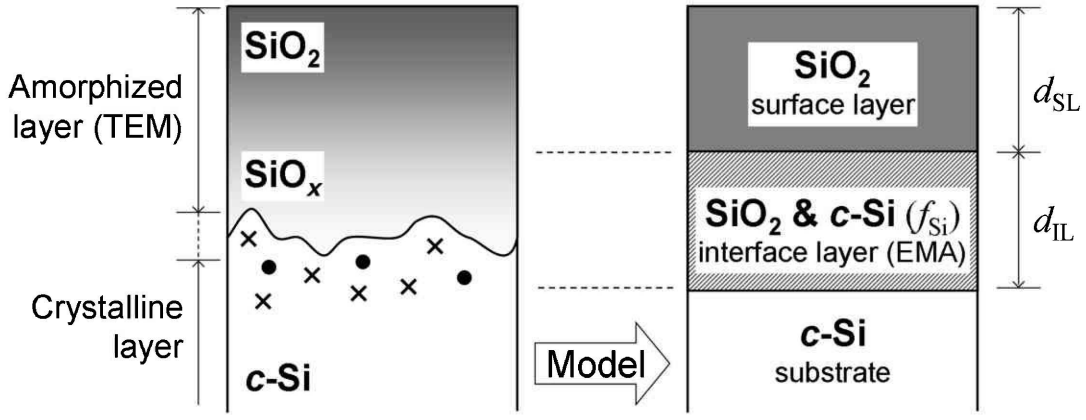

Fig. 3.12 Schematic illustration showing the physical structure as deduced from MD, TEM, and RBS. This structure is optically modeled as shown on the right.
●: segregated O atoms, ×: interstitial Si atoms.

3.4. Conclusion

The formation mechanisms, structure, composition and optical characteristics of damaged silicon wafers were studied comprehensively. MD simulation showed the formation of interstitials, interface roughness and oxygen inclusions induced by Ar^+ ion bombardment. These events were also observed in the plasma-exposed wafer surface, both directly in the micrographs and as the gradual transition of oxygen concentration in the RBS profile. An optical model that addresses these effects was proposed, consisted by the SiO_2 surface layer, the interface layer as EMA of SiO_2 and *c*-Si, and the *c*-Si substrate. Optical constants are to be fixed and fitted using the three unknown parameters: d_{SL}, d_{IL}, and f_{Si}. This small set of parameters is desirable because uncertainty that arise from the fitting procedure (such as overfitting) can be avoided. The interrelation between the physical structure and the analyses is shown in Fig. 3.12. The SE interface layer addresses the interface roughness and defects in the substrate. Using the values of d_{SL} and d_{IL} obtained using the optimal model, depth of the silicon recess can be estimated [6], [9]. We believe that this accurate and practical model described in this work would be effective in addressing physical damage in both laboratories and for in-line monitoring in mass production lines.

3.5. References

[1] C. Y. Chang and S. M. Sze, *ULSI Technology*. New York: McGraw-Hill, 1996.

[2] M. Fukasawa, Y. Nakakubo, A. Matsuda, Y. Takao, K. Eriguchi, K. Ono, M. Minami, F. Uesawa, and T. Tatsumi, "Structural and electrical characterization of HBr/O_2 plasma damage to Si substrate," *J. Vac. Sci. Technol. A*, vol. 29, 041301, Jun. 2011.

[3] U. F. Gianola, "Damage to Silicon Produced by Bombardment with Helium Ions," *J. Appl. Phys.*, vol. 28, pp. 868–873, Aug. 1957.

[4] R. Charavel and J.-P. Raskin, "Etch Rate Modification of SiO_2 by Ion Damage," *Electrochem. Solid-State Lett.*, vol. 9, no. 7, pp. G245–G247, Jul. 2006.

[5] Y. Nakakubo, A. Matsuda, M. Fukasawa, Y. Takao, T. Tatsumi, K. Eriguchi, and K. Ono, "Optical and Electrical Characterization of Hydrogen-Plasma-Damaged Silicon Surface Structures and Its Impact on In-line Monitoring," *Jpn. J. Appl. Phys.*, vol. 49, 08JD02, Aug. 2010.

[6] K. Eriguchi, A. Matsuda, Y. Nakakubo, M. Kamei, H. Ohta, and K. Ono, "Effects of Plasma-Induced Si Recess Structure on n-MOSFET Performance Degradation," *IEEE Electron Device Lett.*, vol. 30, no. 7, pp. 712–714, Jul. 2009.

[7] S. A. Vitale and B. A. Smith, "Reduction of silicon recess caused by plasma oxidation during high-density plasma polysilicon gate etching," *J. Vac. Sci. Technol. B*, vol. 21, no. 5, pp. 2205–2211, Sep. 2003.

[8] T. Ohchi, S. Kobayashi, M. Fukasawa, K. Kugimiya, T. Kinoshita, T. Takizawa, S. Hamaguchi, Y. Kamide, and T. Tatsumi, "Reducing Damage to Si Substrates during Gate Etching Processes," *Jpn. J. Appl. Phys.*, vol. 47, pp. 5324–5326, Jul. 2008.

[9] K. Eriguchi, Y. Nakakubo, A. Matsuda, M. Kamei, H. Ohta, H. Nakagawa, S. Hayashi, S. Noda, K. Ishikawa, M. Yoshimaru, and K. Ono, "A New Framework

for Performance Prediction of Advanced MOSFETs with Plasma-Induced Recess Structure and Latent Defect Site," in *IEDM Tech. Dig.*, 2008, pp. 436–446.

[10] Y. Nakamura, T. Tatsumi, S. Kobayashi, K. Kugimiya, T. Harano, A. Ando, T. Kawase, S. Hamaguchi, and S. Iseda, "Control of atomic layer degradation on Si substrate," *J. Vac. Sci. Technol. A*, vol. 25, pp. 1062–1067, Jul. 2007.

[11] F. H. Stillinger and T. A. Weber, "Computer simulation of local order in condensed phases of silicon," *Phys. Rev. B*, vol. 31, no. 8, pp. 5262–5271, Apr. 1985.

[12] D. B. Graves and D. Humbird, "Surface chemistry associated with plasma etching processes," *Appl. Surf. Sci.*, vol. 192, no. 1–4, pp. 72–87, May 2002.

[13] H. Ohta and S. Hamaguchi, "Molecular dynamics simulation of silicon and silicon dioxide etching by energetic halogen beams," *J. Vac. Sci. Technol. A*, vol. 19, no. 5, pp. 2373–2381, Oct. 2001.

[14] H. Ohta and S. Hamaguchi, "Classical interatomic potentials for Si–O–F and Si–O–Cl systems," *J. Chem. Phys.*, vol. 115, no. 14, pp. 6679–6690, Oct. 2001.

[15] 藤原裕之, 分光エリプソメトリー, 第 2 版, 東京: 丸善, 2011.

[16] N. Yabumoto, M. Oshima, O. Michikami, and S. Yoshii, "Surface Damage on Si Substrates Caused by Reactive Sputter Etching," *Jpn. J. Appl. Phys.*, vol. 20, no. 5, pp. 893–900, May 1981.

[17] Z. Yu, D. A. Muller, and J. Silcox, "Study of strain fields at a-Si/c-Si interface," *J. Appl. Phys.*, vol. 95, no. 7, pp. 3362–3371, Apr. 2004.

[18] P. J. Schultz, E. Tandberg, K. G. Lynn, B. Nielsen, T. E. Jackman, M. W. Denhoff, and G. C. Aers, "Defects and Impurities at the Si/Si(100) Interface Studied with Monoenergetic Positrons," *Phys. Rev. Lett.*, vol. 61, no. 2, pp. 187–190, Jul. 1988.

[19] R. Gago, L. Vázquez, R. Cuerno, M. Varela, C. Ballesteros, and J. M. Albella, "Production of ordered silicon nanocrystals by low-energy ion sputtering," *Appl. Phys. Lett.*, vol. 78, no. 21, pp. 3316–3318, May 2001.

[20] T. K. Chini, F. Okuyama, M. Tanemura, and K. Nordlund, "Structural investiga-

tion of keV Ar-ion-induced surface ripples in Si by cross-sectional transmission electron microscopy," *Phys. Rev. B*, vol. 67, no. 20, 205403, May 2003.

[21] B. Ziberi, F. Frost, T. Höche, and B. Rauschenbach, "Ripple pattern formation on silicon surfaces by low-energy ion-beam erosion: Experiment and theory," *Phys. Rev. B*, vol. 72, no. 23, 235310, Dec. 2005.

[22] P. Etchegoin, J. Kircher, and M. Cardona, "Elasto-optical constants of Si," *Phys. Rev. B*, vol. 47, no. 16, pp. 10292–10303, Apr. 1993.

[23] N. V. Nguyen, D. Chandler-Horowitz, P. M. Amirtharaj, and J. G. Pellegrino, "Spectroscopic ellipsometry determination of the properties of the thin underlying strained Si layer and the roughness at SiO_2/Si interface," *Appl. Phys. Lett.*, vol. 64, no. 20, pp. 2688–2690, May 1994.

[24] D. E. Aspnes, "Optical properties of thin films," *Thin Solid Films*, vol. 89, no. 3, pp. 249–262, Mar. 1982.

[25] E. D. Palik, Ed., *Handbook of Optical Constants of Solids*, vol. 1. Academic Press, 1997.

[26] M. L. Green, E. P. Gusev, R. Degraeve, and E. L. Garfunkel, "Ultrathin (< 4 nm) SiO_2 and Si–O–N gate dielectric layers for silicon microelectronics: Understanding the processing, structure, and physical and electrical limits," *J. Appl. Phys.*, vol. 90, no. 5, pp. 2057–2121, Sep. 2001.

[27] G. E. Jellison, "Examination of thin SiO_2 films on Si using spectroscopic polarization modulation ellipsometry," *J. Appl. Phys.*, vol. 69, no. 11, pp. 7627–7634, Jun. 1991.

[28] V. A. Yakovlev and E. A. Irene, "An Interface Enhanced Spectroscopic Ellipsometry Technique: Application to Si-SiO_2," *J. Electrochem. Soc.*, vol. 139, no. 5, pp. 1450–1455, May 1992.

4. Depth Profiling of Damaged Layers

4.1. Introduction

The structure and composition of plasma-damaged Si is typically not uniform depth-wise. As illustrated in Fig. 4.1(a), the density of the defects has a certain profile. The density is typically high near the surface and decreases with depth [Fig. 4.1(d)]. (See also chapter 1.)

It was recently reported that there is a trade-off relationship between the recess depth (d_{R}) and the residual defect density (n_{dam}) [1]. For instance, a wet-etch process to remove a large amount of the damaged layer would reduce n_{dam} and drain current degradation, but results in a deeper recess—and vice versa (Fig. 4.2). As the trade-off relationship is governed by the profile of the defects and the wet-etch process conditions, it is crucial to understand, analyze, and control defect profiles, in order to minimize their effects on device performance.

To the author's knowledge, one group—Wada *et al.* [2]—has previously studied defect profiles using PRS, wherein they chemically etched the damaged layer with diluted hydrofluoric acid (DHF) and boiled HNO_3, and measured the etched depth with a surface profiler. They found a dependence of the defect profile on plasma RF power, but did not focus on the effects of mass, atom

radius, and projected range of the ions, which is also an important factor that governs physical damage and its depth profile. This chapter aims to address this issue by exposing Si wafers to plasmas with two different gases: He and Ar. We developed an improved wet-etching and depth-monitoring procedure that involves: processing the plasma-damaged substrates with DHF and H_2O_2, monitoring the changes in layer thicknesses and removal depths by SE, and analyzing the changes in the surface potential by PRS.

The experiment flowchart is illustrated in Fig. 4.3. By wet-etching the samples for various durations (wet-etch time t_w), the removed depth d_w was varied. The wet-etch rate of the damaged layer and changes in the surface potential caused by the trapped charges were analyzed. The defect profiles of He- and Ar-plasma-damaged Si are comparatively discussed.

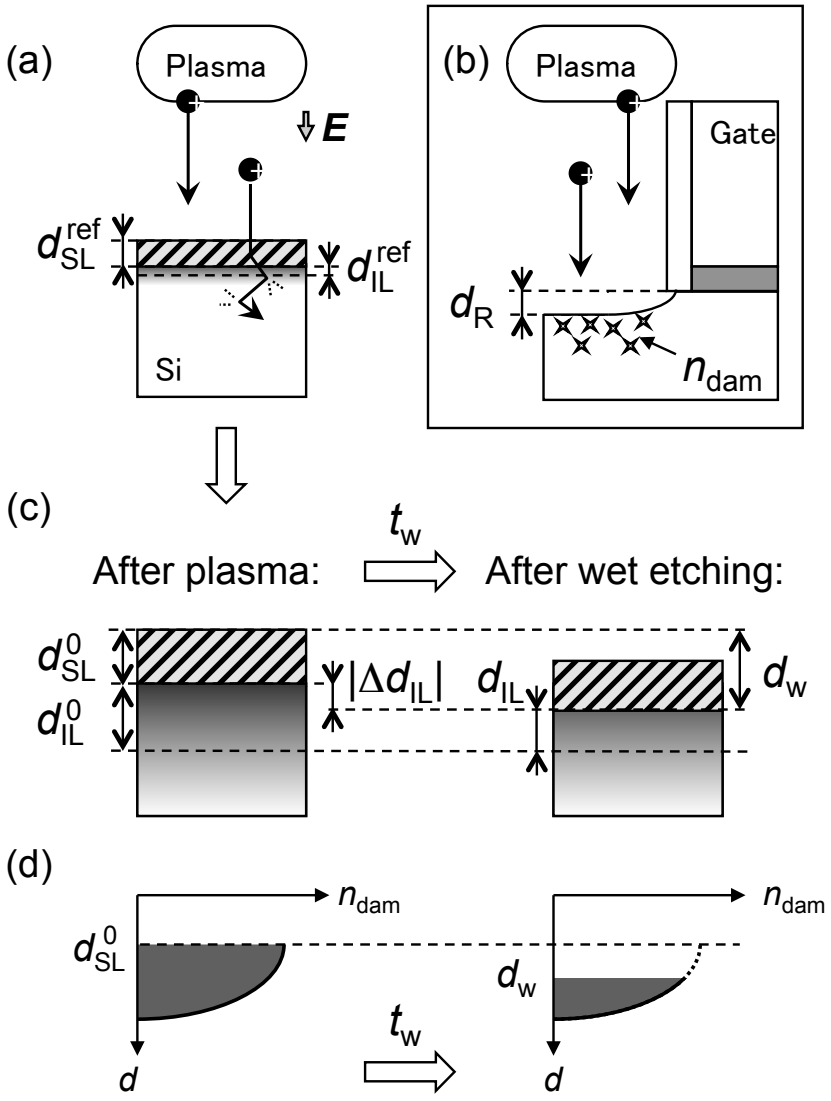

Fig. 4.1 (a) Schematics of the physical damage, caused by energetic ions accelerated in the plasma sheath bombarding the Si surface. Stripes indicate SiO_2 surface layer. Gradation indicates the structural transition layer from SiO_2 to the Si substrate. Thicknesses of the layers before plasma exposure are shown in terms of ellipsometric measurements. (b) Implications in MOSFETs, in terms of recess depth (d_R) and latent defect density (n_{dam}). (c) Wet-etch removal of the damaged layer. Gradations indicate the defect density profiles. The definition of the removed depth d_w is illustrated. (d) Schematic depth profiles of the defect density and strip-off by wet etching. Filled areas indicate charge-trapping defects.

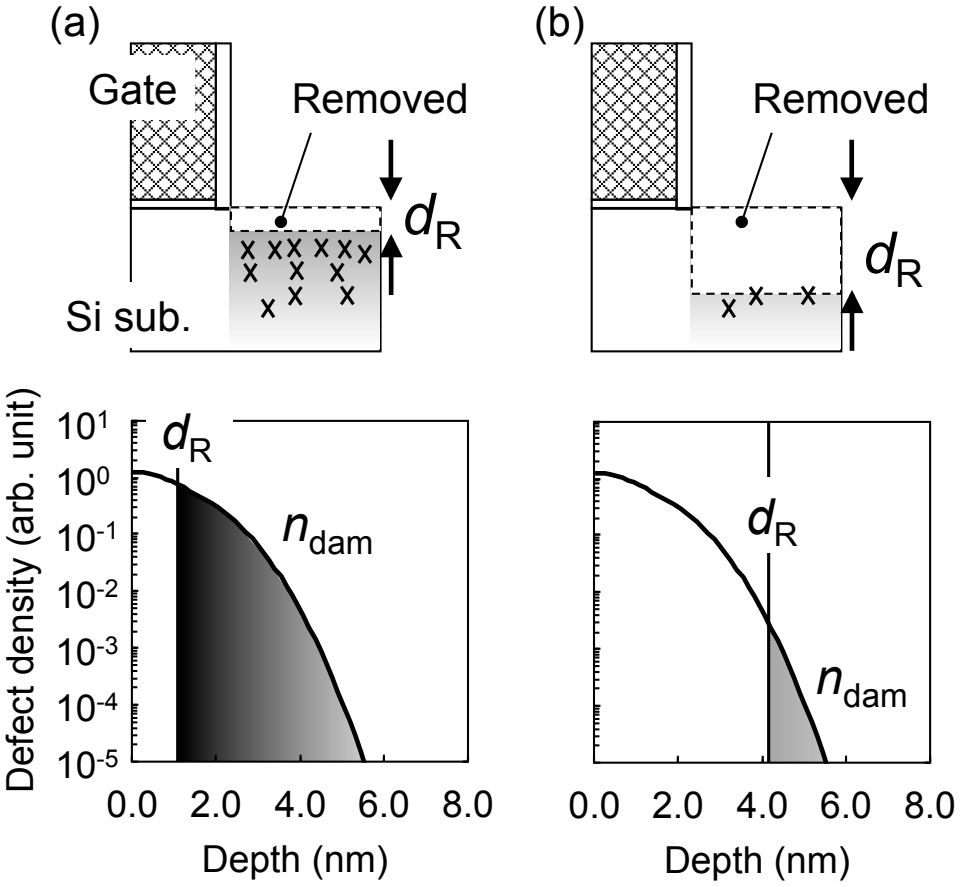

Fig. 4.2 MOSFET after post-etch wet treatment and its defect density profile [1].
(a) Strip-off criteria to minimize recess.
(b) Strip-off criteria to minimize residual damage.

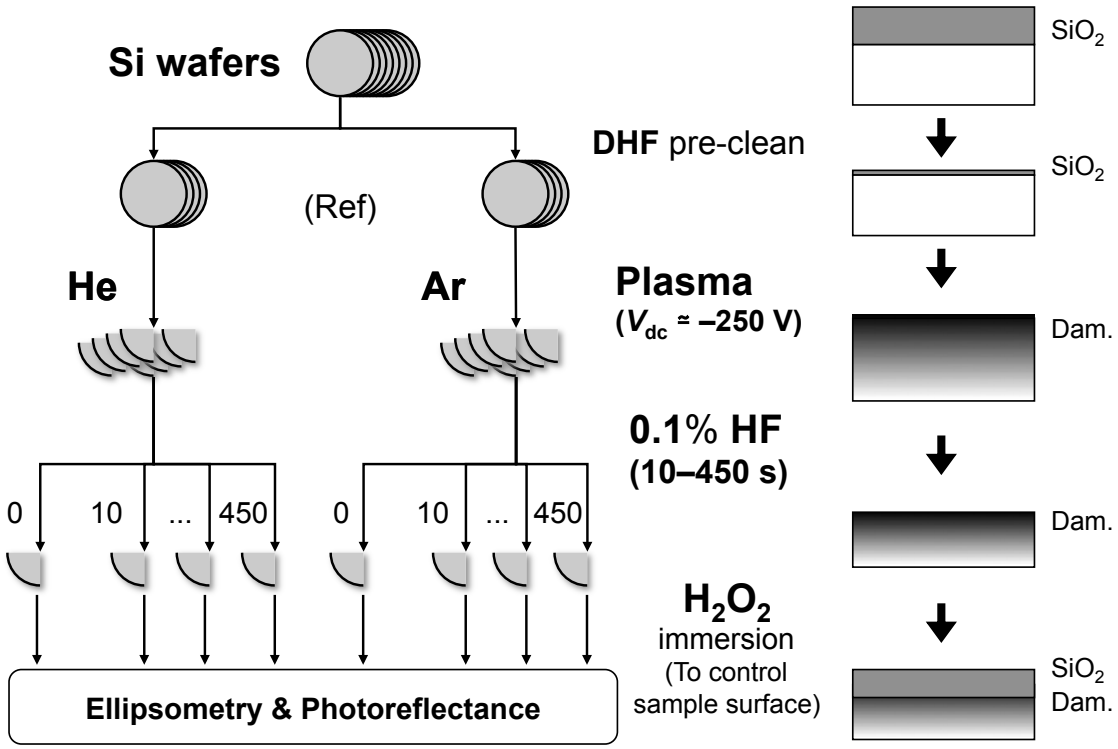

Fig. 4.3 Schematic flowchart of the experiment and the expected surfaces at each step.

4.2. Experimental procedure

4.2.1. Plasma exposure and wet etching

A CCP reactor illustrated in Fig. 4.4 was used. The chamber was made of stainless steel, and its dimensions were 250 mm in diameter and 300 mm in height. A four-inch wafer stage was located at the bottom side of the chamber. 13.56 MHz RF power supply was connected to the wafer stage via a matching box. The voltage of the wafer stage was monitored with a probe and an oscilloscope. The chamber was vacuum-pumped with Oerlikon Leybold Vacuum TURBOVAC TMP 361 turbo molecular pump (TMP) and Alcatel M2010SD rotary pump (RP). Chamber pressure was monitored by Anelva crystal ion gauge and capacitance gauge.

N-type Si (100) wafers with resistivity of 0.02 Ωcm were used. The wafers were pre-cleaned by diluted hydrofluoric acid (DHF) for 60 s. The pre-cleaned sample would be referred to hereafter as the "reference sample". The wafers were placed on the stage of a CCP reactor. One set of the wafers was exposed to He plasma, and another to Ar plasma. Pressure was 2.7 Pa. The plasma was driven by a 13.56 MHz power supply, whose power was controlled in the range from 8 to 9 W to maintain the DC bias voltage V_{dc} (monitored with the oscilloscope) to be approximately −250 V. The duration of each process was 30 s. After the plasma exposure, the damaged layer was wet-etched in 0.1 wt% DHF for a certain wet-etch time of t_w (Fig. 4.5):

$$SiO_2 + 6\,HF(aq) \rightarrow H_2SiF_6 + 2\,H_2O\,,$$

rinsed in pure water, and immersed in hydrogen peroxide (H_2O_2) solution to control the surface [Fig. 4.1 (c),(d)]. By varying t_w, in the range 10–450 s, various thicknesses of the damaged layer were removed.

Thickness of the damaged layer was monitored by SE, using the optical model established in the previous chapter. Using the determined thicknesses, the removal depth d_w as measured from the initial surface (before wet etching; $t_w = 0$) is defined as

$$d_w(t_w) = d_{SL}^0 + |\Delta d_{IL}(t_w)|\,, \tag{4.1}$$

where d_A^0 (A: SL or IL) indicates d_{SL} at $t_w = 0$, and $\Delta d_{IL} = d_{IL} - d_{IL}^0 < 0$. See also Fig. 4.1(c).

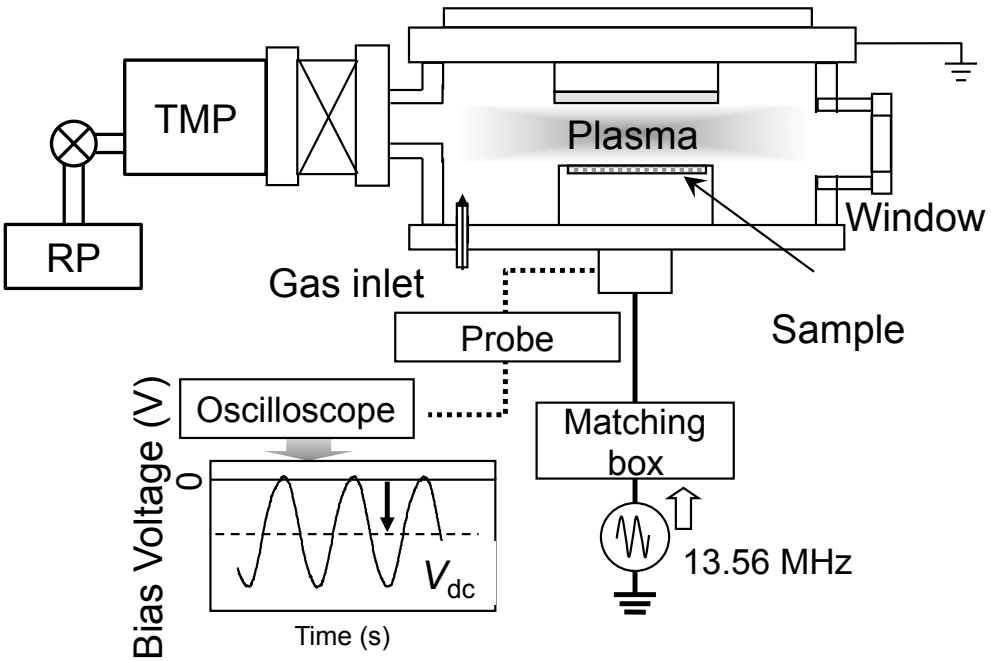

Fig. 4.4 CCP chamber used in this study.

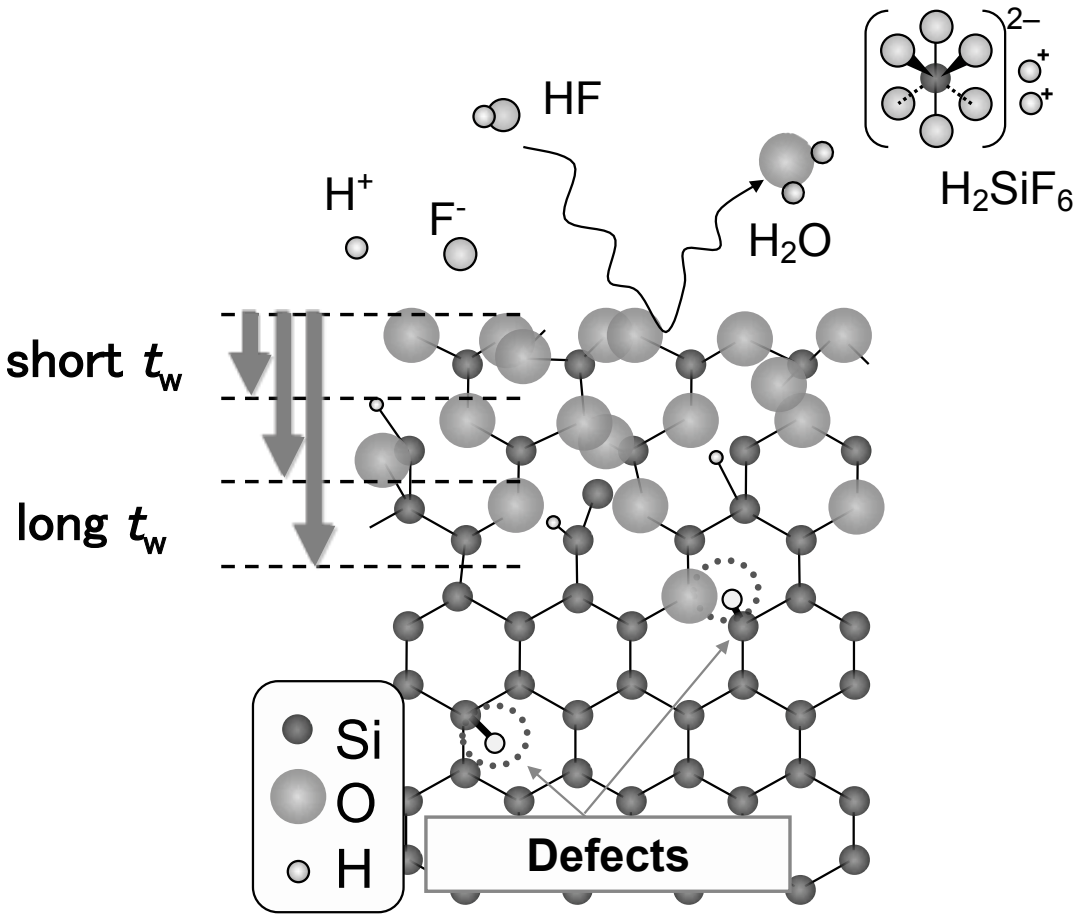

Fig. 4.5 Wet etching of the damaged layer by hydrofluoric acid.

4.2.2. Photoreflectance spectroscopy

PRS measurement was performed using the setup illustrated in Fig. 4.6. A xenon light source from Jobin Yvon UVISEL ellipsometer system was used for the probe beam. A laser unit housing a diode-pumped solid-state laser (Laser-Export DTL-313) was used for the modulation beam. Both beams were guided with single-core optical fibers (core diameter: 800 μm). The modulation beam was chopped at 500 Hz by a mechanical chopper inside the laser housing, and Stanford Research SR830 lock-in amplifier was used to extract the signal.

The PR spectrum is expressed as the ratio of a small change in reflectance caused by the modulation beam (ΔR, typically $\sim 10^{-5} \times R$ in our system) to the reflectance (R). As explained in chapter 2, a PR spectrum can be expressed by a third-derivative functional form (TDFF) as

$$\frac{\Delta R}{R} = \Re\left[C e^{i\theta}\left(E - E_g + i\Gamma\right)^{-n}\right], \tag{4.2}$$

where C is the amplitude factor, θ is the phase factor, E is the photon energy of the probe beam, E_g is the critical point energy, and Γ is the broadening parameter. The parameter n is related to the dimensionality of the interband critical point [3]. The signal intensity of a PR spectrum ($|\Delta R/R|$) is defined as the absolute value of an extremum of a valley at around 3.4 eV (equivalent to the wavelength range analyzed in this study). The optical property of Si has a complex structure at around 3.4 eV. Two types of optical transitions are possible in this range, namely, the E_1 transition along the Λ direction near the L point of the Brillouin zone ($n = 3$) and the E_0' transition at the Γ point ($n = 5/2$). We will cover this matter more closely in chapter 5. For the purpose of this chapter, $n = 3$ is assumed.

In the experiment, the obtained spectra were fitted to Eq. (4.2), and the four TDFF parameters (C, θ, E_g, and Γ) were determined. Of these parameters, the amplitude factor (C) is related to the surface potential (V_s) as [4], [5]:

$$C = P_1 \ln\left(P_2 I_p + 1\right), \tag{4.3}$$

$$P_1 = \frac{c_1}{\mu_{\|}} \frac{\eta k_B T}{e}, \tag{4.4}$$

$$P_2 = c_2 \frac{e\gamma(1-R)}{A^* T^2 h\nu} \exp\left(\frac{eV_s}{k_B T}\right), \tag{4.5}$$

where I_p is the modulation beam intensity, c_1 and c_2 are constants, $\mu_{\|}$ is the interband reduced mass evaluated in the direction of the electric field, η is the ideality factor [6], k_B is the Boltzmann constant, T is the temperature on the sample surface, e is the elementary charge, γ is the quantum efficiency of Si, A^* is the modified Richardson constant [7], and $h\nu$ is the photon energy of the modulation beam. It has been reported that the signal intensity of the PR spectra of plasma-exposed Si surfaces becomes lower than that of the unexposed (control) Si surface [2], [8]–[10]. This is attributed to the formation of trap sites [10] and/or recombination centers [2] for photogenerated carriers, which changes the modulating photovoltage generated by irradiation of the modulation beam (V_m), as well as V_s (Fig. 4.7). The change in V_s induced by plasma exposure (ΔV_s) was calculated by the following procedure: The parameters P_1 and P_2 were extracted by fitting the laser power (I_p) dependence of C to Eq. (4.3). Then, ΔV_s was calculated as

$$\Delta V_s = \frac{k_B T}{e} \ln\left(\frac{P_2^{\mathrm{dam}}}{P_2^{\mathrm{ctrl}}}\right). \tag{4.6}$$

Under assumptions that the change in V_s is induced by the formation of charge-trapping defects (Fig. 4.8) and that the depth profile of the defect sites is uniform, the areal density of trapped charges (N_{dam}) can be calculated by solving Poisson's equation as

$$N_{dam} = -\frac{\varepsilon_{Si}\varepsilon_0}{e}\frac{\Delta V_s}{d_c}, \tag{4.7}$$

where ε_{Si} is the dielectric constant of Si, ε_0 is the vacuum permittivity, and d_c is the assumed depth of the charge centroid from the surface.

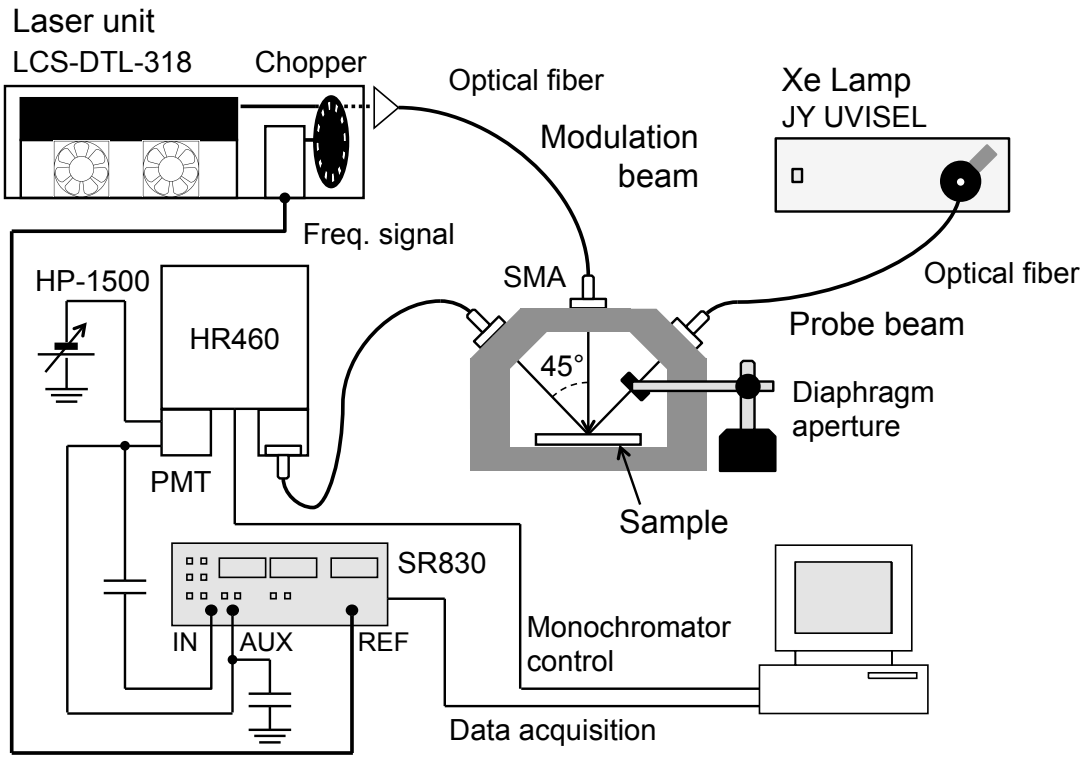

Fig. 4.6 Apparatus for PR measurement.

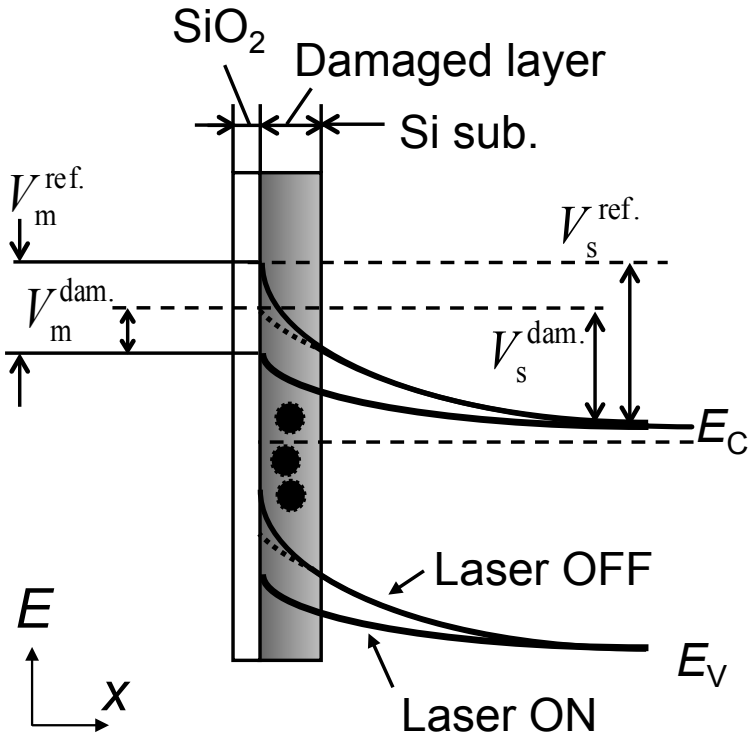

Fig. 4.7 Surface potential of a plasma-damaged Si surface.

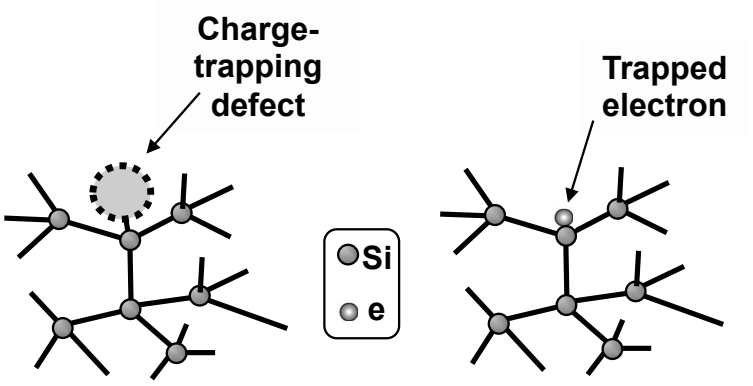

Fig. 4.8 Charge-trapping defect.

4.3. Results

Fig. 4.9 shows the layer thicknesses measured by SE as a function of wet-etch time (t_w). After plasma exposure ($t_w = 0$ s), both d_{SL} and d_{IL} increased from those of the reference sample. After wet etching ($t_w > 0$ s), both d_{SL} and d_{IL} decreased from those at $t_w = 0$ s (with the exception of $t_w = 10$ s for Ar). d_{IL} showed a monotonic decrease with t_w, indicating removal of the layer by wet etching, but d_{SL} fluctuated with respect to t_w.

Photoreflectance spectra for some of the samples are shown in Fig. 4.10. Signal intensities for all samples are shown in Fig. 4.11 as a function of t_w. After plasma exposure, $|\Delta R/R|$ decreased significantly from that of the reference sample. After wet etching, $|\Delta R/R|$ increased with t_w. All of these characteristics were observed for both gases. The trajectory of $|\Delta R/R|$ is shown in Fig. 4.12 as a function of d_{IL}. As the interface layer was removed, the PR signal intensity increased. We were not able to completely eliminate the interface layer (due to the diminishing etch rate, we would have required very long t_w), but we can see the trend for Ar-plasma-damaged samples approaches the reference sample as the interface layer is removed. On the other hand, the trend shows that even if we removed all of the interface layer, the sample would have a lower signal intensity than the reference sample. This matter will be discussed in

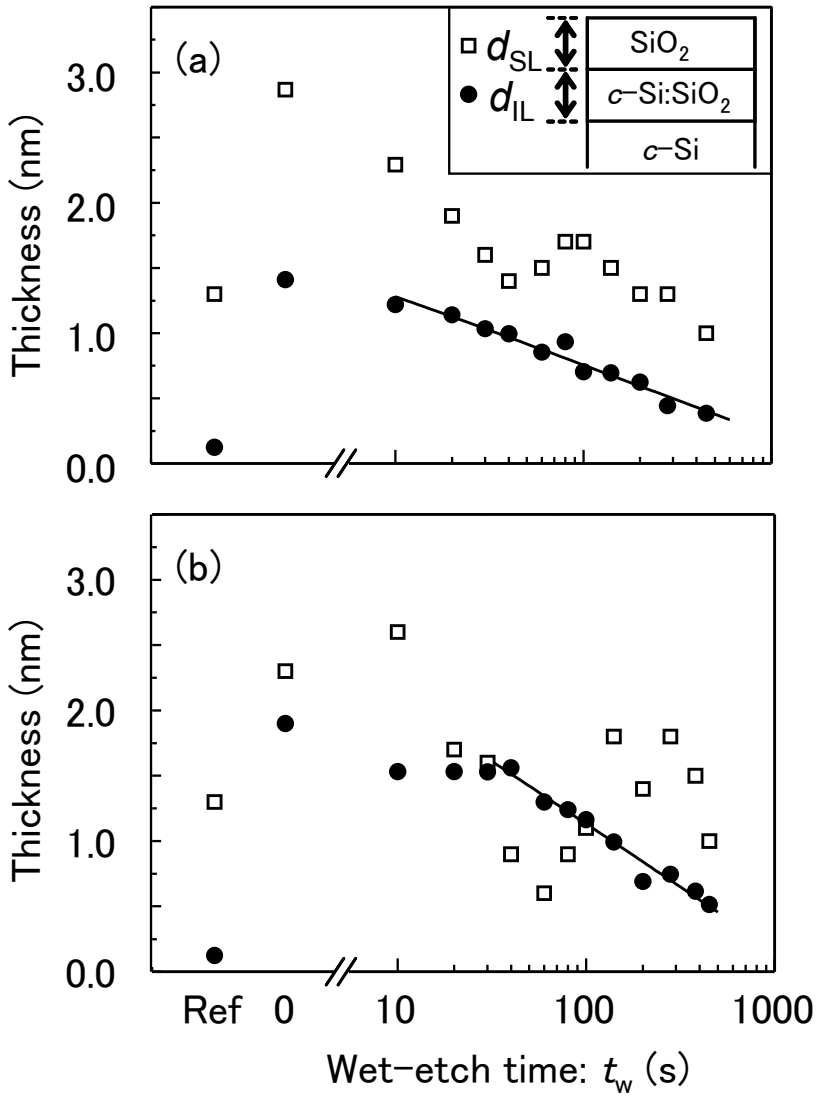

Fig. 4.9 Layer thicknesses as determined by spectroscopic ellipsometry. (a) He plasma, (b) Ar plasma. The optical model is shown in the inset. Lines show the best-fit logarithmic functions as expressed by Eq. (4.8). "Ref" indicates the reference sample prior to plasma exposure.

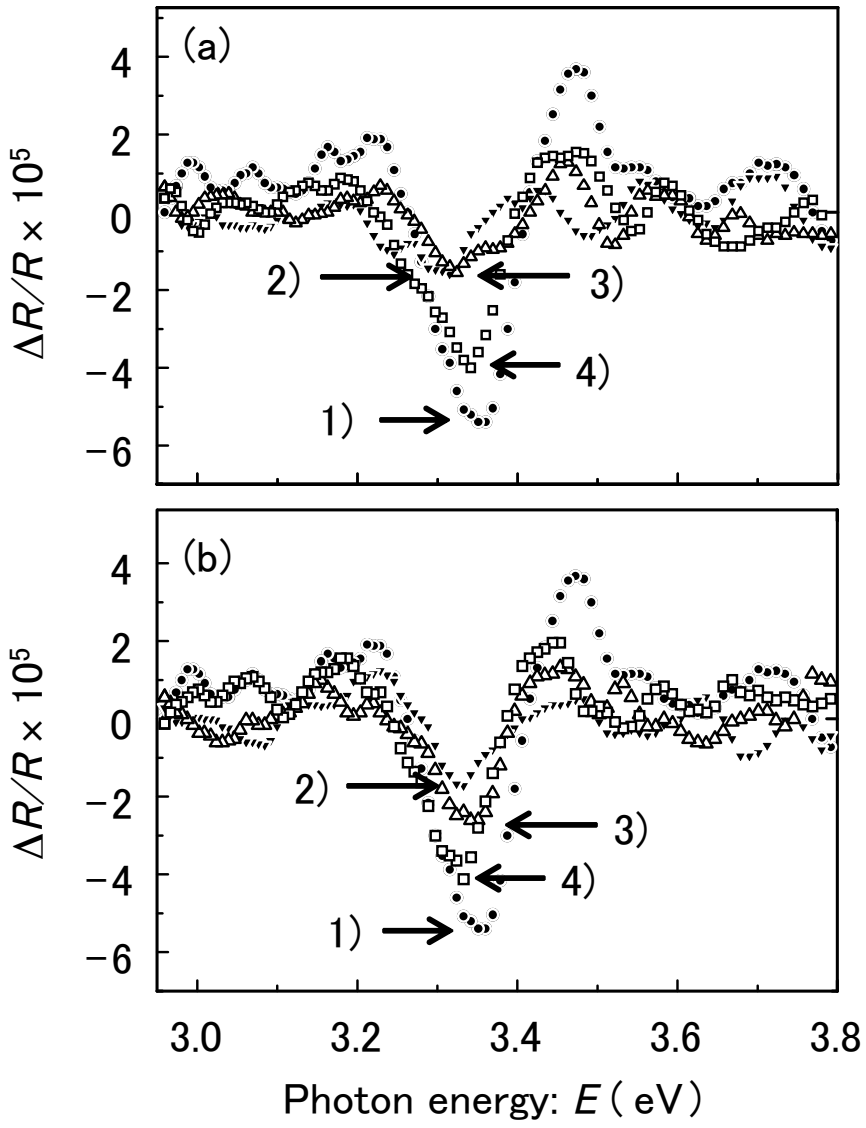

Fig. 4.10 Photoreflectance spectra.

1) Reference,

2) After plasma exposure and before wet etching ($t_w = 0$ s),

3) $t_w = 100$ s,

4) $t_w = 450$ s.

(a) He plasma, (b) Ar plasma.

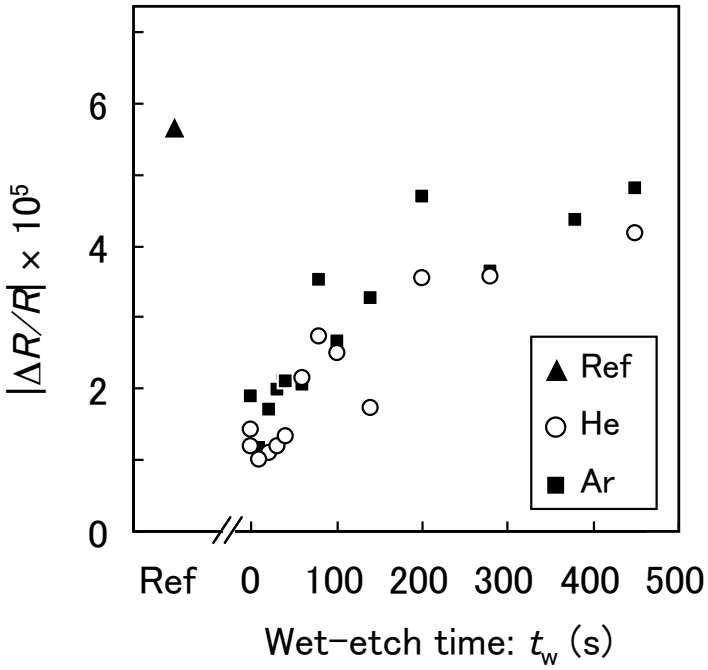

Fig. 4.11 Photoreflectance signal intensity as a function of wet-etch time t_w.

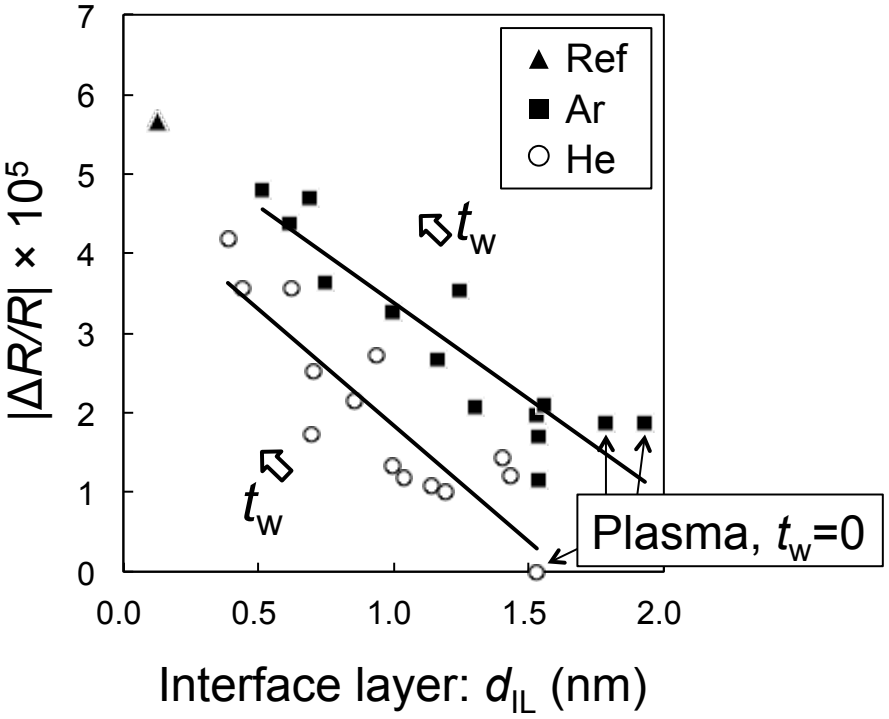

Fig. 4.12 Trajectory of photoreflectance signal intensity as a function of d_{IL}.

4.4. Discussion

4.4.1. Wet-etch rate and oxygen concentration profile

It has been reported that the IL of plasma-damaged Si can be considered as a nonstoichiometric silicon oxide, SiO_x ($x < 2$) [11]. Meanwhile, Pan *et al.* have prepared films of SiO_x by plasma-enhanced chemical vapor deposition (PECVD) and studied their etch rates to a HF solution [12]. For films of similar density, the etch rates of SiO_x films are lower than those of stoichiometric SiO_2 films, due to the presence of ≡Si–Si≡ bonds [13]. We hypothesized that the etch rates of nonstoichiometric SiO_x in plasma-damaged samples are lower in the same manner. From SE results in Fig. 4.9, we see that the t_w dependence of d_{IL} could be approximated by a logarithmic function,

$$d_{IL} = -a \ln(t_w + 1) + b\,, \tag{4.8}$$

where $a = 0.24$ and $b = 1.8$ for He, and $a = 0.42$ and $b = 3.1$ for Ar (unit: nm) give us the best-fit lines shown in the figure. By differentiating Eq. (4.8) with respect to t_w and using Eqs. (4.1) and (4.8), the wet-etch rate of IL can be expressed as a function that decays exponentially with removed depth (d_w) as

$$-\frac{\mathrm{d}d_{IL}}{\mathrm{d}t_w} = c \exp\left(-\frac{d_w}{a}\right), \tag{4.9}$$

where c is a constant expressed as

$$c = a \exp\left(\frac{d_{SL}^0 + d_{IL}^0 - b}{a}\right). \tag{4.10}$$

In analogy with PECVD films, it is natural to believe that the wet-etch rate indicates the difference in the ratio of the number of Si–O bonds to Si–Si bonds. Therefore, the fact that the rate could be expressed by an exponential form with

respect to d_w may indicate that the number of Si–O bonds in plasma-damaged layers also decreases exponentially with respect to the depth from the surface. A similar characteristic has been observed earlier in oxygen concentration profiles in Ar-plasma-damaged Si, in a study using secondary ion mass spectrometry [14].

4.4.2. Comparison of defect distributions

In Fig. 4.12, it is clear that for Ar-plasma-damaged samples, the PR signal intensity approaches that of the reference sample as the interface layer is removed. On the other hand, the trend for He-plasma-damaged samples indicates that there would be a notable amount of defects remaining even after all of the interface layer was removed. This implies that the defects generated by the He plasma were more distributed, deeper beyond the layers characterized as IL by SE (Fig. 4.13). This can be explained by the difference in mass of the ion species. He^+ ions, being lighter, has a deeper "projected range" and can penetrate deeper into the substrate [14], [15]. Similar effects have been reported for H_2-plasma-damaged Si. Fukasawa *et al.* [16] and Ito *et al.* [17] analyzed the profiles of atomic concentrations and dislocated Si by high-resolution Rutherford backscattering spectroscopy. Dislocated Si atoms were distributed deeper for H_2-plasma-damaged Si compared to Ar. These results imply that the damage caused by lighter ions (such as He^+ and H^+) could cause difficult problems, as they have deeper defect distributions. Post-plasma-etch treatments such as annealing could reduce the defect density, which is a subject for a future study. Plasma etching processes and post-etch treatments must be carefully designed to minimize the effects of physical damage on device performance.

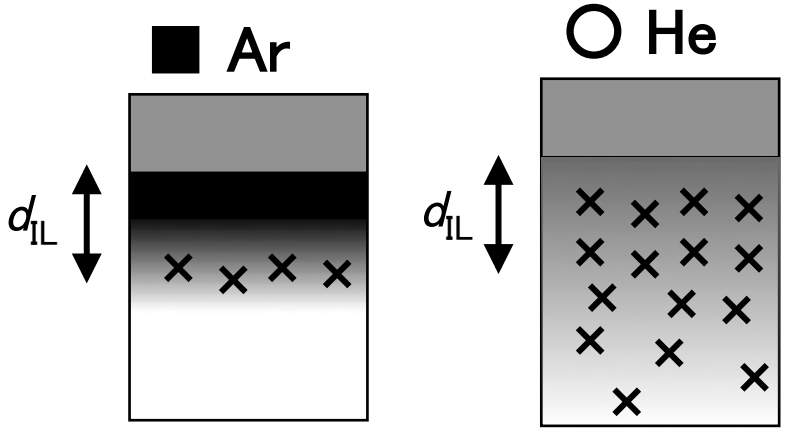

Fig. 4.13 Schematic illustration comparing the defect distribution generated by the two plasmas.

4.5. Conclusion

Depth profiling of He- and Ar-plasma-damaged Si substrates was performed by wet-etching the damaged layer using DHF. By using SE with an optimized optical model, we were able to address the exponential decay of the IL wet-etch rates with respect to depth. The rate could be indicative of the number of Si–O bonds. Photoreflectance signal intensity decreased with plasma exposure, indicating formation of charge-trapping defects and/or recombination centers. With wet etching, the signal intensity recovered with longer wet-etch times, indicating removal of the defects. PRS identified one of the key characteristics in the depth profiles between He and Ar: the defects caused by He plasma is distributed deeper than those caused by Ar plasma. The effectiveness of the PRS-based methodology has been demonstrated, and our findings are expected to be useful in analyzing physical damage, evaluating its effects on device performance, and designing optimal etching and post-etch processes.

4.6. References

[1] K. Eriguchi, Y. Nakakubo, A. Matsuda, M. Kamei, Y. Takao, and K. Ono, "Trade-Off Relationship between Si Recess and Defect Density Formed by Plasma-Induced Damage in Planar Metal–Oxide–Semiconductor Field-Effect Transistors and the Optimization Methodology," *Jpn. J. Appl. Phys.*, vol. 50, 08KD04, Aug. 2011.

[2] H. Wada, M. Agata, K. Eriguchi, and A. Fujimoto, "Photoreflectance characterization of the plasma-induced damage in Si substrate," *J. Appl. Phys.*, vol. 88, no. 5, pp. 2336–2341, Sep. 2000.

[3] D. E. Aspnes and J. E. Rowe, "Resonant Nonlinear Optical Susceptibility: Electroreflectance in the Low-Field Limit," *Phys. Rev. B*, vol. 5, no. 10, pp. 4022–4030, May 1972.

[4] A. Fujimoto, H. Katsumi, M. Okuyama, and Y. Hamakawa, "Contactless Measurement of Surface Temperature and Surface Potential of Si by Photoreflectance Spectroscopy," *Jpn. J. Appl. Phys.*, vol. 34, part 1, no. 2B, pp. 804–807, Feb. 1995.

[5] R. Ditchfield, D. Llera-Rodríguez, and E. G. Seebauer, "Semiconductor surface diffusion: Nonthermal effects of photon illumination," *Phys. Rev. B*, vol. 61, no. 20, pp. 13710–13720, May 2000.

[6] S. M. Sze, *Physics of Semiconductor Devices*, 2nd ed. New York: Wiley-Interscience, 1981.

[7] X. Yin, H.-M. Chen, F. H. Pollak, Y. Chan, P. A. Montano, P. D. Kirchner, G. D. Pettit, and J. M. Woodall, "Photoreflectance study of the surface Fermi level at (001) n- and p-type GaAs surfaces," *J. Vac. Sci. Technol. A*, vol. 10, no. 1, pp. 131–136, Jan. 1992.

[8] K. Eriguchi, A. Ohno, D. Hamada, M. Kamei, H. Fukumoto, and K. Ono, "Quantitative characterization of plasma-induced defect generation process in exposed thin Si surface layers," *Jpn. J. Appl. Phys.*, vol. 47, no. 4, pp. 2446–2451, Apr. 2008.

[9] K. Eriguchi and K. Ono, "Quantitative and comparative characterizations of plasma process-induced damage in advanced metal-oxide-semiconductor devices," *J. Phys. D*, vol. 41, no. 2, 024002, Jan. 2008.

[10] K. Eriguchi, A. Ohno, D. Hamada, M. Kamei, and K. Ono, "Estimation of defect generation probability in thin Si surface damaged layer during plasma processing," *Thin Solid Films*, vol. 516, no. 19, pp. 6604–6608, Aug. 2008.

[11] A. Matsuda, Y. Nakakubo, Y. Takao, K. Eriguchi, and K. Ono, "Modeling of

Ion-Bombardment Damage on Si Surfaces for In-Line Analysis," *Thin Solid Films*, vol. 518, no. 13, pp. 3481–3486, Apr. 2010.

[12] P. Pan, L. A. Nesbit, R. W. Douse, and R. T. Gleason, "The Composition and Properties of PECVD Silicon Oxide Films," *J. Electrochem. Soc.*, vol. 132, no. 8, pp. 2012–2019, Aug. 1985.

[13] G. A. C. M. Spierings, "Wet chemical etching of silicate glasses in hydrofluoric acid based solutions," *J. Mater. Sci.*, vol. 28, no. 23, pp. 6261–6273, Dec. 1993.

[14] K. Eriguchi, Y. Nakakubo, A. Matsuda, Y. Takao, and K. Ono, "Model for Bias Frequency Effects on Plasma-Damaged Layer Formation in Si Substrates," *Jpn. J. Appl. Phys.*, vol. 49, 056203, May 2010.

[15] J. Lindhard and M. Scharff, "Energy Dissipation by Ions in the kev Region," *Phys. Rev.*, vol. 124, no. 1, pp. 128–130, Oct. 1961.

[16] M. Fukasawa, Y. Nakakubo, A. Matsuda, Y. Takao, K. Eriguchi, K. Ono, M. Minami, F. Uesawa, and T. Tatsumi, "Structural and electrical characterization of HBr/O_2 plasma damage to Si substrate," *J. Vac. Sci. Technol. A*, vol. 29, 041301, Jun. 2011.

[17] T. Ito, K. Karahashi, M. Fukasawa, T. Tatsumi, and S. Hamaguchi, "Si Recess of Polycrystalline Silicon Gate Etching: Damage Enhanced by Ion Assisted Oxygen Diffusion," *Jpn. J. Appl. Phys.*, vol. 50, 08KD02, Aug. 2011.

5. Temperature-Controlled Photoreflectance Spectroscopy

5.1. Introduction

PRS-based damage quantification cannot be applied in cases where the damage is severe, *i.e.* when the mean incident ion energy ($\bar{E}_i$) is higher than a certain limit. This problem stems from the characteristics of the method, in which the spectral signal intensity decreases with the density of defects, until the intensity becomes lower than the background fluctuation. For example, the limit in earlier reports using a DC plasma source existed in the range $350 \leq \bar{E}_i \leq 400$ eV [1], [2]. For energies above this limit, PR spectra were lost in the noise and could not be fitted to the third-derivative functional form (TDFF), which has prevented quantitative damage evaluation by PRS.

To address this problem, a temperature-controlled PRS technique is considered, where the sample is cooled to a cryogenic temperature using liquid nitrogen (LN_2). The technique is applied to Si wafers damaged by various incident ion energies from Ar plasma. By obtaining the laser power dependence of the TDFF parameters, the damage is quantitatively evaluated. Effects that contribute to the temperature dependence of the PR spectrum will be discussed and compared with the experimental results.

5.2. Experimental procedure

5.2.1. Plasma exposure

The ICP reactor introduced in chapter 3 was used. N-type Si (100) wafers (resistivity: 0.02 Ωcm) were placed on a wafer stage of the ICP reactor and exposed to Ar plasma. The chamber pressure was 20 mTorr. The exposure time was 30 s. A 13.56 MHz bias power was applied to the wafer stage. The bias power P_{bias} was varied from 0 (no bias) to 400 W to control the energies of ions impinging onto the wafer surface. The average energy of incident ions was estimated as $\bar{E}_{\mathrm{i}} = e(V_{\mathrm{p}} - V_{\mathrm{dc}})$, where e is the elementary charge, V_{dc} (< 0) is the DC self-bias voltage monitored with an oscilloscope, and V_{p} is the plasma potential determined by plasma diagnosis using a Langmuir probe.

5.2.2. Measurement

To observe temperature (T) dependence of the PR spectra, we prepared an apparatus capable of performing cryogenic measurements. The measurement stage can be cooled by circulating liquid nitrogen in the stage (LN_2). The stage temperature was measured by a thermocouple placed inside the stage. The chamber was vacuum-pumped using Alcatel Adixen SD 2005 Pascal rotary pump (RP) and Pfeiffer TMU 071 P turbo molecular pump (TMP) to keep the chamber pressure $p < 5\times10^{-3}$ Pa during low-temperature measurements, to prevent frost. p was monitored by CC-10 crystal/cold cathode gauge. The apparatus shares many of the components with the apparatus employed for the experiment in chapter 4: a xenon light source from JY UVISEL ellipsometer system for the probe beam, HR460 monochromator coupled to a photomultiplier (PMT), and SR830 lock-in amplifier. A laser unit

housing a diode-pumped solid-state laser (Laser-Export LCS-DTL-318) was used for the modulation beam. The beams were guided with single-core optical fibers (core diameter: 800 μm). The modulation beam was chopped at 500 Hz by a mechanical chopper inside the laser housing.

Measurement procedure was as follows. Measurements in phases A and C are measurements for quantitative analysis of the damage; those in phases B and D are quick measurements to monitor the time evolution of the system.

Phase A: Room temperature

The sample was placed in the chamber and its PR spectrum was obtained at room temperature under following conditions: chopper frequency f_c = 500 Hz, PMT voltage $V_{PMT} = -300$ V, lock-in amplifier filter 24 dB, integration time t_{int} = 3 s/point. Modulation laser power (I_p) was varied from 5 to 200 mW to obtain the I_p dependence of the PR spectrum.

Phase B: Cooling

LN_2 was poured into the vacuum-pumped Dewar flask. Measurement with a fixed modulation laser power I_p = 100 mW was repeatedly performed until stabilization of stage temperature. t_{int} was either 1 s/point (for ctrl) or 3 s/point (for dam), to achieve optimal balance between the signal-to-noise (S/N) ratio and time required for one cycle of measurement. All the other parameters were not changed from Phase A.

Phase C: Cryogenic measurement

After stable temperature was achieved, the I_p dependence of the PR spectrum was obtained by performing measurements with various values of I_p (5–200 mW). Parameters were not changed from phase A.

Phase D: Return trip

We then waited for the LN_2 to evaporate completely, at which point the temperature started rising. Measurement with $I_p = 100$ mW was repeatedly performed, in a manner equivalent to Phase B, until the stage temperature was higher than 273 K.

Phase E: Room temperature (confirmation)

After sufficient time (over 16 hours) has passed and the stage has reached room temperature, measurements were performed, in a manner equivalent to Phase A, to see whether the spectra matches those obtained in Phase A.

After the measurements, each spectrum was fitted to the third-derivative functional form (TDFF) as mentioned in chapter 4.

$$\frac{\Delta R}{R} = \Re\left[C\mathrm{e}^{i\theta}\left(E - E_\mathrm{g} + i\Gamma\right)^{-n}\right], \tag{5.1}$$

$$C = P_1 \ln\left(P_2 I_p + 1\right), \tag{5.2}$$

$$P_1 = \frac{c_1}{\mu_\parallel}\frac{\eta k_\mathrm{B} T}{e}, \tag{5.3}$$

$$P_2 = c_2 \frac{e\gamma(1-R)}{A^* T^2 h\nu}\exp\left(\frac{eV_\mathrm{s}}{k_\mathrm{B}T}\right). \tag{5.4}$$

Change in the surface potential ΔV_s and defect density N_dam was quantified from the I_p dependence as

$$\Delta V_\mathrm{s} = \frac{k_\mathrm{B}T}{e}\ln\left(\frac{P_2^\mathrm{dam}}{P_2^\mathrm{ctrl}}\right), \tag{5.5}$$

$$N_\mathrm{dam} = -\frac{\varepsilon_\mathrm{Si}\varepsilon_0}{e}\frac{\Delta V_\mathrm{s}}{d_\mathrm{c}}. \tag{5.6}$$

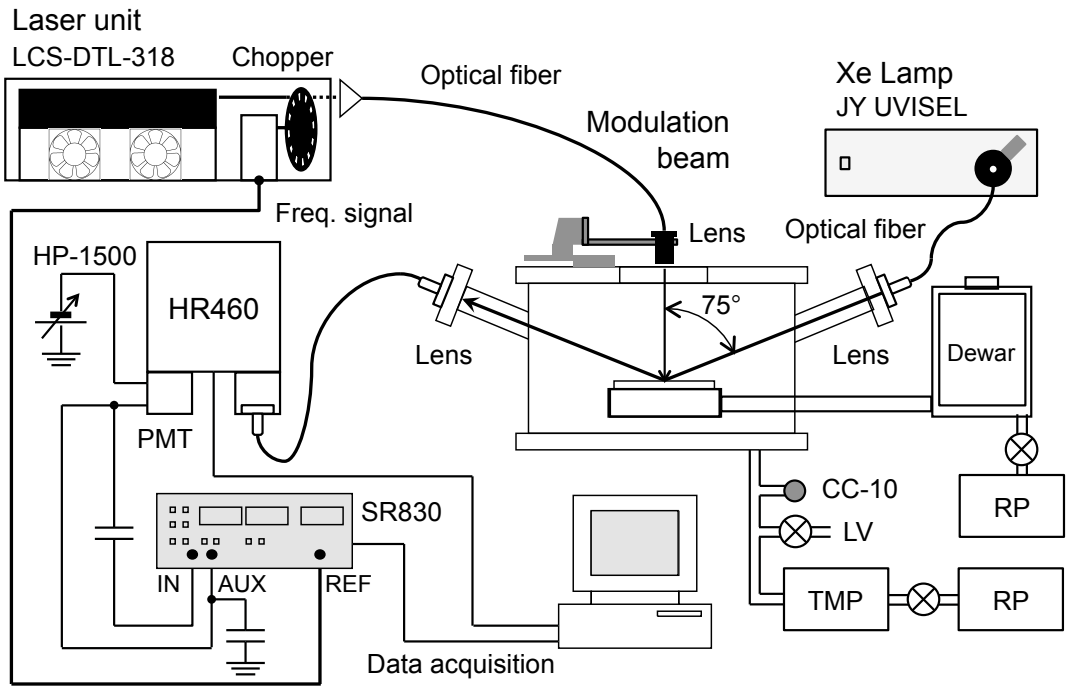

Fig. 5.1 Apparatus for temperature-controlled PR measurements.

5.3. Results and discussion

5.3.1. Plasma parameters and PR spectra

V_p was 11 V without stage bias, and 14–15 V with bias. n_e was 3.0–3.1 × 10^{11} cm^{-3}. T_e was 3.1–3.7 eV. $\bar{E}_i$ was calculated as shown in Table 5.1.

Table 5.1 Estimated average incident ion energy and TDFF parameters for each sample.

P_{bias}	$\bar{E}_i$	$T = 300$ K			$T = 90$ K		
(W)	(eV)	E_g (eV)	Γ (eV)	θ	E_g (eV)	Γ (eV)	θ
Control	N/A	3.37	0.14	1.4	3.46	0.09	1.8
0	11	3.38	0.12	1.9	3.44	0.08	2.0
50	80	3.37	0.15	2.0	3.42	0.10	1.9
100	150	3.33	0.15	1.3	3.41	0.10	1.8
200	210	3.34	0.15	1.7	3.43	0.11	2.5
250	260	3.34	0.14	2.1	3.43	0.11	2.8
300	300	3.33	0.14	2.0	3.41	0.12	2.5
400	420	No peak			3.36	0.14	1.2

With introduction of LN_2, the stage temperature T achieved equilibrium at 89–90 K. The temperature history is shown as solid lines in Fig. 5.2. The equilibrium point was significantly higher than the boiling point of N_2, 77.4 K. This is probably due to influx of heat from irradiation of light and via the chamber walls. The latter was found to be much more significant, as a control experiment with modulation and probe beams turned off resulted in temperature no lower than 88.0 K.

The spectra at 300 K and 90 K are compared in Fig. 5.3. Before we discuss damaged samples, let us focus on the reference sample, Fig. 5.3(a). We can observe the following T-dependent characteristics: by cooling the sample to 90 K, E_g increased, Γ decreased (these two characteristics are also apparent in Fig. 5.2), and the signal intensity increased, in comparison to the measurement at 300 K. These will be discussed in the following subsections.

Fitting the spectrum of each sample to Eq. (5.1) gives us the values for the four TDFF parameters C, E_g, Γ, and θ. In order to perform the fitting, the dimensionality of the critical point must be assumed to determine the value for n. We will assume $n = 3$ for a reason that will be clarified later.

The results for E_g, Γ, and θ are shown in Table 5.1. (C will be discussed later.) The critical point energy E_g of plasma-exposed samples showed a redshift (a shift to a lower photon energy) in comparison to the control under the same T. The shift can be attributed to the band-edge tailing due to defect states [3]–[5] or a change in mechanical strain near the surface due to the formation of the damaged layer [1], [6], [7].

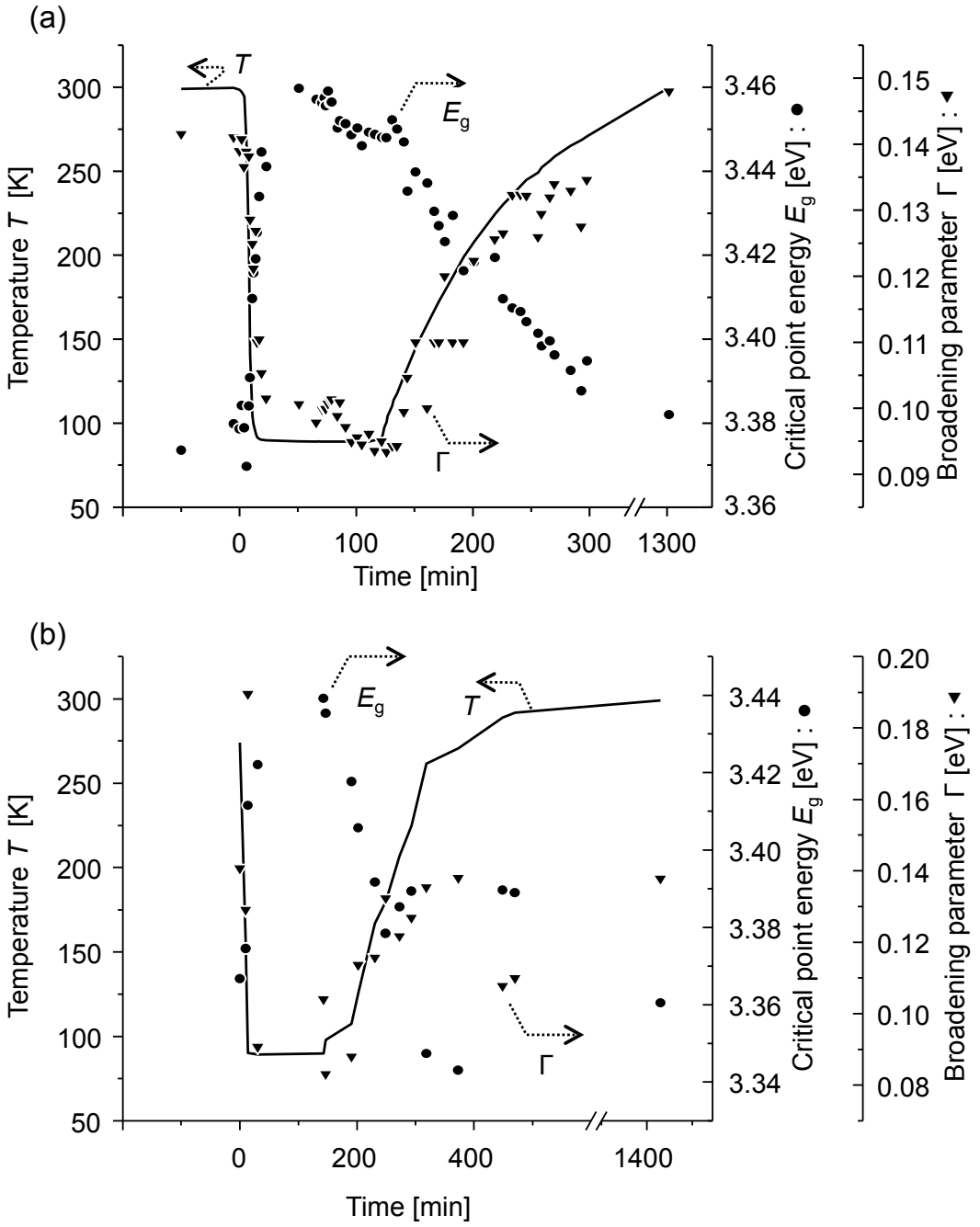

Fig. 5.2 Time evolution of temperature T (solid line), critical point energy E_g (●), and broadening parameter Γ (▼). (a) Unexposed control sample (t_{int} = 1s) and (b) plasma-exposed sample (P_{bias} = 200 W, t_{int} = 3 s). Fitting calculations to obtain the TDFF parameters for (b) were less stable than for (a).

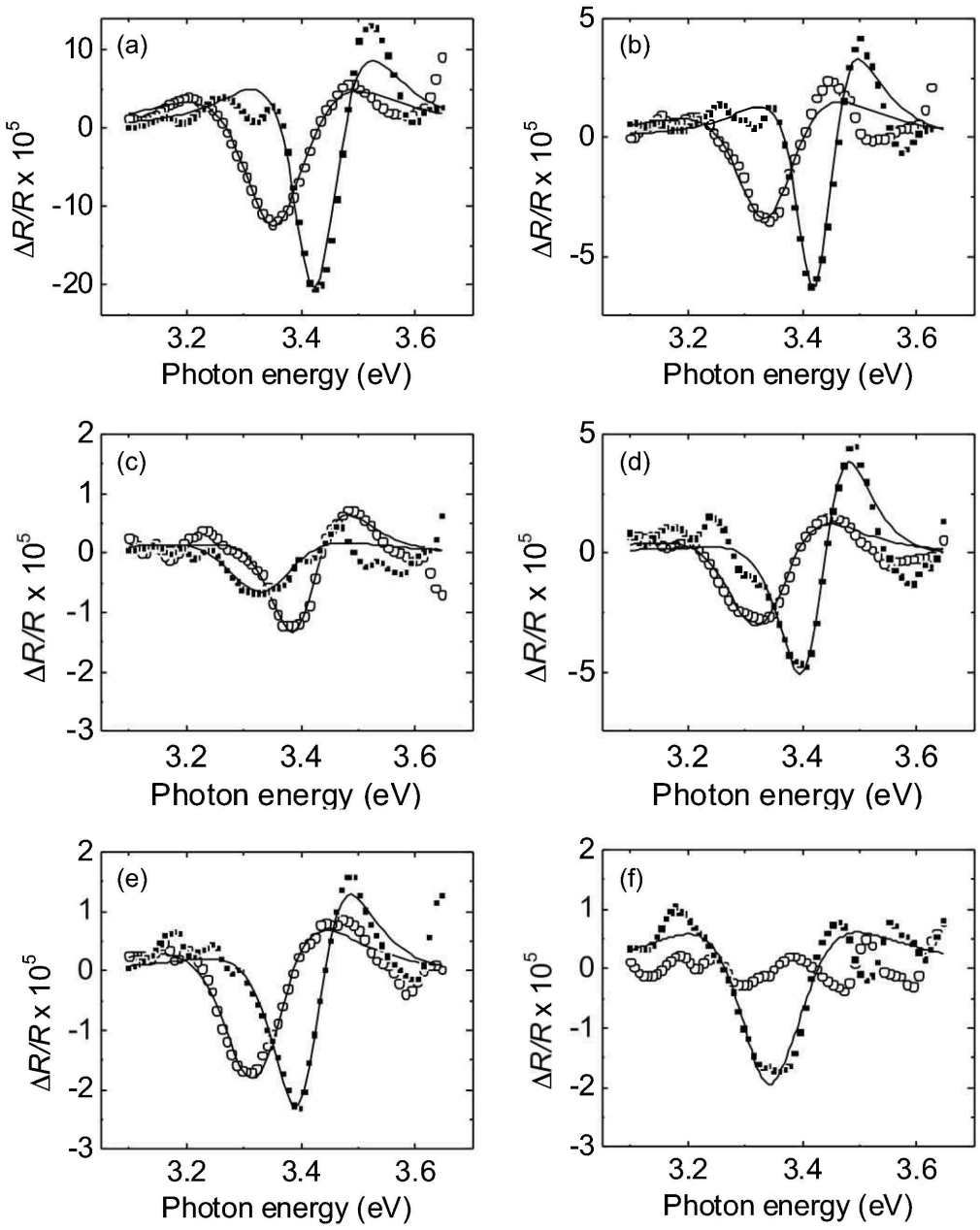

Fig. 5.3 PRS spectra. (a) Control (unexposed). (b) No bias ($P_{\text{bias}} = 0$ W). (c) 100 W. (d) 250 W. (e) 300 W. (f) 400 W.

5.3.2. Interband critical point E_g

As explained in chapter 2, the optical property of Si has a complex structure at around 3.4 eV [8]–[10]. Two types of optical transitions are possible in this range, namely the E_1 transition that take place along the Λ directions near the L point of the Brillouin zone ($n = 3$) and the E_0' transition at the Γ point ($n = 5/2$). The two are nearly degenerate in energy, and there have been many discussions on their roles in the PR spectra [11]–[16]. The temperature dependence of E_g that we have observed in our experiment give us insight into this discussion.

The temperature dependence of E_g is typically formulated using one of the two following expressions [17]. One is the semi-empirical Varshni relationship [18],

$$E_g(T) = E_g(0) - \frac{\alpha T^2}{\beta + T}, \tag{5.7}$$

where α and β are constants. The other is the Bose–Einstein (BE) type expression [13], [16],

$$E_g(T) = E_B - a_B\left[1 + \frac{2}{\exp(\Theta/T) - 1}\right], \tag{5.8}$$

where E_B and a_B are constants, and the average phonon frequency is expressed by $k_B\Theta/\hbar$. Both expressions contain contributions from both lattice dilation due to thermal expansion and electron–phonon coupling effects [17]. In the range 350–820 K, E_1 and E_0' transitions are considered as one structure that shows a linear behavior,

$$E_g(T) = E_c - \lambda T. \tag{5.9}$$

The values given by these expressions are plotted on Fig. 5.4, where the values for $E_g(0)$, α, β, E_B, a_B, E_c, λ, and Θ were taken from Lautenschlager *et al.* [13]. Both expressions are shown for both of the critical points E_1 and E_0'.

The locus of the experimental values that we obtained is plotted on the same graph, from room temperature (A) to cryogenic temperature (B→C) and back (D→E). The circles show the values calculated under the assumption that $n = 3$ (E_1), and the crosses show those under the assumption that $n = 5/2$ (E_0'). Phase B shows a large departure from the Varshni/BE curves because this phase was the course of rapid cooling by LN_2 introduction and the system is not in equilibrium (the cooling of the sample is delayed as compared to the stage temperature that is being measured); but after the system achieves equilibrium, the experimental values show a good agreement with the Varshni/BE curves for E_1 transition, regardless of which value was assumed for n. This result clearly shows that assuming $n = 5/2$ is an error, and the E_1 transition $(n = 3)$ plays a much more significant role in the PR spectra at 3.4 eV.

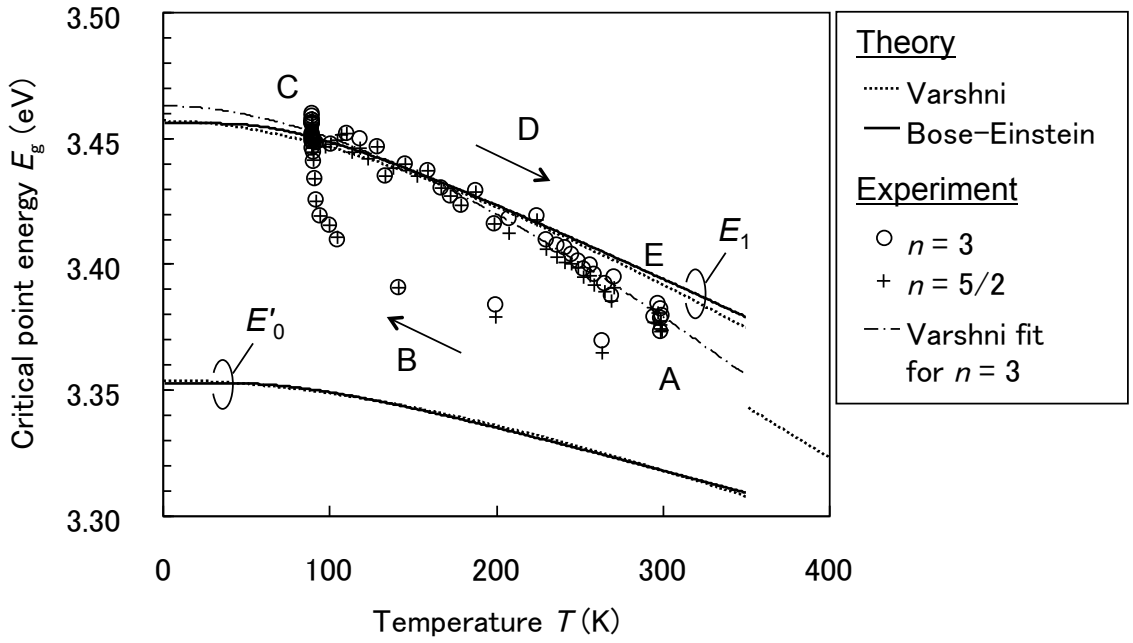

Fig. 5.4 Semi-empirical Varshni expression and Bose–Einstein-type expression of the temperature dependence of E_g for the two transitions: E_1 and E'_0; and the locus of E_g obtained experimentally, from phase A to E via phase C. A best-fit Varshni-type curve for our experimental data is also shown for reference.

5.3.3. Broadening parameter Γ and the increase in signal intensity

Next, we will discuss a cause of the increase in signal intensity by cooling. On the basis of the third-derivative theory, we will mainly focus on the temperature dependence of four TDFF parameters: C, θ, E_g, and Γ.

As expressed in Eqs. (5.2)–(5.4), many effects contribute to the temperature dependence of the amplitude parameter C. P_1 increases with temperature, while P_2 decreases. η may either be proportional to $1/k_B T$ or be near unity depending on whether the tunneling current through the surface Schottky barrier is significant [19]. The surface potential V_s also varies with temperature [4], [20].

The phase factor θ is determined by the asymmetry of the lineshape (the ratio of the absolute magnitudes of the positive and negative extrema) [11]. For our experiment, we can see from our data that neither the change in temperature nor exposure to plasma had a significant effect on the asymmetry of the lineshape. Therefore, there is no need to focus on θ in the scope of this work.

The temperature dependence of E_g was discussed in the previous subsection.

Many mechanisms determine the broadening parameter (Γ), but its *temperature dependence* is related only to the electron–phonon interaction [17]. The temperature dependence of Γ can be expressed in a BE-type expression,

$$\Gamma(T) = \Gamma_0 \left[1 + \frac{2}{\exp(\Theta/T) - 1}\right] + \Gamma_1 , \tag{5.10}$$

where Γ_0 corresponds to electron–phonon coupling, and Γ_1 is determined by combined effects of *temperature-independent* broadening mechanisms, such as

electron–electron interaction, impurity scattering, and dislocation scattering [17], [21]. For higher temperatures ($T > 350$ K) the formulation

$$\Gamma(T) = \Gamma_M + cT^2 \tag{5.11}$$

is used, but this temperature range is out of the scope of this work.

In a similar manner as was done with E_g, the BE curves and the experimental data are compared in Fig. 5.5. Since Γ_1 is unknown, the BE curves has been plotted as $\Gamma_1 = 0$, following Lautenschlager *et al.* [13]. A nonzero Γ_1 would simply shift the curves upward. The experimental data deviated from the E_1 BE curve, which can be explained by a nonzero Γ_1, perhaps due to impurities or other imperfections in the experimentation.

Using Eqs. (5.8) and (5.10), we can simulate the TDFF expressed by Eq. (5.1) using the values [13] for the E_1 transition. It is evident from Eq. (5.1) that the amplitude factor C only scales the lineshape determined by E_g, Γ, θ, and n and does not play any role in the actual lineshape determination [11]. Moreover, the temperature dependence of C cannot be expressed in a relatively simple model like E_g or Γ. For these reasons, C was fixed to an arbitrary value, despite its decrease by cooling in the experiment. Any discrepancy that may arise from this simplification could easily be addressed by scaling the lineshape afterwards. The phase factor was fixed at $\theta = \pi/2$. From previous discussion, $n = 3$. The spectra calculated using this model are shown in Fig. 5.6. The change in spectral lineshape is similar to those observed in the experiment: a shift towards a higher E and an increase in $|\Delta R/R|$. We should stress that C is fixed in this model; the increase in $|\Delta R/R|$ is caused by the temperature-dependent decrease in Γ. The ratio between the intensities of the two signals was larger than that observed experimentally. This can be attributed to the decrease in C, as we shall see in the next subsection.

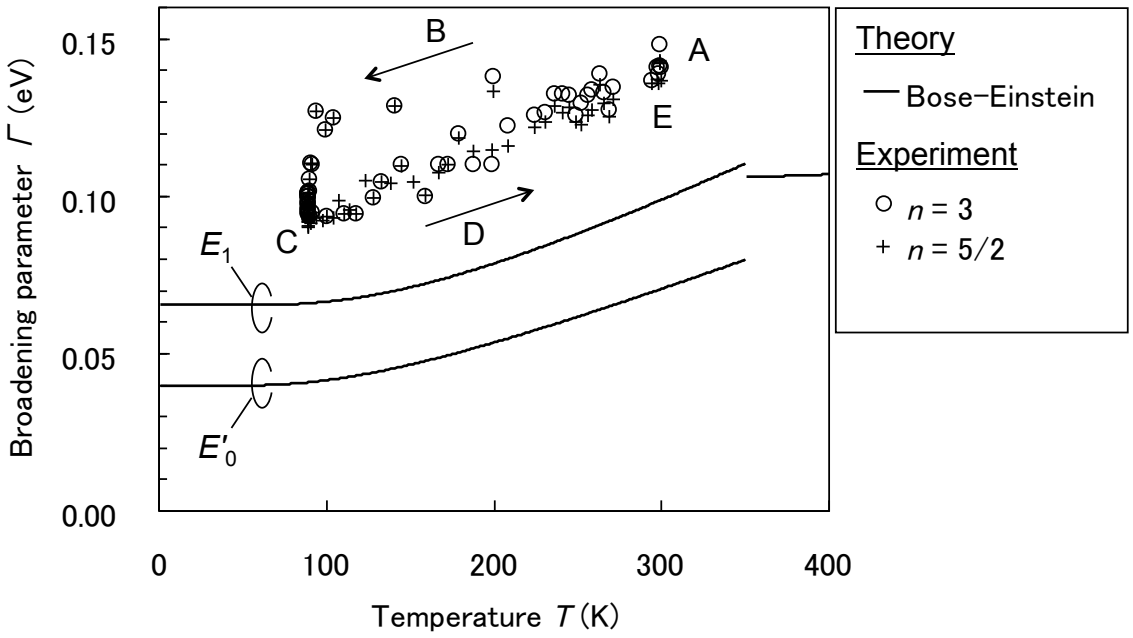

Fig. 5.5 Bose–Einstein-type expression of the temperature dependence of Γ for the two transitions: E_1 and E_0'; and the locus of Γ obtained experimentally.

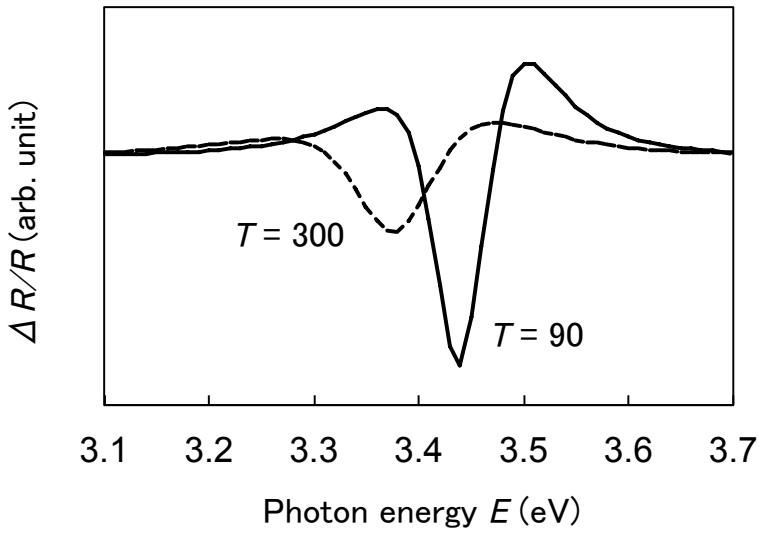

Fig. 5.6 Modeled temperature dependence of the TDFF for a clean Si. Compare with Fig. 5.3.

5.3.4. Defect site density

Let us go back to Fig. 5.3 and compare the spectra among the samples. In the same trend as was reported by Eriguchi *et al.* [1], $|\Delta R/R|$ decreased at higher E_i values. At $P_\mathrm{bias} = 400$ W ($E_\mathrm{i} \cong 420$ eV), the peak can no longer be observed, presumably because the signal intensity became smaller than the background fluctuation. Next, let us compare the spectra between the two temperatures for each sample. As explained in the previous section, the decrease in the broadening parameter Γ caused the signal intensity to increase for all the samples. For $P_\mathrm{bias} = 400$ W, a peak can now be observed at 90 K, which was unobservable at 300 K.

Fig. 5.7 shows the laser power (I_p) dependence of C. The curves were fitted to Eq. (5.2) to extract the parameters P_1 and P_2. Note the slight decrease of their values at 90 K, of which its reason is not clear but still serves to explain the issue raised in the previous section: a weaker T dependence of the signal intensity than the theoretical expectation (compare Fig. 5.3 and Fig. 5.6).

From P_2, the areal density of the charges trapped in the defect sites (N_dam) were estimated using Eqs. (5.5) and (5.6). The results are shown in Fig. 5.8. The defect density was quantified to be $N_\mathrm{dam} \sim 10^{11} - 10^{12}$ cm^{-2}. Quantitative analysis of the rightmost sample ($\bar{E}_\mathrm{i} = 420$ eV) was made possible for the first time by cooling the sample.

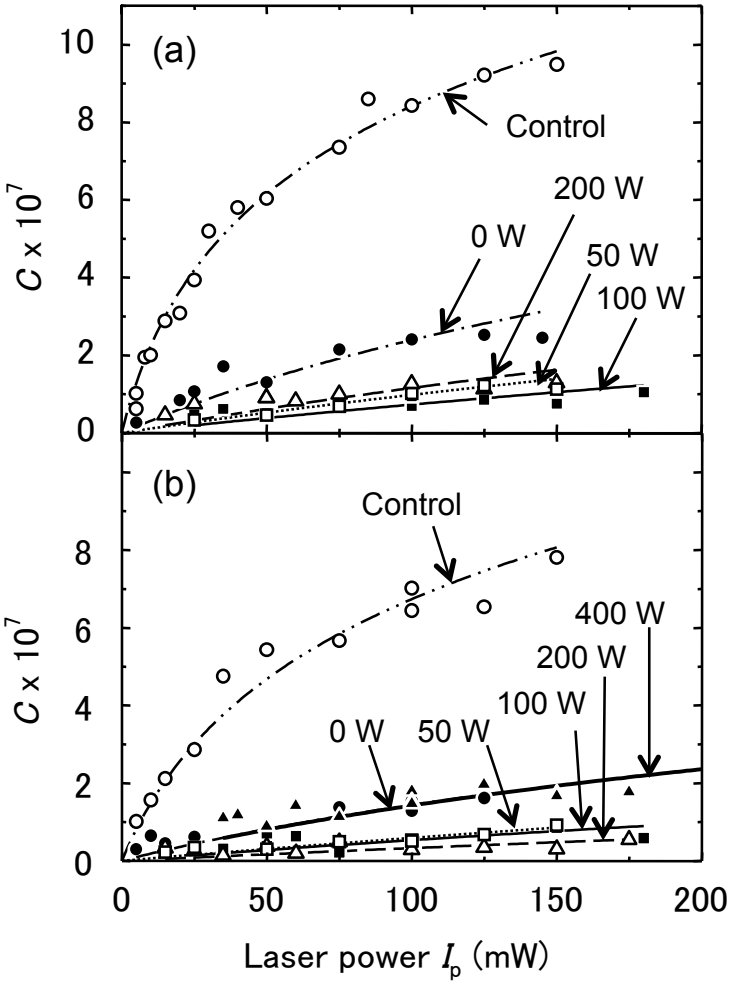

Fig. 5.7 Amplitude factor (C) as function of modulation laser power (I_p): (a) 300K and (b) 90 K. The lines show the fitting curves expressed by Eq. (5.2).

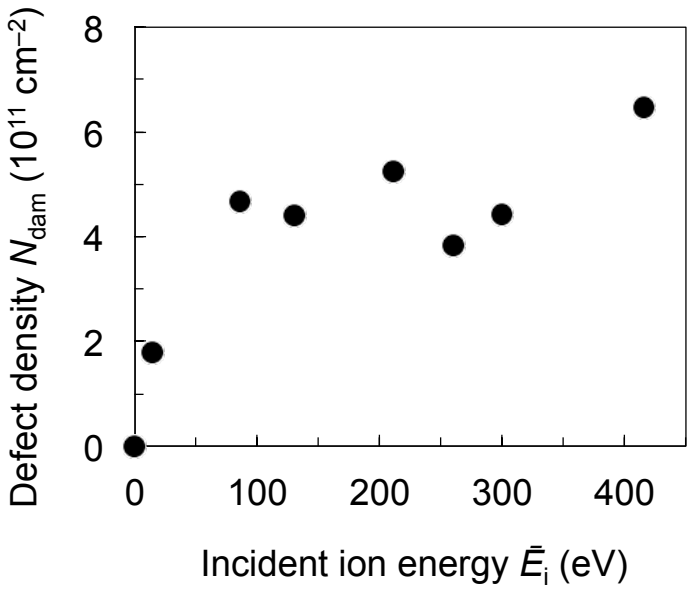

Fig. 5.8 Calculated areal density of the carriers trapped at the defect sites at 90 K, as a function of estimated incident ion energy.

5.4. Conclusion

An advanced photoreflectance spectroscopy technique for optically evaluating physical damage on Si, where the samples were cooled using LN_2, was proposed. By analyzing the temperature dependence of E_g, we were able to identify the optical transition that participates in determining the PR spectrum at 3.4 eV: the E_1 is the dominant transition, with participation of the E_0' transition being minor. This finding contributes to closer understanding of the PR measurements on Si, and allows more accurate analysis of its optical characteristics.

Also, by reducing the temperature from 300 to 90 K, the signal intensity was increased. This technique enables the quantitative analysis possible even for a heavily damaged sample, which could not be carried out at 300 K. The primary cause of the signal enhancement was attributed to the decrease in the broadening parameter Γ. The areal defect density was confirmed to be a function of $\bar{E}_i$, and was estimated to be up to about 7×10^{-11} cm^{-2} for the most heavily damaged sample.

5.5. References

[1] K. Eriguchi, A. Ohno, D. Hamada, M. Kamei, H. Fukumoto, and K. Ono, "Quantitative characterization of plasma-induced defect generation process in exposed thin Si surface layers," *Jpn. J. Appl. Phys.*, vol. 47, no. 4, pp. 2446–2451, Apr. 2008.

[2] K. Eriguchi, A. Ohno, D. Hamada, M. Kamei, and K. Ono, "Estimation of defect generation probability in thin Si surface damaged layer during plasma processing," *Thin Solid Films*, vol. 516, no. 19, pp. 6604–6608, Aug. 2008.

[3] Y. Nakakubo, A. Matsuda, M. Fukasawa, Y. Takao, T. Tatsumi, K. Eriguchi, and K. Ono, "Optical and Electrical Characterization of Hydrogen-Plasma-Damaged Silicon Surface Structures and Its Impact on In-line Monitoring," *Jpn. J. Appl. Phys.*, vol. 49, 08JD02, Aug. 2010.

[4] 犬石嘉雄, 浜川圭弘, 白藤純嗣, 半導体物性II ―素子と物性―, 東京: 朝倉書店, 1977.

[5] A. Matsuda, Y. Nakakubo, R. Ogino, H. Ohta, K. Eriguchi, and K. Ono, "Simulation and Experimental Study on the Characteristics of Plasma-Induced Damage and Methodology for Accurate Damage Analysis," in *Proc. Int. Conf. Integr. Circuit Design & Technol.*, Austin, Texas, 2009, pp. 97–100.

[6] M. Murtagh, S. M. Lynch, P. V. Kelly, S. Hildebrandt, P. A. F. Herbert, C. Jeynes, and G. M. Crean, "Photoreflectance characterisation of Ar^+ ion etched and $SiCl_4$ reactive ion etched silicon (100)," *Mater. Sci. Tech.*, vol. 13, no. 11, pp. 961–964, Nov. 1997.

[7] M. Morifuji, P. Yongwattanasoontorn, K. Taniguchi, C. Hamaguchi, and Y. Ozawa, "Strain Evaluation at Si/SiO_2 Interface Using the Electroreflectance Method," *Jpn. J. Appl. Phys.*, vol. 32, part 1, no. 6A, pp. 2735–2739, Jun. 1993.

[8] P. Y. Yu and M. Cardona, *Fundamentals of Semiconductors*. Berlin: Springer-Verlag,

1996.

[9] S. Adachi, "Model dielectric constants of Si and Ge," *Phys. Rev. B*, vol. 38, no. 18, pp. 12966–12976, Dec. 1988.

[10] A. Daunois and D. E. Aspnes, "Electroreflectance and ellipsometry of silicon from 3 to 6 eV," *Phys. Rev. B*, vol. 18, no. 4, pp. 1824–1839, Aug. 1978.

[11] D. E. Aspnes, "Third-derivative modulation spectroscopy with low-field electroreflectance," *Surf. Sci.*, vol. 37, pp. 418–442, Jun. 1973.

[12] D. E. Aspnes and J. E. Rowe, "Resonant Nonlinear Optical Susceptibility: Electroreflectance in the Low-Field Limit," *Phys. Rev. B*, vol. 5, no. 10, pp. 4022–4030, May 1972.

[13] P. Lautenschlager, M. Garriga, L. Viña, and M. Cardona, "Temperature dependence of the dielectric function and interband critical points in silicon," *Phys. Rev. B*, vol. 36, no. 9, pp. 4821–4830, Sep. 1987.

[14] K. Kondo and A. Moritani, "Symmetry analysis and uniaxial-stress effect on the low-field electroreflectance of Si from 3.0 to 4.0 eV," *Phys. Rev. B*, vol. 14, no. 4, pp. 1577–1592, Aug. 1976.

[15] M. Sohgawa, M. Agata, T. Kanashima, K. Yamashita, K. Eriguchi, A. Fujimoto, and M. Okuyama, "Nondestructive and contactless monitoring technique of Si surface stress by photoreflectance," *Jpn. J. Appl. Phys.*, vol. 40, no. Part 1, No. 4B, pp. 2844–2848, Apr. 2001.

[16] L. Viña, S. Logothetidis, and M. Cardona, "Temperature dependence of the dielectric function of germanium," *Phys. Rev. B*, vol. 30, no. 4, pp. 1979–1991, Aug. 1984.

[17] F. H. Pollak and H. Shen, "Modulation spectroscopy of semiconductors: bulk/thin film, microstructures, surfaces/interfaces and devices," *Mater. Sci. Eng. R*, vol. 10, no. 7–8, pp. 275–374, Oct. 1993.

[18] Y. P. Varshni, "Temperature dependence of the energy gap in semiconductors,"

Physica, vol. 34, no. 1, pp. 149–154, 1967.

[19] S. M. Sze, *Physics of Semiconductor Devices*, 2nd ed. New York: Wiley-Interscience, 1981.

[20] A. Fujimoto, H. Katsumi, M. Okuyama, and Y. Hamakawa, "Contactless Measurement of Surface Temperature and Surface Potential of Si by Photoreflectance Spectroscopy," *Jpn. J. Appl. Phys.*, vol. 34, part 1, no. 2B, pp. 804–807, Feb. 1995.

[21] P. Lautenschlager, P. B. Allen, and M. Cardona, "Phonon-induced lifetime broadenings of electronic states and critical points in Si and Ge," *Phys. Rev. B*, vol. 33, no. 8, pp. 5501–5511, Apr. 1986.

6. Conclusion

6.1. Summary

This study established the following findings:

1. The composition and structure of the damaged layers were studied by using RBS, HRTEM, and MD simulation.
2. For characterization of plasma-damaged wafer surfaces with spectroscopic ellipsometry, an interface layer should be included in the optical model to address the clarified composition and structure. The interface layer should be modeled as a mixture of Si and SiO_2 phases.
3. Depth profiles of the damaged layers were experimentally acquired by wet-etching the damaged layers and by measuring the samples using aforementioned improvement in the optical model for spectroscopic ellipsometry and surface voltage quantification by photoreflectance spectroscopy. The structures of the damaged layers created by Ar and He plasmas were compared and discussed.
4. Temperature-controlled photoreflectance spectroscopy technique was performed, where the sample was cooled with liquid nitrogen. Temperature dependence of E_g gave insight into the interband critical points of Si, and clarified the dominant optical transition that determines

the photoreflectance spectra to be the E_1 transition.

5. Temperature dependence of the broadening parameter Γ caused the increase in the signal intensity under a cryogenic condition. This allowed damage quantification for heavily damaged samples with a low signal-to-noise ratio, thereby extending the applicable range of the damage quantification technique.

6.2. Future issues and brief outlook

Since ΔR in PR measurements of Si is very small in comparison to R, it is extremely sensitive to the imperfections in the light source, stray lights, or fluctuations in the frequency of the mechanical chopper. The PR spectra that we have observed had a characteristic "noise" or a background fluctuation. We have tried several alterations to the system, including deployment of an advanced light source, but were not able to pinpoint the cause of the "noise" and this issue remains unsolved.

Also, our PR measurements required significant amount of time to obtain a spectrum. Perhaps we could compensate for this by performing a single-wavelength measurement as opposed to obtaining the full spectrum; because for the purpose of damage characterization, the signal intensity is our primary concern. This cuts down the time required for a measurement to about 1/100. However, this simple is not without its shortcomings. The formation of the damaged layer causes not only the decrease in the signal intensity but also a shift in E_{g}. Moreover, both the blueshifts (shifts to higher energies) and redshifts (shifts to lower energies) have been observed in plasma-damaged surfaces [1]–[3]. We have suggested that the difference in strain could be a

possible cause of this difference [3], but until this matter is clarified, a single-wavelength measurement can only indicate an unidentified deviation from a reference measurement. Alternatively, recent developments such as the rapid photoreflectance (RPR) measurement using an array detector [4] should contribute to increasing the feasibility of PRS as a damage characterization technique.

The apparatuses for photoreflectance spectroscopy and spectroscopic ellipsometry share many of their components, and they could be integrated into a single apparatus (*e.g.* Ref. [5]). Also, microspot measurements (typical spot sizes: 25–100 μm) would be suitable for measuring small target gratings etched in the scribe lines between the chips [6]. Microspot spectroscopic ellipsometry is already a commonplace, and likewise, a microspot photoreflectance spectroscopy is a strong candidate for an advanced optical characterization technique [7]. It is anticipated that such techniques would be useful in production lines for accurate monitoring of damage, to realize devices with minimal effects of physical damage.

The discussion in this dissertation specifically covered the effects of physical damage on today's conventional planar MOSFETs. However, in the last few years, we are seeing new challenges. One recent strategy is the multigate FET (MuGFET, FinFET) [8], [9], where its channel is surrounded by several gates on multiple surfaces. Gate etching of FinFETs require longer over-etch time than conventional planar gates (and therefore more likely to suffer from damage in the substrate); and Si loss (Si recess) continues to be a problem in FinFETs [10]. Therefore, the issues covered in this thesis will continue to be crucial points to consider, and the damage characterization methodology will be even more important. It is anticipated that the results of

this work, in combination with other related arts, would play a notable role in further progress of the electronics industry.

6.3. References

[1] M. Murtagh, S. M. Lynch, P. V. Kelly, S. Hildebrandt, P. A. F. Herbert, C. Jeynes, and G. M. Crean, "Photoreflectance characterisation of Ar^+ ion etched and $SiCl_4$ reactive ion etched silicon (100)," *Mater. Sci. Tech.*, vol. 13, no. 11, pp. 961–964, Nov. 1997.

[2] K. Eriguchi, A. Ohno, D. Hamada, M. Kamei, and K. Ono, "Estimation of defect generation probability in thin Si surface damaged layer during plasma processing," *Thin Solid Films*, vol. 516, no. 19, pp. 6604–6608, Aug. 2008.

[3] A. Matsuda, Y. Nakakubo, Y. Takao, K. Eriguchi, and K. Ono, "Optical Characterization of Plasma-Induced Si Damage by Ar and Cl_2 Inductively Coupled Plasmas," presented at the Plasma Etch and Strip in Microelectronics, Grenoble, France, 2012.

[4] H. Chouaib, M. E. Murtagh, V. Guènebaut, S. Ward, P. V. Kelly, M. Kennard, Y. M. Le Vaillant, M. G. Somekh, M. C. Pitter, and S. D. Sharples, "Rapid photoreflectance spectroscopy for strained silicon metrology," *Rev. Sci. Instrum.*, vol. 79, no. 10, 103106, Oct. 2008.

[5] K. Eriguchi, A. Ohno, D. Hamada, M. Kamei, H. Fukumoto, and K. Ono, "Quantitative characterization of plasma-induced defect generation process in exposed thin Si surface layers," *Jpn. J. Appl. Phys.*, vol. 47, no. 4, pp. 2446–2451, Apr. 2008.

[6] M. Losurdo, M. Bergmair, G. Bruno, D. Cattelan, C. Cobet, A. de Martino, K. Fleischer, Z. Dohcevic-Mitrovic, N. Esser, M. Galliet, R. Gajic, D. Hemzal, K.

Hingerl, J. Humlicek, R. Ossikovski, Z. V. Popovic, and O. Saxl, "Spectroscopic ellipsometry and polarimetry for materials and systems analysis at the nanometer scale: state-of-the-art, potential, and perspectives," *J. Nanopart. Res.*, vol. 11, no. 7, pp. 1521–1554, Oct. 2009.

[7] H. Chouaib, M. E. Murtagh, and P. V. Kelly, "A micro-optical modulation spectroscopy technique for local strain measurement," *Rev. Sci. Instrum.*, vol. 82, no. 4, 043901, Apr. 2011.

[8] I. Ferain, C. A. Colinge, and J.-P. Colinge, "Multigate transistors as the future of classical metal-oxide-semiconductor field-effect transistors," *Nature*, vol. 479, no. 7373, pp. 310–316, Nov. 2011.

[9] "International Technology Roadmap for Semiconductors: 2012 Update," 2012. [Online]. Available: http://www.itrs.net/.

[10] K. J. Kanarik, G. Kamarthy, and R. A. Gottscho, "Plasma etch challenges for FinFET transistors," *Solid State Tech.*, vol. 55, no. 3, Apr. 2012.

Appendix

A.1. Stillinger–Weber-type interatomic potential set

The molecular dynamics simulation in this work is based on the program developed by Ohta *et al.* [1]–[3] that uses a Stillinger–Weber-type interatomic potential set. In this potential set, the total energy of the atomic system is expressed by the summation of two- and three-body potentials as

$$\Phi = \sum_{i}^{N}\sum_{j>i}^{N} v_2(i,j) + \sum_{i}^{N}\sum_{j>i}^{N}\sum_{k>j}^{N} v_3(i,j,k) \tag{A.1}$$

where N is the number of atoms in the system. The indices i, j, and k denote the i-th, the j-th, and the k-th atom. The exact forms of $v_2(i,j)$ and $v_3(i,j,k)$ are explained below. Refer to articles by Watanabe [4] and Ohta and Hamaguchi [2] for the parameter values therein.

When the pair of atoms (i,j) is either (Si,Si), (Si,O), or (O,O), it is assumed that the two-body potential between them $v_2(i,j)$ has the form

$$v_2(i,j) \equiv v_{ij}(r_{ij}) = \begin{cases} g(i,j)A_{ij}\left(\dfrac{B_{ij}}{r_{ij}^{p_{ij}}} - \dfrac{1}{r_{ij}^{q_{ij}}}\right)\exp\left(\dfrac{C_{ij}}{r_{ij}-a_{ij}}\right) & (\text{if } r_{ij} < a_{ij}) \\ 0 & (\text{otherwise}) \end{cases} \tag{A.2}$$

where $r_{ij} = \left|\mathbf{r}_j - \mathbf{r}_i\right|$ denotes the distance between the two atoms located at $\mathbf{r}_i$ and $\mathbf{r}_j$. The cut-off distance is denoted by a_{ij}. The parameters

$A_{ij}, B_{ij}, C_{ij}, p_{ij}, q_{ij}$, and a_{ij} take different values depending on the species of i and j. $g(i,j)$ is the bond-softening function designed to reproduce the valence of oxygen [4]. The parameters have been fitted to *ab initio* quantum-mechanical calculations based on a density-functional method using *Gaussian* [8].

When either of the atoms is argon, $v_2(i,j)$ is modeled using the pseudo-Molière potential. The Molière potential [9] is one of the special cases of what is known as a *screened Coulomb potential* expressed by an analytical solution to the Thomas–Fermi equation [10], [11]. The Molière potential is expressed as

$$V(r_{ij}) = \frac{Z_i Z_j e^2}{4\pi\varepsilon_0 r_{ij}} \left[0.35\exp\left(-\frac{0.3r_{ij}}{a_F}\right) + 0.55\exp\left(-\frac{1.2r_{ij}}{a_F}\right) + 0.10\exp\left(-\frac{6.0r_{ij}}{a_F}\right) \right], \tag{A.3}$$

where a_F is the Firsov screening radius [12]

$$a_F = 0.8853 \cdot a_0 \left(Z_i^{1/2} + Z_j^{1/2} \right)^{-2/3}. \tag{A.4}$$

Z_i and Z_i are the number of protons contained in the nucleus, and a_0 is the Bohm radius

$$a_0 = \frac{4\pi\varepsilon_0 \hbar^2}{m_e e^2} = 5.292 \times 10^{-11} \text{ [m]}, \tag{A.5}$$

where m_e is the electron rest mass and e is the elementary charge. Detailed discussion and derivation of these equations can be found in the literature by Torrens [13]. In this simulation, the Molière potential has been fitted to Eq. (A.2) (the pseudo-Molière potential [2]).

The three-body term $v_3(i,j,k)$ for (*i*,*j*,*k*) combinations of Si and O is separated into three symmetrical terms,

$$\begin{aligned} v_3(i,j,k) &\equiv v_{ijk}(\mathbf{r}_i,\mathbf{r}_j,\mathbf{r}_k) \\ &= h_{jik}(r_{ij},r_{ik},\theta_{jik}) + h_{ijk}(r_{ji},r_{jk},\theta_{ijk}) + h_{ikj}(r_{ki},r_{kj},\theta_{ikj}) \end{aligned} \tag{A.6}$$

$$h_{jik}(r_{ij},r_{ik},\theta_{jik}) = \begin{cases} \lambda_{jik}\exp\left[\dfrac{\gamma^j_{jik}}{r_{ij}-a^j_{jik}} + \dfrac{\gamma^k_{jik}}{r_{ik}-a^k_{jik}}\right]\cdot\left|\cos\theta_{jik}-\cos\theta^0_{jik}\right|^{2\alpha_{jik}} \\ \qquad\qquad (\text{if } r_{ij} < a^j_{jik} \text{ and } r_{ik} < a^k_{jik}) \\ 0 \quad (\text{otherwise}) \end{cases} \tag{A.7}$$

where θ_{jik} is the angle spanned by two vectors $(\mathbf{r}_j - \mathbf{r}_i)$ and $(\mathbf{r}_k - \mathbf{r}_i)$. Here, parameters λ_{jik}, γ^j_{jik}, γ^k_{jik}, a^j_{jik}, a^k_{jik}, θ^0_{jik}, and α_{jik} are dependent on the species of *i*, *j*, and *k*. For example, $\cos\theta^0_{jik} = -1/3$ and $\alpha_{jik} = 1.0$ holds regardless of *j* and *k* when *i* = Si [2]. Thus, the cosine term is minimized when $\theta_{jik} = \arccos(-1/3) = 109.47°$, giving the sp^3 tetrahedral diamond-like structure of crystalline silicon [14].

When the (*i*,*j*,*k*) combination contains argon, $v_3(i,j,k) = 0$. This is because noble gases do not form covalent bonds, and its potential can be expressed by a superposition of screened two-body Coulomb potentials.

A.2. References

[1] H. Ohta and S. Hamaguchi, "Molecular dynamics simulation of silicon and silicon dioxide etching by energetic halogen beams," *J. Vac. Sci. Technol. A*, vol. 19, no. 5, pp. 2373–2381, Sep./Oct. 2001.

[2] H. Ohta and S. Hamaguchi, "Classical interatomic potentials for Si–O–F and Si–O–Cl systems," *J. Chem. Phys.*, vol. 115, no. 14, pp. 6679–6690, Oct. 2001.

[3] H. Ohta, A. Iwakawa, K. Eriguchi, and K. Ono, "An interatomic potential model for molecular dynamics simulation of silicon etching by Br^+-containing plasmas," *J. Appl. Phys.*, vol. 104, no. 7, 073302, Oct. 2008.

[4] T. Watanabe, H. Fujiwara, H. Noguchi, T. Hoshino, and I. Ohdomari, "Novel Interatomic Potential Energy Function for Si, O Mixed Systems," *Jpn. J. Appl. Phys.*, vol. 38, pp. L366–L369, Apr. 1999.

[5] F. Cerdeira and M. Cardona, "Photoreflectance and electroreflectance in silicon," *Solid State Commun.*, vol. 7, no. 12, pp. 879–882, Jun. 1969.

[6] M. Murtagh, S. M. Lynch, P. V. Kelly, S. Hildebrandt, P. A. F. Herbert, C. Jeynes, and G. M. Crean, "Photoreflectance characterisation of Ar^+ ion etched and $SiCl_4$ reactive ion etched silicon (100)," *Mater. Sci. Tech.*, vol. 13, no. 11, pp. 961–964, Nov. 1997.

[7] H. Moriya, A. Kaneta, and S. Adachi, "Photoreflectance study of crystalline silicon," *Mater. Sci. Eng. B*, vol. 76, no. 3, pp. 232–236, Jul. 2000.

[8] J. B. Foresman and A. Frisch, *Exploring Chemistry with Electronic Structure Methods*. Pittsburgh: Gaussian, 1996.

[9] G. Molière, "Therorie der Streuung schneller geladener Teilchen I. Einzelstreuung am abgeschirmten Coulomb-Feld," *Z. Naturforsch.*, vol. 2a, pp. 133–145, 1947.

[10] L. H. Thomas, "The Calculation of Atomic Fields," *Math. Proc. Cambridge Phil. Soc.*, vol. 23, no. 5, pp. 542–548, Jan. 1927.

[11] E. Fermi, "Un Metodo Statistico per la Determinazione di alcune Priorieta dell'Atome," *Rend. Accad. Naz. Lincei*, vol. 6, pp. 602–607, 1927.

[12] O. B. Firsov, "Calculation of the Interaction Potential of Atoms," *Sov. J. Exp. Theo. Phys.*, vol. 6, pp. 534–537, 1958.

[13] I. Torrens, *Interatomic Potentials*. New York: Academic Press, 1972.

[14] C. Kittel, *Introduction to Solid State Physics*, 8th ed. Hoboken, NJ: John Wiley & Sons, 2005.

Acknowledgments

First and foremost, I would like to appreciate Prof. Kouichi Ono for his kind guidance and insightful commentaries backed by his immense knowledge. Assoc. Prof. Koji Eriguchi has been my most enlightening mentor, and I cannot thank him enough for his thorough guidance and patience in every aspect of my time during this study. Assis. Prof. Yoshinori Takao has given me many helpful comments and warm encouragement. The MD simulation in this study relies heavily on prior art by Dr. Hiroaki Ohta (the former assistant professor).

I would like to thank Prof. Akitomo Tachibana and Prof. Kenji Kimura at the Department of Micro Engineering, Kyoto University for reviewing this dissertation and providing valuable advice and comments.

Drs. Tetsuya Tatsumi, Masanaga Fukasawa, Masaki Minami, Fumikatsu Uesawa, and Nobuyuki Kuboi at Sony Corporation has given me not only helpful advices regarding applications and demands from the industrial perspective, but also valuable guidance and encouragement during the course of this study.

I am again grateful to Drs. Masaki Yoshimaru, Sumio Kuwahara, Moritaka Nakamura, Shuichi Noda, Shigenori Hayashi, Hideo Nakagawa, Kenji Ishikawa, Tokuhisa Oiwa, Hikaru Kokura, and Hisataka Hayashi at Semiconductor Technology Academic Research Center (STARC) for their helpful advice and discussions.

I would like to thank all the members of the Propulsion Engineering Laboratory. In particular, my special thanks go to my senior teammates of *SHANa* team, Mr. Masayuki Kamei and Mr. Yoshinori Nakakubo, whose shoulders are which I stand upon. I greatly enjoyed being with my colleagues Mr. Takumi Saegusa and Mr. Hirotaka Tsuda, and would like to thank them for being such nice and friendly rivals.

This work was financially supported in part by Grants-in-Aid for Scientific Research from the Japan Society for the Promotion of Science (JSPS) and STARC. I have benefited from JSPS Research Fellowship for Young Scientists for two years within the duration of this study.

Finally, this work would not have been possible without the warmest support and continuous encouragement from my terrific family, Mitsuo Matsuda, Yumiko Matsuda, and Fuyuki Matsuda, to whom I wish to dedicate this dissertation.

List of Publications

Journal Articles

1. A. Matsuda, Y. Nakakubo, Y. Takao, K. Eriguchi, and K. Ono, "Advanced Contactless Analysis of Plasma-Induced Damage on Si by Temperature-Controlled Photoreflectance Spectroscopy," *Jpn. J. Appl. Phys.*, vol. 50, no. 8, 08KD03, Aug. 2011.
   DOI: 10.1143/JJAP.50.08KD03
2. K. Eriguchi, Y. Nakakubo, A. Matsuda, M. Kamei, Y. Takao, and K. Ono, "Trade-Off Relationship between Si Recess and Defect Density Formed by Plasma-Induced Damage in Planar Metal–Oxide–Semiconductor Field-Effect Transistors and the Optimization Methodology," *Jpn. J. Appl. Phys.*, vol. 50, no. 8, 08KD04, Aug. 2011.
   DOI: 10.1143/JJAP.50.08KD04
3. M. Fukasawa, Y. Nakakubo, A. Matsuda, Y. Takao, K. Eriguchi, K. Ono, M. Minami, F. Uesawa, and T. Tatsumi, "Structural and electrical characterization of HBr/O_2 plasma damage to Si substrate," *J. Vac. Sci. Technol. A,* vol. 29, issue 4, 041301, Jun. 2011.
   DOI: 10.1116/1.3596606
4. K. Eriguchi, Y. Nakakubo, A. Matsuda, M. Kamei, Y. Takao, and K. Ono, "Threshold Voltage Instability Induced by Plasma Process Damage in Advanced Metal–Oxide–Semiconductor Field-Effect Transistors," *Jpn. J. Appl. Phys.*, vol. 49, no. 8, 08JC02, Aug. 2010.
   DOI: 10.1143/JJAP.49.08JC02
5. Y. Nakakubo, A. Matsuda, M. Fukasawa, Y. Takao, T. Tatsumi, K. Eriguchi, and K. Ono, "Optical and Electrical Characterization of Hydrogen-Plasma- Damaged Silicon Surface Structures and Its Impact on In-line Monitoring," *Jpn. J. Appl. Phys.*, vol. 49, no. 8, 08JD02, Aug. 2010.
   DOI: 10.1143/JJAP.49.08JD02

6. K. Eriguchi, Y. Nakakubo, A. Matsuda, Y. Takao, and K. Ono, "Model for Bias Frequency Effects on Plasma-Damaged Layer Formation in Si Substrates," *Jpn. J. Appl. Phys.*, vol. 49, no. 5, 056203, May 2010. * 第 33 回応用物理学会優秀論文賞
DOI: 10.1143/JJAP.49.056203
7. A. Matsuda, Y. Nakakubo, Y. Takao, K. Eriguchi and K. Ono, "Modeling of Ion-Bombardment Damage on Si Surfaces for In-Line Analysis," *Thin Solid Films*, vol. 518, issue 13, pp. 3481–3486, Apr. 2010.
DOI: 10.1016/j.tsf.2009.11.044
8. K. Eriguchi, Y. Nakakubo, A. Matsuda, Y. Takao, and K. Ono, "Plasma-Induced Defect-Site Generation in Si Substrate and Its Impact on Performance Degradation in Scaled MOSFETs," *IEEE Electron Device Lett.*, vol. 30, issue 12, pp. 1275-1277, Dec. 2009.
DOI: 10.1109/LED.2009.2033726
9. K. Eriguchi, A. Matsuda, Y. Nakakubo, M. Kamei, H. Ohta and K. Ono, "Effects of Plasma-Induced Si Recess Structure on n-MOSFET Performance Degradation," *IEEE Electron Device Lett.*, vol. 30, issue 7, pp. 712–714, Jul. 2009.
DOI: 10.1109/LED.2009.2022347

Book

1. Y. Nakakubo, A. Matsuda, M. Kamei, H. Ohta, K. Eriguchi, and K. Ono, "Analysis of Si Substrate Damage Induced by Inductively Coupled Plasma Reactor with Various Superposed Bias Frequencies," in *Emerging Technologies and Circuits* (Lecture Notes in Electrical Engineering 66), A. Amara, M. Belleville, and T. Ea, Eds., London, UK: Springer, 2010, part IV, ch. 8, pp. 107–120.
ISBN 978-90-481-9378-3

Invited talks

1. K. Eriguchi, Y. Nakakubo, A. Matsuda, Y. Takao, and K. Ono, "Modeling as a powerful tool for understanding surface damage during plasma processing of materials," presented at Plasma Etch and Strip in Microelectronics (PESM), Leuven, Belgium, Mar. 14–15, 2013.
2. A. Matsuda, Y. Nakakubo, Y. Takao, K. Eriguchi, and K. Ono, "プラズマからのイオン照射ダメージと光学的評価手法 (Ion-Bombardment Damage from Plasma and Its Optical Characterization Techniques)," presented at the Japan Society of Applied Physics Silicon Technology Division, Tokyo, Japan, Feb. 15, 2013. Published as *応用物理学会分科会 シリコンテクノロジー*, no. 156, pp. 11–18, Feb. 2013. ISBN 978-4-86348-318-7
3. A. Matsuda, Y. Nakakubo, Y. Takao, K. Eriguchi, and K. Ono, "プラズマプロセスにおける Si 基板ダメージと光学的評価手法 (Si Substrate Damage during Plasma Processes and Optical Characterization Techniques)," presented at the 5th ICAN Kyou Sou Seminar: ナノデバイスにおける微細加工技術についてのオープンセミナー, Tsukuba, Japan, Mar. 5, 2012.
4. K. Eriguchi, Y. Nakakubo, A. Matsuda, Y. Takao, and K. Ono, "物理的プラズマダメージによる MOSFET バラツキ増大予測のための包括モデル (Design Framework for Parameter Fluctuation in MOSFET Damaged by Ion Bombardment during Plasma Etching)," presented at シリコン材料・デバイス (SDM) 研究会, Sendai, Japan, Oct. 20–21, 2011. Published as *信学技法*, vol. 111, no. 249, pp. 73–78, Oct. 2011.

International conference contributions

1. A. Matsuda, Y. Nakakubo, M. Fukasawa, Y. Takao, T. Tatsumi, K. Eriguchi, and K. Ono, "Three-Dimensional Parameter Mapping of Annealing Processes for HBr/O_2-Plasma-Induced Damages in Si Substrates," in *Proc. 34th Int. Symp. Dry Process* (DPS 2012), Tokyo, Japan, Nov. 15–16, 2012, pp. 181–182.
2. Y. Nakakubo, A. Matsuda, M. Fukasawa, Y. Takao, T. Tatsumi, K. Eriguchi, and K. Ono, "Detailed Analysis of Si Substrate Damage Induced by HBr/O_2- and

H_2-Plasma Etching and the Recovery Process Designs," presented at the AVS 59th International Symposium & Exhibition, Tampla, FL, USA, Oct. 28–Nov. 2, 2012.

3. K. Eriguchi, Y. Nakakubo, A. Matsuda, M. Kamei, Y. Takao, and K. Ono, "Optimization Problems for Plasma-Induced Damage: A Concept for Plasma-Induced Damage Design," in *2012 IEEE Int. Conf. IC Design & Technol.* (ICICDT), Austin, TX, USA, May 30–June 1, 2012.
   DOI: 10.1109/ICICDT.2012.6232840
4. A. Matsuda, Y. Nakakubo, Y. Takao, K. Eriguchi, and K. Ono, "Optical Characterization of Plasma-Induced Si Damage by Ar and Cl_2 Inductively Coupled Plasmas," presented at the Plasma Etch and Strip in Microelectronics (PESM), Grenoble, France, March 15–16, 2012.
5. K. Eriguchi, Y. Nakakubo, A. Matsuda, Y. Takao, and K. Ono, "Unifed Model-Prediction Framework for MOSFET Performance Degradation by Plasma-Induced Si Damage and its Application to Process Parameter Optimization," presented at the Plasma Etch and Strip in Microelectronics (PESM), Grenoble, France, March 15–16, 2012.
6. A. Matsuda, Y. Nakakubo, Y. Takao, K. Eriguchi, and K. Ono, "Defect Profiling Using a Wet-Etch Technique and Photoreflectance Spectroscopy for He- and Ar-Plasma-Damaged Si Substrate," in *Proc. 33rd Int. Symp. Dry Process* (DPS 2011), Kyoto, Japan, Nov. 10–11, 2011, pp. 159–160.
7. A. Matsuda, Y. Nakakubo, Y. Takao, K. Eriguchi, and K. Ono, "Improvement in the Evaluation Technique for Plasma-Etch Si Damage using Photoreflectance Spectroscopy with Temperature Control," presented at the AVS 58th International Symposium & Exhibition, Nashville, TN, USA, Oct. 30–Nov. 4, 2011.
8. Y. Nakakubo, A. Matsuda, M. Fukasawa, Y. Takao, T. Tatsumi, K. Eriguchi, and K. Ono, "Effect of Rapid Thermal Annealing on Si Surface Damage by HBr/O_2- and H_2-Plasma," presented at the AVS 58th International Symposium & Exhibition, Nashville, TN, USA, Oct. 30–Nov. 4, 2011.
9. A. Matsuda, Y. Nakakubo, Y. Takao, K. Eriguchi, and K. Ono, "Advanced Contactless Analysis of Plasma-Induced Damage on Si by Temperature-Controlled Photoreflectance Spectroscopy," in *Proc. 32nd Int. Symp. Dry Process* (DPS 2010), Tokyo, Japan, Nov. 11–12, 2010, pp. 191–192.

* DPS 2010 Young Researcher Award

10. K. Eriguchi, Y. Nakakubo, A. Matsuda, Y. Takao, and K. Ono, "Trade-Off Relationship between Si Recess and Defect Density Formed by Plasma-Induced Damage in Planar MOSFETs and the Optimization Strategies," in *Proc. 32nd Int. Symp. Dry Process* (DPS 2010), Tokyo, Japan, Nov. 11–12, 2010, pp. 185–186.
11. Y. Nakakubo, A. Matsuda, Y. Takao, K. Eriguchi, and K. Ono, "Study of Wet-Etch Rate of Plasma-Damaged Surface and Interface Layers and Residual Defect Sites," in *Proc. 32nd Int. Symp. Dry Process* (DPS 2010), Tokyo, Japan, Nov. 11–12, 2010, pp. 173-174.
12. A. Matsuda, Y. Nakakubo, M. Kamei, Y. Takao, K. Eriguchi, and K. Ono, "Assessment of Ion-Bombardment Damage in Plasma-Exposed Si by Interface Layer Thickness and Charge-Trapping Defects," in *Ext. Abstr. 2009 Int. Conf. Solid State Devices & Mater.* (SSDM), Sendai, Japan, Oct. 7–9, 2009, pp. 346-347.
13. A. Matsuda, Y. Nakakubo, R. Ogino, H. Ohta, K. Eriguchi, and K. Ono, "Simulation and Experimental Study on the Characteristics of Plasma-Induced Damage and Methodology for Accurate Damage Analysis," in *2009 IEEE Int. Conf. IC Design & Technol.* (ICICDT), Austin, TX, USA, May 18–20, 2009, pp. 97–100. DOI: 10.1109/ICICDT.2009.5166274
14. K. Eriguchi, A. Matsuda, Y. Nakakubo, M. Kamei, H. Ohta, and K. Ono, "Study of Plasma-Induced 'Si Recess Structure' and Its Effects on Threshold Voltage Variability in Advanced MOSFETs," in *2009 IEEE Int. Conf. IC Design & Technol.* (ICICDT), Austin, TX, USA, May 18–20, 2009, pp. 101–104. DOI: 10.1109/ICICDT.2009.5166275
15. A. Matsuda, Y. Nakakubo, Y. Ueda, H. Ohta, K. Eriguchi, and K. Ono, "Significance of Interface Layer between Surface Layer and Si Substrate in Plasma-Exposed Structures and Its Impacts on Plasma-Induced Damage Analysis," in *Ext. Abstr. 2008 Int. Conf. Solid State Devices & Mater.* (SSDM), Tsukuba, Japan, Sep. 23–26, 2008, pp. 358–359.
16. K. Eriguchi, Y. Nakakubo, A. Matsuda, Masayuki Kamei, Y. Takao, and K. Ono, "Comprehensive Modeling of Threshold Voltage Variability Induced by Plasma Damage in Advanced MOSFETs," in *Ext. Abstr. 2008 Int. Conf. Solid State Devices & Mater.* (SSDM), Tsukuba, Japan, Sep. 23–26, 2008, pp. 338-339.
17. Y. Nakakubo, A. Matsuda, M. Fukasawa, Y. Takao, T. Tatsumi, K. Eriguchi, and K. Ono, "Optical and Electrical Characterization of H_2 Plasma-Damaged Si Surface

Structures and its Impact on In-line Monitoring," in *Proc. 31st Int. Symp. Dry Process* (DPS 2009), Busan, Korea, Sep. 24–25, 2009, pp. 125–126.

18. K. Eriguchi, Y. Nakakubo, A. Matsuda, M. Kamei, Y. Takao, and K. Ono, "Threshold Voltage Instability Induced by Plasma Process Damage in Advanced MOSFETs," in *Proc. 31st Int. Symp. Dry Process* (DPS 2009), Busan, Korea, Sep. 24–25, 2009, pp. 267-268. * DPS 2009 Best Paper Award
19. K. Eriguchi, Y. Nakakubo, A. Matsuda, M. Kamei, H. Ohta, H. Nakagawa, S. Hayashi, S. Noda, K. Ishikawa, M. Yoshimaru, and K. Ono, "A New Framework for Performance Prediction of Advanced MOSFETs with Plasma-Induced Recess Structure and Latent Defect Site," in *IEEE Int. Electron Devices Meet. 2008* (IEDM), Dec. 15–17, 2008, San Francisco, CA, USA.
DOI: 10.1109/IEDM.2008.4796720
20. Y. Nakakubo, A. Matsuda, Y. Ueda, H. Ohta, K. Eriguchi, and K. Ono, "Clarification of Surface and Interface Structures exposed to Inductively Coupled Plasma with Various Superposed Bias Frequencies and Its Implication in Plasma Damage Control," presented at AVS 55th International Symposium & Exhibition, Boston, MA, USA, Oct. 19–24, 2008.
21. Y. Nakakubo, A. Matsuda, M. Kamei, H. Ohta, K. Eriguchi and K. Ono, "Analysis of Si Substrate Damage Induced by Inductively Coupled Plasma Reactor with Various Superposed Bias Frequencies," in *2008 Int. Conf. IC Design & Technol.* (ICICDT), Grenoble, France, June 2–4, 2008, pp. 101-104.

Japanese conference contributions

1. A. Matsuda, Y. Nakakubo, Y. Takao, K. Eriguchi, and K. Ono, "温度制御型フォトリフレクタンス分光法を用いたプラズマ誘起 Si 基板ダメージの定量化とそのプロファイル解析 (Quantification and Profile Analysis of Plasma-Induced Si Substrate Damage using Temperature-Controlled Photoreflectance Spectroscopy)", presented at シリコン材料・デバイス (SDM) 研究会, Sendai, Japan, Oct. 25, 2012.
2. Y. Nakakubo, K. Eriguchi, A. Matsuda, Y. Takao, and K. Ono, "電気的手法を用いた物理的 Si 基板ダメージのプラズマプロセス依存性の検討 (Electrical

Characterization Techniques for Si Substrate Damage during Plasma Etching)", presented at シリコン材料・デバイス (SDM) 研究会, Sendai, Japan, Oct. 20–21, 2011. Published as *信学技法*, vol. 111, no. 249, pp. 79–84, Oct. 2011.

3. K. Eriguchi, Y. Nakakubo, A. Matsuda, Y. Takao, and K. Ono, "Model for Bias Frequency Effects on Plasma-Damaged Layer Formation in Si Substrates," presented at 第 72 回 応用物理学会学術講演会 (72nd JSAP Autumn Meeting), Yamagata, Japan, Aug. 29–Sep. 2, 2011.
4. Y. Nakakubo, A. Matsuda, M. Fukasawa, Y. Takao, T. Tatsumi, K. Eriguchi, and K. Ono, "HBr/O_2, H_2プラズマダメージに対する高速熱処理プロセスの効果," presented at 第 72 回 応用物理学会学術講演会 (72nd JSAP Autumn Meeting), Yamagata, Japan, Aug. 29–Sep. 2, 2011.
5. K. Eriguchi, Y. Nakakubo, A. Matsuda, Y. Takao, and K. Ono, "プラズマプロセスにおける Si 基板ダメージ層形成モデルの提案," presented at 第 71 回 応用物理学会学術講演会 (71st JSAP Autumn Meeting), Nagasaki, Japan, Sep. 14–17, 2010.
6. A. Matsuda, Y. Nakakubo, Y. Takao, K. Eriguchi, and K. Ono, "分子動力学法によるプラズマ誘起ダメージ予測:イオンエネルギー分布の影響 (Projecting Plasma-Induced Damage by Molecular Dynamics Simulation: Effects of Ion Energy Distribution)," presented at 第 71 回 応用物理学会学術講演会 (71st JSAP Autumn Meeting), Nagasaki, Japan, Sep. 14–17, 2010.
7. M. Fukasawa, Y. Nakakubo, A. Matsuda, Y. Takao, K. Eriguchi, K. Ono, M. Minami, F. Uesawa, T. Tatsumi: "H を含むプラズマによる Si 基板ダメージの構造解析 (II)," presented at 第 71 回 応用物理学会学術講演会 (71st JSAP Autumn Meeting), Nagasaki, Japan, Sep. 14–17, 2010.
8. A. Matsuda, Y. Nakakubo, M. Fukasawa, Y. Takao, T. Tatsumi, K. Eriguchi, and K. Ono, "H_2を含むプラズマによる Si 基板ダメージの光学的・電気的構造 (Optical and Electrical Structure of Si Substrates Damaged by H_2-Containing Plasma)," presented at 第 70 回応用物理学会学術講演会 (70th JSAP Autumn Meeting), Toyama, Japan, Sep. 8–11, 2009.
9. Y. Nakakubo, A. Matsuda, Y. Takao, K. Eriguchi, and K. Ono, "Effects of O_2 addition on Si substrate surface damage exposed to Ar plasma," presented at the 22nd Symposium on Plasma Science for Materials (SPSM), Tokyo, Japan, June 15–16, 2009.
10. A. Matsuda, Y. Nakakubo, Y. Takao, K. Eriguchi, and K. Ono, "Modeling of

Ion-Bombardment Damage on Si Surfaces for In-Line Analysis," presented at the 22nd Symposium on Plasma Science for Materials (SPSM), Tokyo, Japan, June 15–16, 2009.

11. Y. Nakakubo, A. Matsuda, R. Ogino, Y. Ueda, K. Eriguchi, and K. Ono, "O_2 添加 Ar プラズマによる Si 基板表面層内誘起欠陥の電気的解析," presented at 第 56 回応用物理学関係連合講演会 (56th JSAP Spring Meeting), Tsukuba, Japan, Mar. 30–Apr. 2, 2009.
12. A. Matsuda, R. Ogino, Y. Nakakubo, H. Ohta, K. Eriguchi, and K. Ono, "Si 表面のプラズマダメージの精確な解析における界面層の重要性 (On the Importance of Interface Layer in Accurate Analysis of Plasma-Induced Damage on Si Surfaces)," presented at 第 56 回応用物理学関係連合講演会 (56th JSAP Spring Meeting), Tsukuba, Japan, Mar. 30–Apr. 2, 2009.
13. A. Matsuda, R. Ogino, Y. Nakakubo, H. Ohta, K. Eriguchi, and K. Ono, "Si 表面におけるプラズマダメージ層増大の分光エリプソメトリーと 分子動力学シミュレーションによる解析 (Detailed Analysis of Plasma-Damaged Layer and Its Significance in Si Surface Structures by Spectroscopic Ellipsometry and Molecular Dynamics Simulations)," in *Proc. Plasma Sci. Symp. 2009/26th Symp. Plasma Processing* (PSS-2009/SPP-26), Nagoya, Japan, Feb. 2–4, 2009, p. 424.
14. Y. Nakakubo, A. Matsuda, Y. Ueda, H. Ohta, K. Eriguchi, and K. Ono, "Ar 系プラズマにおける Si 表面層内誘起欠陥形成過程の O_2 添加効果," presented at 第 69 回応用物理学会学術講演会 (69th JSAP Autumn Meeting), Kasugai, Japan, Sep. 2–5, 2008.